Convection forced by horizontal differences in heating with two plumes or a sill

Melissa A. Coman

A thesis submitted for the degree of
Doctor of Philosophy
of The Australian National University.

Research School of Earth Sciences

December 2008

Except where otherwise indicated in the text, the research described in this thesis is my own original work.

Melissa A. Coman
December 1, 2008

Acknowledgements

Many people have travelled with me on this PhD journey, and I would like to thank them all.

Firstly, my supervisor Ross, who gave me the opportunity to study here. And equally importantly my advisor/supervisor, Graham, who, due to his close proximity to my office, often faced the brunt of my questions. I have learnt much while I've been studying here with you both and I thank you for your patience and encouragement.

Laboratory experiments feature prominently in this work and none of them would have been possible without the help of Tony Beasley who built, maintained (and fixed) all my tanks. The GFD Matlab and LaTeX help desk was well serviced by Andy Hogg. Brad Ferguson whose invaluable advice made capturing the perfect pictures of my flows easy. The GFD group has offered a lot of great lunchtime discussion and advice, so thanks to Andy, Ross K, Geoff, Stewart, Mel, Kial and Jesse.

I've also had some great opportunities to get 'real' oceanographic experience through a voyage on the Southern Surveyor and two cruises on the Aurora Australis. So thanks to the CSIRO, but particularly, Steve Rintoul and Bronte Tilbrook.

I've had the pleasure to meet and become good friends with two long-term office mates during my PhD. Firstly, Leela who shared with me during her honours year, and now Andreea, who has been lucky enough to share with me for the past three years. Thank you Andreea for putting up with me and for continually making me question my own opinions. I've really enjoyed all the cups of tea and morning chats about mantle dynamics, Romania, my crazy dance group, Romania, LaTeX, Romania..... I'll leave our tea collection with you (but remember, if Ross runs out again, he will come looking for more in our office).

The Bordonian community has helped to keep me sane and entertained outside of work so a big thank you all, but especially to John and Aylwen, Jenny B, Gen, Linda, Will, Jason, Madelaine, Ceri, Christy and Eddie (I'm coming to pick up my Rutherglen wine tonight, and for the last time I am not including sea monkeys in this thesis!). Similarly, my housemate Dave has done a stellar job providing many happy hours watching Stargate and Dr. Who.

Thanks to my siblings, Lara, Elizabeth, William and Milly, and my extended family for keeping me amused and on my toes by continually asking me what I was researching. And to my parents for the long distance support you provided, and for helping me to get to university in the first place.

And lastly to Josh, for all the support and friendship you have given me over this most interesting year.

Abstract

Convective flows due to horizontal variations of heating are examined in this thesis. In the first experiment we investigate the influence by a partial barrier (modeling a sill in ocean bathymetry) on the circulation driven by heating one endwall of a rectangular cavity and cooling the other. The sill is a vertical partition that partially divides the cavity into two connected basins. We measure the heat and volume fluxes through the gap above the sill. It was found that for smaller gap sizes the magnitude of the volume transport decreases. The heat transport is unchanged for gap sizes that are greater than 20% of the cavity depth, and then decreases quickly for gap sizes that are less than 20%.

The second experiment explores the convective circulation that arises when a fluid is thermally forced by different arrangements of heating and cooling sources: the sources at the same level, the heating below the cooling and the cooling below the heating. All of these arrangements establish a horizontal temperature gradient and we observe a convective overturning in all cases. These findings are inconsistent with an early 20th century experiment carried out by Sandström (1908), in which it was concluded that a source of heating must be below a source of cooling for a convective circulation to exist. We conclude that Sandström's observations were in error and that his 'theorem' should not be used to discount the forcing of a deep convective overturning in the oceans by the meridional gradient of surface temperature or buoyancy fluxes.

The third experiment studies a class of horizontal convection in which the thermal forcing is such that there is one region of stabilising buoyancy flux but two regions of destabilising buoyancy flux. We focus on the steady state circulation owing to the two plumes that form as a consequence of the destabilising fluxes. We classify the flow into three regimes of overturning, according to the pattern of interior circulation and depending on the relative strengths of the two plumes. We found that unequal plumes increase the interior stratification above that of two equal plumes, and when one plume is stronger than the other by more than 10%, the interior stratification is set by the stronger plume. The numerical solutions for this experiment show a substantial variability in the form of internal gravity waves. The arrangement of buoyancy fluxes in this experiment mimics the high latitude sinking in the Northern and Southern Hemispheres of the current ocean. This experiment broadly outlines the interaction of two deep sinking plumes and describes how the circulation and interior stratification changes when the ratio of the destabilising 'surface' buoyancy fluxes change.

The final experiment introduces a sill to the horizontal convection experiment with two regions of destabilising flux. The gap above the sill must accommodate

a mass exchange in the thermal boundary layer and the return flow over the sill. When the gap height is 25% of the depth of the domain it is somewhat larger than the no sill boundary layer thickness. However, when the gap height is reduced to just 10% of the depth of the domain the sill extends into the region where the thermal boundary layer would otherwise be, so that in comparison to the no sill case, a significant deviation to the circulation pattern and heat transport occurs. Therefore, we again find that for a sill to have a significant effect on the circulation and heat transport the gap above the sill must be less than 25% of the depth of the domain.

The discovery of internal waves in the horizontal convection experiments raises the question as to whether much wave action is produced by the convection circulation, and in particular, by the plumes and plume outflows. We show that their presence in the laboratory convective flow accounted for some of the variability in the flow. The possibility of generation of internal waves by deep convection, sill overflows, slope currents and deep plume outflows may therefore be a new exciting area that needs further work.

Contents

List of Figures

List of Tables

Chapter 1

Introduction

1.1 Convection driven by horizontal density differences

Buoyancy-driven flows are commonplace in geophysical, environmental and engineering contexts. An important subset of these flows are those driven by horizontal gradients of buoyancy forcing. Many different types of buoyancy forcing will maintain a horizontal density difference in a body of fluid, leading to a convective circulation (Tritton, 1988). These forcing arrangements are fundamental to fluid dynamics and have many practical applications. The solar irradiation at the ocean surface results in a net heating at equatorial latitudes and a net cooling at polar latitudes, creating a meridional temperature gradient in the surface waters of the ocean. Vertically well-mixed estuaries often have a horizontal density gradient due to salinity which drives slow horizontal circulations in addition to tidal motions (Fischer, 1972; Imberger, 1974). Horizontal temperature differences in single rooms or entire buildings can be used to ventilate those enclosures by harnessing the convection that will naturally arise (Linden, 1999). Building ventilation involves modeling convection due to horizontal density differences in square or long enclosures. In contrast, double glazing, generally used for insulation purposes in windows and walls of buildings, is modeled by applying a temperature difference between closely spaced vertical walls (Eckert & Carlson, 1961). Industrial processes will commonly be subject to horizontal variations in buoyancy forcing (see for example Chiu-Webster *et al.*, 2008). In this thesis we focus on two canonical arrangements of buoyancy forcing: differential heating along one horizontal boundary, and a temperature difference between opposite vertical walls of a cavity.

'Horizontal convection' is the term used for flow arising from buoyancy forcing

applied at only one horizontal boundary. For instance, when the lower boundary of a long cavity is differentially heated a horizontal temperature gradient is established in a bottom boundary layer. The flow in the bottom boundary layer is towards the relatively hot end where it rises up the endwall in a plume until it reaches a neutral buoyancy level or the upper boundary (Rossby, 1965; Stommel, 1962). The plume outflow enters the interior of the cavity and then, rather more slowly, the interior fluid is advected downwards into the bottom boundary layer. The circulation is highly asymmetric with narrow upwelling and broad downwelling (Stommel, 1962). The asymmetry is due to the relative inefficiency of conduction compared to convection (Rossby, 1965). The density gradients are highest in the lower boundary layer and much smaller in the interior of the overturning cell. In the steady state the largest temperature in the cavity is located at the base of the plume. The Rayleigh number and Prandtl number will determine whether the convection is laminar or turbulent.

In contrast to horizontal convection, convection due to thermal forcing of opposite vertical walls has been well studied (Bejan, 1979, 1980; Bejan *et al.*, 1981; Bejan & Tien, 1978; Blythe & Simpkins, 1977; Cormack *et al.*, 1974*a*,*b*; Gill, 1966; Imberger, 1974; Patterson & Imberger, 1980; Simpkins & Chen, 1986; Simpkins & Dudderar, 1981). The circulation for this configuration varies with the aspect ratio of the cavity. For square or long cavities a single overturning cell fills the entire cavity. Fluid rises in the thermal boundary layer next to the heated endwall and sinks in the thermal boundary layer next to the cooled endwall. The interior is stably stratified. The strength of the forcing determines whether the heat is transported through the interior or primarily in the boundary layers. For weak forcing the majority of the heat transfer is through the interior. For stronger forcing the boundary layers accommodate most of the heat transfer. If the strength of the forcing is further increased the convection will become turbulent. For weak thermal forcing, the circulation in tall cavities consists of a single laminar overturning cell. When the forcing is slightly increased the circulation changes to exhibit a stacked cellular structure. If the forcing is further increased, the cellular structure breaks down into a single overturning cell which is driven by the boundary layer and has a turbulent core.

The two canonical cases previously described are both examples of convection driven by horizontal density differences, however some important differences should be highlighted. Forcing from vertical walls directly affects the entire water column, whereas horizontal convection is forced at one level only. This difference leads to a circulation that is symmetric when the fluid is forced by a thermal difference between

vertical walls, and a circulation that is highly asymmetric when the fluid is forced along one horizontal boundary (Rossby, 1965; Stommel, 1962).

In section 1.3 we will introduce studies of horizontal convection aimed at helping us understand the governing dynamics of the meridional overturning circulation. However, first in section 1.2, we describe the meridional overturning circulation of the ocean as it provides much of the motivation for the work in this thesis.

1.2 The meridional overturning circulation of the oceans

A simple "conveyor belt" schematic of the main oceanic currents and pathways is shown in figure 1.1 and gives an indication of the differences between ocean basins, though of course, the ocean currents are more complicated than the diagram might suggest. In contrast to the conveyor belt representation of the ocean the meridional overturning circulation (MOC) is a zonally integrated, time averaged view of the vertical circulation along a meridian in the ocean. It transports heat and mass meridionally in the ocean and has generated a lot of debate concerning the factors driving or governing the flow. A section that can be used to illustrate the nature of the MOC is shown in figure 1.2. The difference between the MOC and this section is that the MOC is zonally averaged whereas the section is a single meridional slice through the ocean.

At the surface of the ocean is a region directly modified and mixed by the wind and convection. This surface mixed layer is $50 - 100\,\mathrm{m}$ deep, depending on season and latitude, and it is characterised by vertically uniform temperature and salinity profiles. The thermocline is the region of large temperature gradients below the surface mixed layer. It is typically a few hundred metres thick and extends through the equatorial and mid-latitude regions. At latitudes above about 20° the surface waters experience a net loss of heat to the atmosphere (Houghton *et al.*, 1996), and therefore a meridional temperature gradient exists at the surface of the ocean. At the higher latitudes the density of the surface water is increased by cooling and, around the margins of Antarctica, by mixing with brine, produced from sea-ice formation. Providing there is not too much freshwater supply at the high latitudes (from precipitation and continental runoff), the surface water will be sufficiently dense to sink in localized plumes to the deep ocean. The sinking water is replaced by surface flow.

In the present regime the densest waters in the Southern Hemisphere are found

in the Weddell Sea, the Ross Sea and the Adelie Land, and the outflows from these regions sink to form Antarctic Bottom Water (AABW). In the Northern Hemisphere the densest waters are formed in the Labrador Sea in the North Atlantic and in the Norwegian Sea and Greenland Sea in the Arctic ocean. The outflows from these regions sink to form North Atlantic Deep Water (NADW) at $\sim 3000\,\mathrm{m}$ depth (Talley, 1999). If the deep flow was purely buoyancy-driven, the equation of state was linear and the plume geometries similar, this would immediately imply that the Southern Hemisphere sinking carries a larger buoyancy flux than the North Atlantic sinking (Hughes *et al.*, 2007; Killworth & Turner, 1982; Wong & Griffiths, 1999). A comparison of the density at the surface of the sinking regions from the Northern and Southern Hemispheres shows that the northern waters are more dense. However, the nonlinearities in the equation of state, and possibly the differences in plume geometry, results in the southern water being denser than the northern waters, at ocean bottom pressures. When these two water sources meet the NADW intrudes above the AABW.

Oceanographic measurements show that a stable density stratification exists in the abyssal ocean (depths $> 1000\,\mathrm{m}$), although it is much weaker than the vertical density gradients in the thermocline (Ledwell *et al.*, 1993). To maintain this abyssal stratification the dense, upwelling bottom water is warmed (and the density reduced) by the downward diffusion of heat from the thermocline (Munk, 1966). The rate of the downward diffusion of heat is measured to be greater than the molecular rate of thermal diffusion, which is about $10^{-7}\,\mathrm{m^2/s}$. Values of the thermal diffusion in the ocean are thought to vary depending on location, but are generally in the range $10^{-5}\,\mathrm{m^2/s}$ to $10^{-4}\,\mathrm{m^2/s}$, or higher in localized regions near bottom topography (see St Laurent & Simmons (2006) for a short summary of measurements). Therefore,

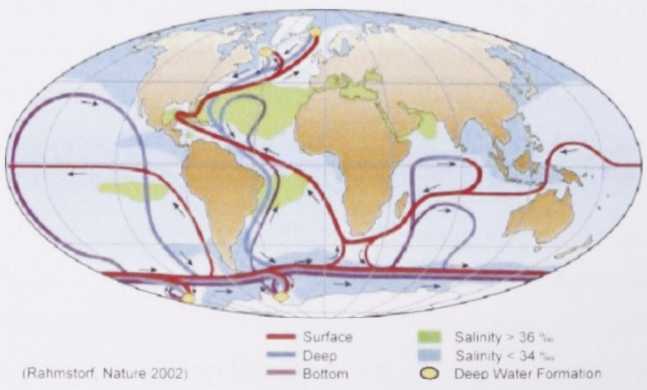

Figure 1.1: The "conveyor belt" circulation, from Rahmstorf (2002).

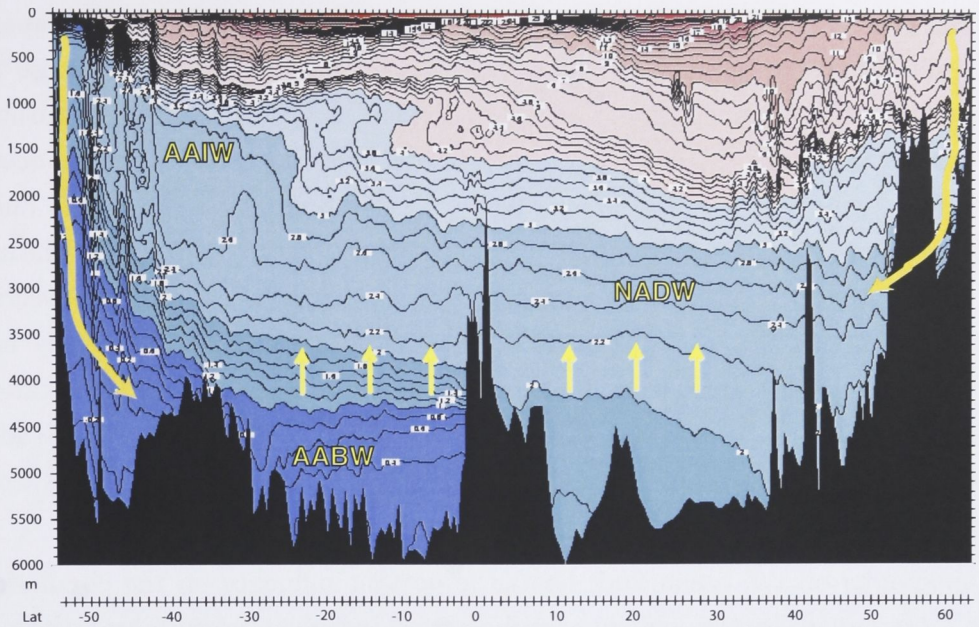

Figure 1.2: A meridional slice of potential temperature at 25° W from 50° S to 60° N. The warmest waters are in red and the coldest in blue. The densest waters are visible as originating from near Antarctica. The arrows show a schematic of the zonally integrated meridional flow. The locations of Antarctic Bottom Water (AABW), Antarctic Intermediate Water (AAIW) and North Atlantic Deep Water (NADW) are labelled.

heat that is diffused downwards involves turbulent mixing (Munk & Wunsch, 1998). The source of energy for this turbulence is most likely winds and tides, but the amount of turbulent mixing that occurs is a point of contention. In addition to turbulent mixing, heat can also be advected downward through entrainment into sinking plumes (Hughes & Griffiths, 2006). The production rate of dense water in marginal seas is only a fraction of the volume transport of deep water into the abyss near the bottom of the ocean. The entrainment of abyssal water into the dense slope currents increases the volume of NADW and AABW production by a factor of 2-3 (Price & Baringer, 1994). At depths above the bottom waters some upwelling may also take place along isopycnals (lines of constant density) due to surface wind forcing (Gnanadesikan *et al.*, 2007). Mixing can readily occur in the vicinity of fronts, and if these isopycnals outcrop at the surface, mixing will occur in the near-surface wind-mixed layer.

Open ocean deep convection is a mixing process that does not require coastal or sloping boundaries. As described by Killworth (1976) and Jones & Marshall (1993), it is possible if favourable conditions are present. A large scale background cyclonic circulation is needed which forms an upward doming of the isopyncals. In

addition, the underlying water must be preconditioned such that it is only weakly stratified. When strong surface forcing cools the surface layer it can expose the underlying weakly stratified layer, resulting in the whole column quickly overturning. The doming structures have scales up to 100 km, but the vertical mixing occurs in localised turbulent plumes whose diameter is of the order of 1 km. The radial spreading of well mixed water under gravity is controlled by rotation to form a new weakly stratified layer at intermediate depths. Open ocean deep convection is intermittent and not widespread. The cooling of the water column may help that water to sink into the abyssal ocean at a later time and in another location, specifically, at high-latitude deep sinking regions (Legg & Marshall, 1993; Send & Marshall, 1995). It has been shown that the majority of deep sinking occurs along sloping boundaries (Spall & Pickart, 2001).

Topography on the ocean floor has an important influence on the circulation. Large topographic features enhance local rates of turbulent mixing due to the interaction between the topography, the circulation, tides and internal waves. In addition, mid-ocean ridges produce buoyant hydrothermal fluid which can lead to heat input to the bottom of the ocean and megaplume formation (Woods & Bush, 1999). Topography like the Denmark Straits and Faroe Bank Channel (figure 1.3) has an additional effect. Dense water that has sunk in the Arctic Basin pools behind the ridges that extend between Greenland, Iceland and Scotland. This dense water overflows the sill as a turbulent slope current. The stratification and deep water properties in the main ocean basins are modified by hydraulic controls at the topographic sills and the density of the overflow, but in turn, the stratification of the main basin will modify the depth at which the slope currents intrude (Whitehead, 1998). Thus topography acts as a control on the circulation, causing the overall range of densities to be larger than it would be in the absence of topography (Bryden & Nurser, 2003). We will investigate this effect through simple models in the latter part of this thesis. Presently, the exchange of heat and mass fluxes through constrictions and over shallow sills between ocean basins, or between a marginal sea, such as the Mediterranean Sea, and the open ocean (Whitehead, 1998) are not well represented in general circulation or climate models and must be parameterised. The parameterisations are usually based on process models that describe the local flow.

Reconstructions of past climates have revealed how variable the climate system can be, and an important contributor to the state of the climate system is the ocean circulation, as it has a large capacity for storing and transporting heat. Three different patterns of circulation are thought to have existed during the last glacial

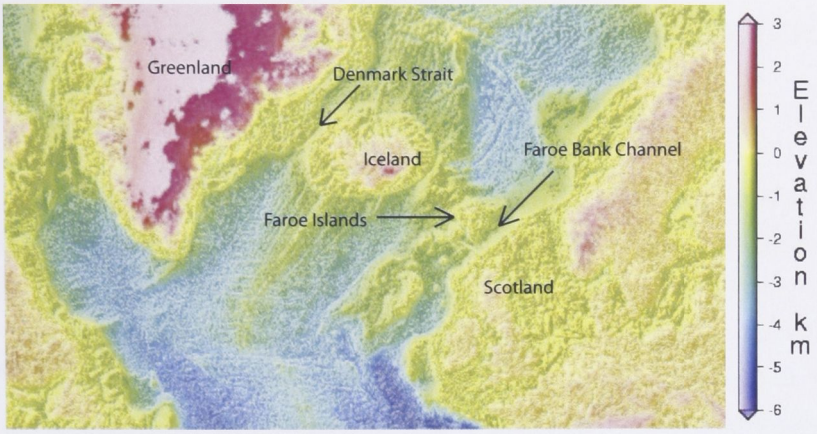

Figure 1.3: Bathymetry and topographic map of the Greenland-Iceland-Scotland ridge region, from Smith & Sandwell (1997), courtesy of Kial Stewart.

period with each tied to a particular climate, see figure 1.4 (Rahmstorf, 2002). The location of or even the existence of deep sinking regions does not have to be the same as it is today. The current interstadial or 'warm' mode has the North Atlantic water sinking further north (i.e. Norwegian Sea) than in the stadial or 'cold' mode, which has sinking south of Iceland. The third, or 'off' mode, is associated with Heinrich events, which are thought to be caused by large discharges of ice from melting icesheets in the Northern Hemisphere, resulting in a large input of surface fresh water and stopping the sinking in the North Atlantic altogether. The Antarctic Bottom Water would then dominate the northern abyssal ocean as well as the southern. Rahmstorf (2002) assumes the Southern Ocean is stable throughout the re-location of deep sinking regions in the Northern Hemisphere. However, the stability of the Southern Ocean's overturning branch has not been demonstrated.

We recall that in the Munk (1966) model, the maintenance of the stable stratification in the ocean requires a balance between the upward advection of abyssal waters and the downward diffusion of heat. The rate of molecular diffusion is not large enough to accommodate this balance so turbulent mixing is required. However, the source and amount of energy needed for the turbulent mixing is an unresolved issue. It is often argued that surface buoyancy forcing cannot provide energy to the oceans (through the potential energy field) and that therefore it does not have a role in driving the meridional overturning circulation (Huang, 1999; Munk, 1966; Munk & Wunsch, 1998; Paparella & Young, 2002; Wunsch, 2000, 2002; Wunsch & Ferrari, 2004). Neglecting buoyancy forcing as a means of energising the overturning leaves wind and tidal forcing as the only mechanism to fulfill the energy requirement.

Many models limit themselves to the vertical advection-diffusion balance as the

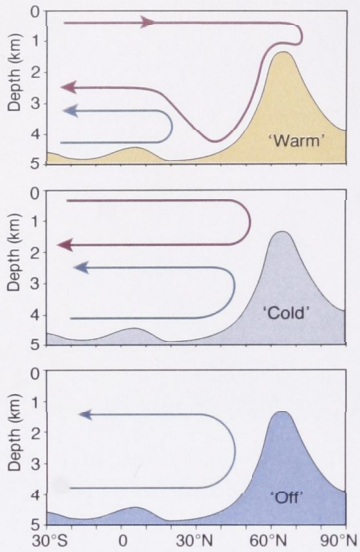

Figure 1.4: Schematic of the three modes of ocean circulation that prevailed during the last glacial period. Shown is a meridional section in the Atlantic; the rise in bottom topography symbolizes the shallow sill between Greenland and Scotland. The circulation of North Atlantic Deep Water is shown by the red line, Antarctic Bottom Water by the blue line. From Rahmstorf (2002).

only mechanism for the maintenance of the abyssal stratification. Balancing a downward vertical volume transport of 30 Sv (Macdonald & Wunsch, 1996) under the Munk (1966) framework requires the average value for the turbulent diffusivity to be $O(10^{-4})\,m^2/s$. Given these values Munk & Wunsch (1998) find that a mechanical energy input of 2.1 TW is required to maintain the abyssal stratification. They calculate an approximate energy budget and find the winds and surface tides to be just able to provide this amount of energy. However measurements find the background turbulent diffusivity to be only $O(10^{-5})\,m^2/s$ (Ledwell *et al.*, 1993; Polzin *et al.*, 1997). While there are regions in the ocean where the turbulent diffusivity is very large, it is not sufficient to yield an average turbulent diffusivity that is an order of magnitude greater than background levels (Polzin *et al.*, 1997). Surface wind forcing can provide energy for turbulent mixing through internal wave generation and Ekman pumping. In particular, the prevailing westerly winds in the Southern Ocean cause a divergence of surface waters that brings NADW from as deep as 1500 m to the surface (Toggweiler & Samuels, 1995, 1998). The upwelled water has been advected to southern latitudes along isopycnals thereby reducing the energy requirement for the turbulent mixing (Webb & Suginohara, 2001).

1.3 Horizontal convection and its relevance to the ocean overturning circulation

There is currently considerable debate over the role of surface buoyancy forcing in the ocean overturning circulation, and studies of horizontal convection have provided much useful insight. The idea that surface buoyancy forcing could play an integral role in governing the MOC is not new. Sandström (1908) was the first to consider whether the Gulf Stream was thermally or wind-driven. He carried out two experiments to investigate this and concluded that "a closed steady circulation can only be maintained in the ocean if the heat source is situated at a lower level than the cold source" (Defant, 1961). This has subsequently become known as "Sandström's theorem." However his reasoning has been shown to be flawed (Jeffreys, 1925) because the effect of diffusion and friction was neglected. Jeffreys (1925) showed that a horizontal gradient in buoyancy forcing gives rise to a horizontal temperature gradient, and therefore flow, because of diffusion. However, the type of flow that arises is considered by some to be "diffusive creep" (Wunsch, 2000). Stommel's (1962) thought experiment aimed to better understand the nature of a circulation driven by a horizontal temperature gradient supplied along the upper boundary of a box. He predicted a highly asymmetric circulation with a small sinking region near one edge of the box and a broad upwelling into a region of rapid temperature variation adjacent to the surface throughout the rest of the box. Rossby, at the request of Stommel, followed up the thought experiment with a laboratory analogue. Rossby (1965) applied a linear temperature gradient to the bottom of a rectangular tank. He observed, as predicted, that a highly asymmetric flow filled the entire tank. Fluid in the thermal boundary layer above the base of the tank flowed towards the destabilising warm region whereupon it gained just enough buoyancy (in a steady state) to rise to the top of the tank. The plume at the endwall was much thinner than the length of the tank. The outflow from the plume ran along the upper boundary and fluid in the interior was slowly advected downwards into the thermal boundary layer. This showed that horizontal buoyancy forcing was able to induce a significant convective overturning. A fusion between surface buoyancy forcing and mechanical input of energy is realised in a more recent theory by Hughes & Griffiths (2006, 2008). They couple an advection-diffusion balance in the interior (cf. Munk & Wunsch, 1998) with a turbulent, entraining slope current for the sinking leg. Turbulent mixing in the interior is assumed to be energized from an external source. This model finds that a background level of turbulent diffusivity of $O(10^{-5})\,m^2/s$ is consistent with a number of observational constraints, including the estimated bot-

tom water formation rate and the top-to-bottom density difference. More horizontal convection studies have been completed and will be reviewed in Chapter 2.

This thesis will present the results of a variety of laboratory and numerical experiments in which convective flows are forced by horizontal differences. The effect of a sill in a box with differentially heated endwalls is studied in Chapter 3. In Chapter 4, Sandström's original experiments are reproduced in order to clarify the contradiction between his conclusion and Rossby's (1965) experiments. High Rayleigh number horizontal convection in a long box with two regions of destabilising buoyancy forcing is studied in Chapter 5. The aim is to gain insights into the interaction of two sinking regions in a convective overturning circulation. In Chapter 6 numerical solutions are reported for the case of two sinking regions, and we examine internal wave activity. Finally, in Chapter 7, we introduce a sill into the horizontal convection experiments with two destabilising regions and investigate how the presence of the sill affects the circulation and stratification.

Chapter 2

Previous work

In the first section of this chapter we review the circulation maintained by differential heating of opposite vertical endwalls in low aspect ratio cavities ($A = H/L$). This serves as background for Chapter 3, in which we add a partial barrier or sill to a rectangular cavity, forced as above, to investigate the circulation and heat transport. We then consider convection driven by differential heating on one horizontal boundary only. In section 2.3 we review relevant convective flows, which are largely driven by salinity differences, but which serve to describe convection in more complex geometries. In section 2.4 we review a range of previous studies more explicitly aimed at understanding the meridional overturning circulation of the oceans, using theoretical, numerical and experimental techniques.

2.1 Convection between heated and cooled walls.

Laminar convection in a two-dimensional differentially heated cavity has been extensively studied for a range of aspect ratios, motivated by a wide range of engineering applications (Bejan, 1980; Bejan & Tien, 1978; Cormack *et al.*, 1974*a*,*b*; Gill, 1966; Imberger, 1974). The Rayleigh number is defined as

$$Ra = \frac{g\alpha\Delta T H^3}{\kappa\nu}, \tag{2.1}$$

where g, is the gravitational acceleration, α, is the coefficient of thermal expansion, ΔT, is the applied temperature difference, H, is the height of the cavity, κ, is the thermal diffusivity and ν, is the kinematic viscosity. In this section we focus our attention on low aspect ratio cavities, for which two distinct flow regimes are apparent (Bejan *et al.*, 1981). The 'parallel core flow' regime exists at low Rayleigh numbers, $0 < Ra < 10^5$, (Cormack *et al.*, 1974*a*,*b*; Imberger, 1974). In this regime the differ-

entially heated endwalls maintain a longitudinal temperature gradient through the interior. The circulation in the cavity interior or 'core' region is described as having 'parallel flow' with the fluid below half depth flowing towards the heated endwall and the fluid above half depth flowing towards the cooled endwall. The flow in the end regions merely turns the parallel core flow through 180°. Not surprisingly, the heat transfer and mass transport occur through the core of the cavity. Cormack *et al.* (1974*a*) derive an asymptotic solution, for $A \ll 1$, for the temperature and flow fields in the core of the cavity, and match this with asymptotic solutions for the flow in the two end regions. They find that the heat transport, measured by the Nusselt number, is a function of the Rayleigh number and the aspect ratio: $Nu \sim 1 + Ra^2A^2$. This analytical result was confirmed by subsequent numerical and experimental studies (Cormack *et al.*, 1974*b*; Imberger, 1974).

The boundary layer regime exists at high Rayleigh numbers, $Ra > 10^7$. A strong boundary layer circulation (figure 2.1) accommodates most of the mass and heat fluxes: a buoyant plume rises up the hot endwall, flows along the top of the box, falls down the cold endwall as a dense plume, and then returns along the bottom of the cavity (Bejan & Tien, 1978; Cormack *et al.*, 1974*b*; Imberger, 1974; Simpkins & Chen, 1986; Simpkins & Dudderar, 1981). Fluid in the core is nearly stagnant and has a temperature field that varies linearly with depth and is independent of horizontal position (Bejan *et al.*, 1981; Simpkins & Chen, 1986). A horizontal temperature gradient is however present across the vertical wall boundary layers.

Bejan & Tien (1978) extended the analytical work of Cormack *et al.* (1974*a*) to larger Rayleigh number and aspect ratio by coupling their solution for the core with integral solutions for the vertical boundary layer flow in the two end regions (which have a very different role to play compared with the parallel core flow regime end regions). For the boundary layer regime Bejan & Tien (1978) predict $Nu \sim Ra^{1/5}$. In the limit of fixed A and $Ra \to \infty$ the circulation is boundary layer driven and the heat transfer relation found by Cormack *et al.* (1974*a*) becomes $Nu \sim A^{-1}Ra^{1/4}$ (Imberger, 1974). The limit of large Ra and Prandtl number, Pr, is reached in the analysis of Blythe & Simpkins (1977), who developed an integral method for solving the boundary-layer equations, and which agreed very well with numerical predictions (Quon, 1972; Stewart & Weinberg, 1972) of the temperature distribution in the cavity. They find the heat transfer to depend on Ra as $Nu \sim Ra^{1/4}$. Bejan *et al.* (1981) completed laboratory experiments in a long shallow box filled with water and found the power law that fits their heat transfer data to be, $Nu = 0.028Ra^{0.35}$, with a slightly larger exponent than any of the other theoretical studies. Bejan (1979) found that the exponent on Ra in heat transfer predictions will be of the order of

1/4, but will approach this value asymptotically as $Pr \to \infty$. This is because solving for the flow using the vertical boundary layer equations assumes there is no vertical heat transfer between the hot and cold horizontal boundary layers, which is not the case for experiments using water and operating in the boundary layer regime.

For even higher Rayleigh numbers the vertical boundary layers can become turbulent (Patterson & Imberger, 1980), but this case is not relevant for the study in Chapter 3. The transition between parallel core flow for low Ra and boundary layer flow for high Ra consists of a circulation that has thin boundary layers and a core with horizontal flow. Both the core and the thin boundary layers are of importance in heat transfer mechanisms.

Simpkins & Dudderar (1981) completed a suite of laboratory experiments over a large range of Ra ($10^3 - 10^6$) and A ($0.11 - 4$). They found empirically that the stream function, ψ, at mid-depth depends on Ra and A for $Ra < 10^4$, but for higher Ra the ψ becomes largely independent of Ra. This is in contrast to numerical and theoretical solutions for the boundary layer regime, which are based on solving the vertical boundary layer equations (Gill, 1966) and find ψ to be independent of Ra and A (Cormack *et al.*, 1974*a*; Gill, 1966; Quon, 1972; Stewart & Weinberg, 1972). The observation was confirmed by Simpkins & Chen (1986). The discrepancy is thought to be due to the neglect of the horizontal boundary layers present in the high Rayleigh number flow, which become increasingly important as the aspect ratio decreases.

The case of high Rayleigh number differential endwall heating in a rectangular cavity with a barrier, or sill, altering the boundary layer circulation that would otherwise be present is explored in Chapter 3. A summary of this work has also been reported in Coman *et al.* (2006*b*).

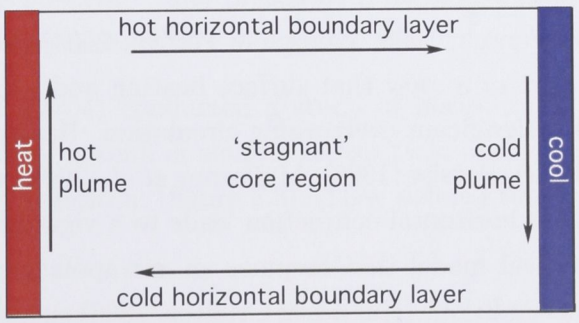

Figure 2.1: Schematic of the boundary layer circulation in a differentially heated box at high Rayleigh numbers.

2.2 Heating and cooling at the same level: horizontal convection

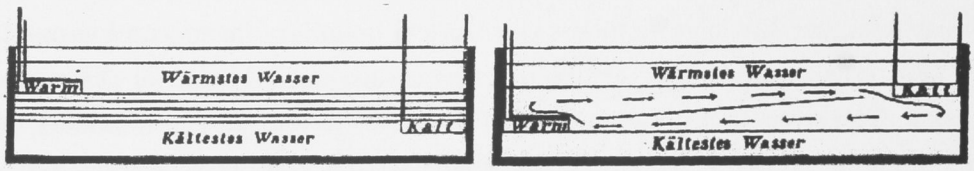

Figure 2.2: Sandström's two experiments reported in 1908. When Sandström placed the warm source above the cold (*kalt*) source he observed no motion and a stable thermal gradient between the sources, illustrated by the isothermal lines in the figure on the left. A clockwise circulation developed when the cold source was placed above the warm source, as illustrated in the figure on the right.

In 1908 a Swedish scientist, J.W. Sandström, carried out two experiments to investigate the oceanographic question of whether the poleward transport of heat in the oceans is forced by the meridional gradient of heating at the ocean surface. He took a long thin tank, filled it with salt water, and placed sources of heating and cooling at each end. The height of each source was varied such that in one experiment the heating source was above the cooling source and in the second experiment the heating source was below the cooling source (figure 2.2). Sandström (1908) reported the observations of the steady state circulation for the two experiments and concluded that "a thermal circulation can only occur if the heat source is below the cold source". The same conclusion was drawn in Sandström (1916), which expanded on the previous experiments to include an experiment where the heating and cooling sources were at the same level.

Others (Munk & Wunsch, 1998; Wunsch & Ferrari, 2004) use this 'theorem' as an argument in support of a view that surface heating and cooling of the oceans is unable to support a significant overturning circulation. However, Rossby (1965), Beardsley & Festa (1972), Rossby (1998), Mullarney *et al.* (2004) and Wang & Huang (2005) have shown that horizontal convection leads to a vigorous overturning flow. A mechanistic theoretical model that assumes an extrapolation of the laboratory observations to ocean conditions (Hughes & Griffiths, 2006) suggests that convection could potentially account for the whole of the measured global overturning rate, and also correctly predicts the top-to-bottom density difference in the oceans. Thus the role of surface buoyancy forcing on the overturning circulation is under contention.

Works that support a major forcing role for buoyancy include Stommel (1962),

who presented a simple convective box model of an idealised ocean. In a thought experiment, a series of vertical pipes connected a large constant temperature abyssal region, having uniform horizontal pressure, to the 'surface' boundary layer. The temperature at the top of each pipe was fixed. Heat could diffuse down the pipes from the surface region and the water in the pipes could move either up or down. He showed that for diffusively dominated and advectively dominated regimes, only the single, coldest pipe carried flow into the bottom reservoir, whereas all the other pipes had upward flow into the surface region. This model illustrates the nature of the strong asymmetry of sinking regions that is observed in both horizontal convection and the meridional overturning circulation.

Further evidence that surface buoyancy fluxes can potentially force large scale circulations was presented by Rossby (1965). Laboratory experiments were conducted in a rectangular tank that was forced by a linear temperature gradient along the base. This arrangement mimics an up-side-down version of the thermal forcing at the ocean surface, though applying fixed boundary temperatures in place of the ocean's mixed boundary conditions. Over the cooler part of the base he observed a stable boundary layer that was advected towards the warmer part of the base where it thickened slightly as it was warmed. At the end of the tank the fluid from the boundary layer rose up the endwall in a thin buoyant laminar plume. This plume turned into a broader outflow layer moving horizontally across the top of the tank. The rest of the interior was slowly moving downward. Rossby's experiments were carried out with moderate Rayleigh numbers, $1 \times 10^7 < Ra < 1 \times 10^{10}$, ($Ra$ based on the applied temperature difference and the tank length) and large Prandtl numbers ($13 < Pr < 8500$) so the flow was laminar for all cases. He found the Nusselt number, Nu, (the ratio of heat transfered by convection over that transfered by conduction) to be $Nu \sim Ra^{1/5}$ and presented a boundary layer analysis that gave the same power law dependence.

Mullarney *et al.* (2004) conducted a study of horizontal convection at higher Rayleigh numbers using a tank of smaller aspect ratio and a piecewise uniform imposed flux boundary condition (figure 2.3). They defined the flux Rayleigh number as

$$Ra_F = \frac{g\alpha F_T L^4}{\rho_0 c_p \kappa^2 \nu}, \tag{2.2}$$

where F_T is the imposed heat flux (W/m^2), ρ_0 a reference density and c_p the specific heat capacity. The flux Rayleigh numbers achieved by Mullarney *et al.* (2004) were $10^{13} < Ra_F < 10^{15}$, or $10^{11} < Ra < 10^{13}$ using a Rayleigh number based on the temperature difference. They observed a similar asymmetric circulation to Rossby,

but at these Rayleigh numbers the overturning flow was more vigorous.

The bottom boundary forcing sets up a horizontal temperature gradient at the base of the tank. A stable thermocline exists above the cooled half of the boundary, which is then advected over the destabilising half of the boundary. The thermocline is subsequently eroded from the base by the destabilising flux, forming a convective mixed layer which grows in thickness until it reaches the top of the thermocline at the end of the box. A narrow turbulent vertical plume then rises up the endwall and forms an unsteady eddying outflow at the top of the tank. The plume always penetrated through the full depth of the tank once the flow had reached thermal equilibrium. Mullarney *et al.* (2004) developed theoretical viscous-buoyancy boundary layer scaling laws which agreed well with their experimental and two dimensional numerical results. The scaling theory followed that of Rossby (1965), modified for imposed flux boundary conditions in place of imposed temperature conditions. The boundary conditions are assumed to be no-slip so that the thermal and momentum boundary layers both scale with the same thickness, h. Fluid in the bottom boundary layer is advected towards the destabilizing end with a horizontal velocity u, and conservation of mass means that this flow is balanced by fluid moving into the bottom boundary layer with vertical velocity, w, over the length of the box, L. Applying the conservation of mass and heat equations to the bottom boundary layer they found,

$$u \sim \frac{wL}{h} \sim \frac{\kappa_T L}{h^2}, \tag{2.3}$$

where κ_T is the thermal diffusivity. The amount of buoyancy needed to move the

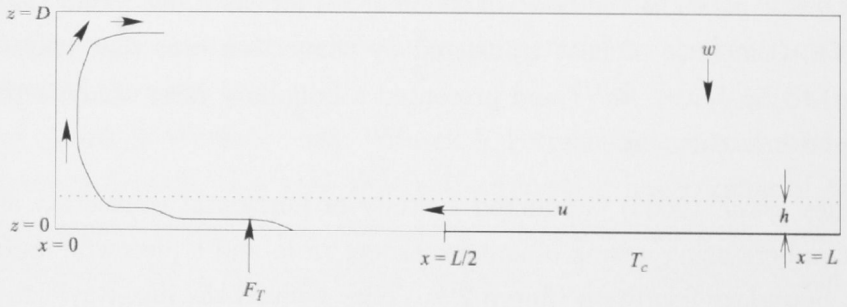

Figure 2.3: Sketch of the flow through a vertical plane in Mullarney *et al.* (2004). A destabilising flux is applied through the bottom boundary between $0 < x < L/2$, a stabilising temperature is applied along the remainder of the box. The dotted line indicates the thermal boundary layer and the solid line indicates the convective mixed layer and the plume boundary. The flow is to the left in the thermal boundary layer, upwards in the plume and there is broad downwelling throughout the rest of the weakly stratified interior.

viscous fluid in the boundary layer is found using the vorticity equation and the scaling in (2.3) to find,

$$\alpha g \delta T \frac{h}{L} \sim \nu \frac{u}{h^2}, \tag{2.4}$$

where α is the thermal expansion coefficient, g is the gravitational acceleration, δT is the temperature difference arising from the applied flux along the lower boundary and ν is the viscosity. The conservation of heat in the boundary layer implies that the flux supplied to the box, over the length L, must be advected through the thermal boundary layer,

$$\rho_o c_P \delta T u h \sim F_T L. \tag{2.5}$$

Using equations (2.3), (2.4) and (2.5), they find the scalings for the normalised boundary layer thickness h, boundary layer velocity u, vertical velocity w, and the Nusselt number Nu:

$$\frac{h}{L} \sim Ra_F^{-1/6}, \tag{2.6}$$

$$\frac{uL}{\kappa_T} \sim Ra_F^{1/3}, \tag{2.7}$$

$$\frac{wL}{\kappa_T} \sim Ra_F^{1/6}, \tag{2.8}$$

$$Nu \sim Ra_F^{1/6}, \tag{2.9}$$

If the Rayleigh number definition is instead based on the temperature difference $Ra = g\alpha\delta T L^3/\nu\kappa$, then equation (2.9) is consistent with Rossby's scaling result for the Nusselt number ($Nu \sim Ra^{1/5}$). Numerical pre-factors in (2.6-2.9) were evaluated empirically.

Outside the bottom boundary layer (the interior) the vertical mass flux carried by the plume is balanced by downward vertical advection throughout the remainder of the box. For a thermally equilibrated flow the interior temperature gradient is steady and is maintained against the effects of vertical advection by thermal diffusion through the depth of the box.

To minimize the heat exchange between the surroundings and the apparatus Mullarney *et al.* (2004) used double glazing on the side walls and thick (at least 5cm) expanded polystyrene foam on all sides of the tank to limit the heat loss to between 2% and 6% of the total flux applied to the heated end (except for their lowest Rayleigh number experiments in which there was a gain from the surroundings).

In more recent experiments Wang & Huang (2005) take a different approach to minimize heat exchange with the surroundings. They used double glazing, but instead of filling the gap with argon gas (as in Mullarney *et al.*, 2004), they created

a vacuum between their tank and another larger box that completely enclosed their tank. Conduction between the apparatus and the room could therefore not occur, just radiative effects, which were minimized by choosing a temperature for the heated end to be just below the room temperature. The interior can then only gain heat from the room (not lose it), and any such heating can only be balanced by additional cooling from the cold source. They find a circulation where the buoyant plume does not penetrate through the full depth of the tank. The plume gains enough buoyancy to rise through the thermal boundary layer but then intrudes into the interior of the tank, just above the boundary layer. They use the term "partial depth circulation" to describe the overturning cell that develops.

The boundary layer thickness, δ, and the overturning cell height, h_c, are measured using the velocity field, which is measured using digital particle image velocimetry (DPIV). The boundary layer thickness is defined as the height at which the horizontal velocity drops to 1% of the maximum velocity in the boundary layer and the cell height is the zonal average of the height at which the oppositely-directed horizontal flow reduces to 1% of the maximum velocity, U, in the intrusion. The thermal boundary layer thickness, δ, followed Rossby's power law for dimensionless boundary layer thickness, $\delta \sim Ra^{-1/5}$, and the dimensionless cell height also followed a $Ra^{-1/5}$ power law. The measurements of bulk mixing, $\kappa_{bulk} = Uh_c^2/L$ (they assumed vertical diffusion is balanced by vertical advection), show that when flow fluctuations exist, such as those that arise in horizontal convection, they lead to a bulk mixing that is higher than the molecular level. They conclude that thermal forcing of the ocean surface could play a dynamical role in the large scale ocean overturning.

Wang & Huang (2005) plot the dimensionless stream function maximum in the boundary layer versus the Grashof number ($Gr_\delta = g'\delta^3/\nu^2$, based on the thermal boundary layer thickness, δ) for their partial depth experiments as well as for the experiments from Rossby (1965), Miller (1968) and Mullarney *et al.* (2004). The data all collapse, showing the results are independent of partial or full depth overturning and further that the dimensionless stream function maximum is insensitive to the details of the bottom boundary condition.

Hughes *et al.* (2007) present a simple model of horizontal convection, based upon the laboratory experiments of Mullarney *et al.* (2004). A localised turbulent line (or point source) plume is assumed to be maintained by a destabilising heat input, q_h, at one end of the base of a long box, with an equal, but opposite, stabilising heat input, q_c, distributed along the entire length of the base (see figure 2.4). The turbulent plume rises through the full depth and entrains fluid from the interior of

the box. The model is therefore much like a 'filling box' (Baines & Turner, 1969), except that there is no net supply of buoyancy to the box volume ($q_h = q_c$). Thus the model is termed a "recycling box," because the density (or buoyancy) is recycled.

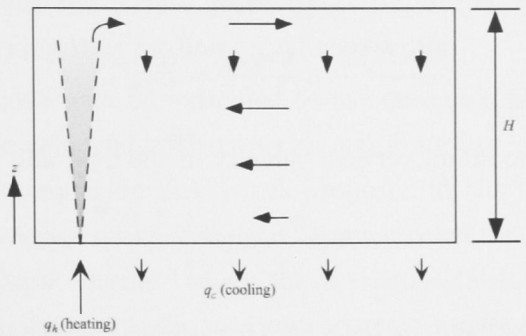

Figure 2.4: Schematic diagram of the recycling box model for horizontal convection, from Hughes *et al.* (2007). Bottom heating and cooling are equal so that a steady flow develops in which a turbulent plume rises through the box depth and forms an outflow along the upper boundary. A distributed down welling occurs everywhere above the bottom boundary layer with entrainment into the plume also occurring.

The two dimensional governing equations for conservation of volume, momentum and buoyancy in the plume were solved by assuming (following Baines & Turner, 1969) the profiles of time-averaged velocity and density anomaly through the plume cross-section are similar at all depths, and depend only on the distance above the plume origin, $z = 0$, and the width of the plume at that height, $r(z)$. The plume grows in width by entrainment of interior fluid and the entrainment constant, E, is the ratio of horizontal velocity into the plume to the vertical velocity at the plume centerline. Conservation of volume and a one dimensional advection - diffusive balance is used to model the interior.

Scalings for the depth of the thermal boundary layer (defined as the thickness incorporating 95% of the top-to-bottom density difference), the top-to-bottom temperature difference and the stream function maximum were derived from the model to compare with the experimental results of Mullarney *et al.* (2004). The multiplying constants all depend, to various powers, on the entrainment constant, E, the heat flux applied to the plume base, q_h, and the thermal diffusivity, κ. The dependence of the thermal boundary layer thickness on the flux Rayleigh number is,

$$\frac{h_{0.95}}{L} \sim Ra_F^{-1/6}, \tag{2.10}$$

for the top-to-bottom temperature difference,

$$\alpha \Delta T|_{max} \sim Ra_F^{5/6}, \tag{2.11}$$

the stream function maximum,

$$\frac{W_e(H)L}{\kappa} \equiv \frac{\psi|_{max}}{\kappa} \sim Ra_F^{1/4}, \tag{2.12}$$

where $W_e(H)$ is the maximum vertical velocity in the box, and the Nusselt number,

$$Nu \sim Ra_F^{1/6}. \tag{2.13}$$

There is excellent agreement between this inviscid solution and the buoyancy-viscous scaling results of Mullarney *et al.* (2004) (compare equations (2.10) to (2.6), (2.13) to (2.9)). The apparent disagreement between equations (2.12) and (2.8) is because the vertical velocity in the latter corresponds to that for the boundary layer, which does not account for entrainment into the plume. If the Hughes *et al.* (2007) scaling for the vertical velocity in the boundary layer is used in place of the scaling for the vertical velocity in the plume, then equation (2.8) would be recovered. Thus scalings for the stream function maximum that are based on the boundary layer analysis (Mullarney *et al.*, 2004; Rossby, 1965) cannot predict the overall maximum stream function in the box.

Hughes *et al.* (2007) suggest the good agreement between their inviscid model and that of the buoyancy-viscous balance in the boundary layer (Mullarney *et al.*, 2004) is due to the fact that in the laboratory and numerical experiments the flow in the interior is essentially inviscid, being driven, in part, by entrainment into the turbulent plume. Continuity must hold across the viscous thermal boundary layer, so the interior inviscid flow imposes strong constraints on the flow achievable in the thermal boundary layer.

This two-dimensional model is able to predict the flow characteristics of the Mullarney *et al.* (2004) experimental work quite well. However, extending the model to an idealised ocean, with a two-dimensional flow and either a line or an axisymmetric plume, gives thermocline depths and top-to-bottom density differences that are much too large. The geometry of the plumes used in the model causes the entrainment into each plume to be much less than the entrainment that would occur in a turbulent plume in the ocean. At depth, a line plume has less area over which to entrain fluid compared to an axisymmetric plume, which in turn has less area compared to a geostrophic slope current (Hughes & Griffiths, 2006). More entrainment

into a plume implies the interior of the domain will be more mixed, the top-to-bottom density difference will be reduced, and the overturning rate will be greater. A more sophisticated geostrophic slope plume model presented by Hughes & Griffiths (2006) (reviewed in section 2.4) gives results that compare quite favourably with ocean data. Thus the plume geometry is important in setting the density structure and overturning rate for horizontal convection.

The theoretical model can be extended to the case of multiple plumes of equal strength, as might be achieved with two regions of surface cooling in the oceans. Using the scaling from equation (2.12) it is proposed in Hughes & Griffiths (2008) that the ratio of the average maximum overturning stream function, $\overline{\psi_{max}}(n)$, within a box containing multiple plumes (where the average is taken over the cells accompanying each of the n plumes) to the maximum stream function for a single plume in the box, $\psi_{max}(n=1)$, (with the sum of input flux held constant and shared equally between the n plumes) scales as,

$$\frac{\overline{\psi_{max}}(n)}{\psi_{max}(n=1)} \sim n^{-1/2}, \tag{2.14}$$

where n is the number of plumes in the box. Similarly, the ratio of the total overturning, as measured by the maximum stream function within a box containing multiple plumes, to the maximum stream function for a single plume in the box will be,

$$\frac{\psi_{max}(n)}{\psi_{max}(n=1)} \leq n^{1/2}. \tag{2.15}$$

The prediction arises from arguing that the total overturning must be less than n times the average overturning associated with n plumes.

2.2.1 Computational studies

Numerical simulations of horizontal convection add to the laboratory studies by extending the range of parameters, such as Rayleigh and Prandtl number, that can be investigated. For the computed flow, the stream function, velocity and temperature fields are easily obtained. Further to this, slightly more complex problems, which are important to understanding the full behaviour of horizontal convective flows, are more easily investigated numerically rather than experimentally. The numerical solutions are also free of unwanted laboratory effects, such as those due to side wall heat loss, and can be used to assess the roles of complications, such as the nonlinear equation of state of water.

Rossby (1998) performed non-rotating, two dimensional, steady state numerical horizontal convection experiments in a square box with a horizontal temperature difference applied at the base. Importantly, the scaling result from Rossby (1965), $Nu \sim Ra^{1/5}$, was confirmed for a larger range of Rayleigh number ($10^3 \leqslant Ra \leqslant 10^{10}$). A one-fifth power law relationship between the maximum stream function, ψ, and Nu is also measured for $Ra > 10^5$. The computational approach enabled an investigation into the effects on ψ and Nu of a variation in Prandtl number ($1 \leqslant Pr \leqslant 100$). For $Ra \geqslant 10^7$ and Pr between $10 - 100$, ψ and Nu showed no dependence on Pr, but for $Pr < 10$ and approaching 0, ψ increases rapidly while Nu decreases slightly. The transient response of the convection to a slight change in the bottom thermal boundary condition was also explored and was found to depend upon where the change was applied. If either an increase or decrease was made to the warmer part of the base the change directly affected the temperature field in the interior. If the change is made to the cooled part of the base this is quickly communicated by the boundary layer flow to the heated section, and the boundary layer adjusts to the new conditions without affecting the interior temperature field. It was concluded that the temperature of the fluid at the base of the plume sets the average temperature of the box and that the time scale to reestablish a steady state is much shorter if the adjustment is made to the cooled part of the base rather than the warmed part. However, recent experiments in our laboratory have shown very little difference between the adjustment time scales following a change applied to the heated or cooled portion of a horizontal convection experiment (using an apparatus similar to that described in Mullarney *et al.*, 2004).

Paparella & Young (2002) derive an expression for viscous dissipation rate and the 'anti-turbulence' theorem, namely that as viscosity and thermal diffusivity approach zero, with Pr held constant, the dissipation of mechanical energy approaches zero. They reported two dimensional numerical horizontal convection experiments in a long box ($H/L = 1/4$) with non-conductive boundaries, except the upper boundary, which has a non-uniform temperature condition such that a sinking plume is created in the centre of the box. For $Pr = 1$, they find a steady solution for $Ra < 3 \times 10^6$ and an unsteady, eddying plume for $Ra > 3 \times 10^6$. For $Ra = 10^8$, a steady flow occurs for $Pr > 1$ and unsteady flow evolves for $Pr < 1$. Nevertheless, Paparella & Young (2002) conclude that horizontal convection is not 'truly turbulent' according to the law of finite energy dissipation.

Mullarney *et al.* (2004) complemented their laboratory experiments with two dimensional numerical simulations using experimental geometries and ideal boundary conditions. They found excellent agreement between the laboratory and numerical

flows. Due to the two dimensional nature of the flow the convective mixed layer (which in the experiments contained three dimensional turbulence) is resolved as two dimensional 'rolls.' The computed results follow the boundary layer scaling derived in the same paper but the experimental results and computations have slightly different multiplying factors. This is thought to be due to the forced two dimensional convective mixed boundary layer and/or the genuinely insulating boundary conditions on the side, end and upper boundaries in the numerical calculation.

Upper bounds on the viscous dissipation rate and the horizontal Nusselt number are developed for horizontal convection by Siggers *et al.* (2004). They find the upper bound on the Nusselt number to be $Nu \sim Ra^{1/3}$. In the limit $Ra \to \infty$ they predict the boundary layer next to the forcing boundary to have a thickness no greater than $O(Ra^{1/3})$ and in the same limit the temperature gradient in the interior will vanish. In addition to the theory they also complete numerical horizontal convection experiments in a square cavity with a sinusoidal variation of imposed flux at the surface. They find the relationship between the Rayleigh number and the Nusselt number to be $Nu \sim Ra^{1/5}$, in accord with the Rossby scaling and smaller than their upper bounds. They conclude that either the bounds are not very tight or that horizontal convection experiments are yet to reach the asymptotic regime of $Ra \to \infty$.

Mullarney *et al.* (2006) used the numerical model developed in Mullarney *et al.* (2004) to investigate the effect of an additional flux being applied to the horizontal boundary opposite the main forcing boundary. A destabilising flux through the upper boundary equates to the situation of geothermal heating (which is destabilising to the water column) through the bottom of the ocean. The maximum time-averaged stream function showed that an experiment with a destabilising flux of 10% of the total heat transport had 2.5 times as much overturning as the case with no destabilising forcing through the upper boundary.

The application of horizontal convection to the meridional overturning circulation of the oceans will be reviewed in section 2.4. Next we review other convective flows that give some insight to the dynamics of a convective circulation in the presence of multiple plumes and topographic sills.

2.3 Other convective flows

We have reviewed convective flows driven by horizontal density differences due to temperature. However, horizontal density differences have also been established in previous work on horizontal convection by introducing sources of salty and fresh

water at the surface of a tank of fluid, creating a surface salinity dipole. The salinity fluxes from each source are matched so that the net buoyancy input is zero. However, the volume of fluid in the tank will increase (or in some cases the excess is removed and the volume kept constant) because the sources are continually introducing new fluid into the tank. Thus a steady state is reached in which the average density is set by the average of the two source densities. The use of salt, compared to heat, allows for larger density differences and buoyancy fluxes, hence the achievement of higher Rayleigh numbers. Importantly, salinity and thermally driven turbulent plumes are both governed by coupling between plume buoyancy, entrainment and the background stratification, and these determine the plume outflow, regardless of the thermal or haline nature of the density difference. In addition, convection forced by differential heating at one boundary, or at opposite endwalls, has not been examined with sills or when multiple plumes result. Nevertheless, some relevant lessons can be learnt from experimental studies that create turbulent plumes using salt. In particular, we review in section 2.3.2 flows containing single and multiple turbulent plumes in basins of finite volume, and in section 2.3.3 a flow containing multiple turbulent plumes with a sill. These latter laboratory experiments do not contain salinity dipoles, therefore there is a net buoyancy input to the tank, preventing the flows from reaching a steady state.

2.3.1 Flows with surface dipole salinity forcing

Pierce & Rhines (1996) build a pycnocline in a laboratory experiment by introducing a dense source at the surface of a long rectangular box and a light source at the opposite end. The volume in the tank is kept approximately constant by extracting fluid from four locations along the length of the tank, between the light and dense sources. A control experiment was run in a rectangular tank. Initially the dense source formed fluid that sank though the tank as a dense turbulent entraining plume. Once light water spread across the surface of the tank and created a surface layer this fluid modified the sinking plume and reduced the density of the plume source water. When a slope was introduced beneath the source of dense water, entrainment was inhibited and the entrainment coefficient was reduced in comparison to a free falling plume (Turner, 1973). The reduction in entrainment causes the salinity maximum at the bottom of the tank to be larger than in the control case and as the plume entrains lighter surface water it "lifts-off" the slope and intrudes at successively higher and higher depths. A simple numerical plume model showed that after a diffusive time scale the density of the bottom water was reduced through diffusion

until the plume was able to penetrate through the full depth again. The control case with no bottom topography was also run in a rotating environment. The final stratification was very similar to the non-rotaing case, the main difference was in the manner of the approach to the final state. Overall three time scales were described: an advective time scale which characterises the time for the light water to spread across the surface of the tank and start to modify the dense source water, a short diffusive time scale by which time the surface fresh layer has come into diffusive equilibrium with the underlying interior fluid and therefore the light surface layer can begin to increase the deep density flux. The final time scale is a long diffusive time scale, which characterises the time for diffusion to act on the densest water that has pooled at the bottom so that the entraining plume will penetrate through the full depth. The last time scale could not be achieved in the laboratory as it was too long ($\sim$ 1 year).

Whitehead & Wang (2008) conduct a similar experiment to Pierce & Rhines (1996) with the addition of a stirring rod extending through the tank depth that provides mechanical energy to drive turbulent mixing. The long diffusive time scale from Pierce & Rhines (1996) is reduced in these experiments by the turbulent mixing of salt. Whitehead & Wang (2008) introduce, at the surface and at opposite ends of a long rectangular box, a source of saline water and a source of fresh water. A spillway in the centre of the box maintains tank volume and removes fluid of the average density of the two sources. A steady state circulation developed in which the source of dense water fed a turbulent, entraining plume which penetrated through the full tank depth and had an outflow along the bottom boundary. The source of light (fresh) water spread across the surface and was mixed downwards by the turbulent mixing behind the stirring rod. A thermocline and abyssal region were formed, the former having a much stronger stratification. It was found that the potential energy fluxes associated with plume and the mechanical mixing are in approximate balance. It is suggested that if the potential energy of the ocean is steady, as it was in the experiments, then this balance will also hold in the ocean. Estimates of the potential energy fluxes associated with ocean plumes and turbulent mixing suggest the balance is possible.

Pierce & Rhines (1997) conduct non-hydrostatic and hydrostatic numerical simulations of their earlier laboratory experiment. The comparison of the two realisations provides insight into the importance of modeling the convective process. A box filled with water is forced from the upper surface by a dipole of buoyancy fluxes, a fresh source near the left end and a dense source near the right end. In comparison to the laboratory experiment the numerical calculation achieves a no net volume flux

condition. The circulation for the non-hydrostatic model involves a periodic deep sinking event because the surface fresh water periodically caps the deep sinking region and the water must densify before it is able to penetrate into the interior. The interior circulation consists of an asymmetric clockwise circulation cell in the upper half of the box, in which the plume intrudes at a partial depth with broad upwelling over the remaining box cross-section and entrainment into the upper portion of the plume. Some flow reaches the bottom of the box when the plume is actively sinking. If a hydrostatic assumption is made (as in ocean GCM's) the model did not show the intermittent plume behaviour. This was due to the use of a 'convective adjustment' scheme in which convective instability was parameterised by a high local eddy diffusivity, resulting in vertical mixing in a few time steps. This leads to a plume that consistently reached through the full depth of the box and highlights the importance of accurately modeling small-scale convective processes in order to resolve large-scale variability in ocean circulation.

2.3.2 "Filling box" flows with multiple sinking regions

Baines & Turner (1969) showed that a descending plume (maintained by a destabilising buoyancy flux) in a confined region leads to the formation of a density stratification. The turbulent, entraining plume sank and subsequently spread along the bottom of the tank. Water in the outflow at an earlier time was slowly upwelled to shallower depths by the continued outflow of slightly denser water from the plume (which is always increasing in density). The plume entrains the upwelling fluid at all levels above the plume outflow. The establishment of a stratification in this manner was termed the "filling-box" process. Killworth & Turner (1982) showed that a descending plume in a confined region driven by a time-varying buoyancy source also leads to the formation of an ambient density stratification. The plume initially enters the tank of uniform density fluid and, over many forcing cycles, the subsequent penetration of the densest water to the bottom of the tank establishes a background stratification. When the forcing is at its maximum the plume penetrates through the stable stratification, spreading horizontally at the plume's neutrally buoyant level, or at the bottom of the tank. When the forcing is reduced the plume retreats towards the surface, and when the forcing is at its minimum the plume spreads out horizontally at the surface. The maximum value of the time-varying buoyancy source sets the stratification. The stratification in the interior was found to be very similar to the stratification predicted by Baines & Turner (1969) for a steady turbulent plume based on the maximum buoyancy flux.

Wong & Griffiths (1999) investigate the convection and stratification produced by two turbulent plumes of unequal buoyancy fluxes in the same box. Their two plume "filling box" theoretical predictions and experiments showed that the density profile and the circulation pattern was dominated by the stronger plume. For large times, the weaker plume intruded into the stratification at a depth dependent on $(F_{weak}/F_{strong})^{2/3}$, the ratio of the plume buoyancy fluxes to the 2/3 power.

Hydrographic data show that the sinking in the southern hemisphere forms the Bottom Water for the worlds oceans. "Filling box" models have shown that for a basin with two sinking plumes, the plume with the strongest buoyancy flux will reach the bottom and control the top-to-bottom density difference (Baines & Turner, 1969; Wong & Griffiths, 1999) and under oscillating conditions the maximum buoyancy in the forcing cycle sets the stratification (Killworth & Turner, 1982). This implies that the sinking near Antarctica is presently the strongest. The sinking in the northern hemisphere forms North Atlantic Deep Water (NADW) which intrudes above the Antarctica Bottom Water (AABW) and thus must have weaker buoyancy flux than the plume feeding the AABW. The level at which NADW intrudes into the stratification (which is presently controlled by the southern hemisphere plumes) will depend on the buoyancy of those waters. We might expect that the NADW intrusion level will be very sensitive to changes in the forcing of the plume feeding that intrusion. Understanding how each sinking region affects the overall circulation and how the surface forcing interacts with individual sinking regions is required to discover how sensitive the current ocean circulation is to changes in surface buoyancy forcing.

2.3.3 Flow over a sill

Wong & Griffiths (2001) study the convective circulation driven by multiple sinking regions in the presence of topography. The set-up consisted of a rectangular box with the lower depths separated into two basins by a partial barrier or sill (see figure 2.5). The height of the sill and the ratio of basin sizes was varied and there was one plume sinking into each basin. The flow was characterized by different stratifications in each basin and by an overflow from one basin into the other. Figure 2.5 shows the four different flow regimes found for the two plume, two basin arrangement. Regime 1 is not a steady state regime, the first fronts of each of the descending plumes are yet to reach the barrier height and therefore both plumes descend to the bottom of their respective basins. Regime 2 is a final state for certain values of the normalised sill depth, $\zeta_s = z_s/H$, and flux ratio, Φ. Here H is the box height and

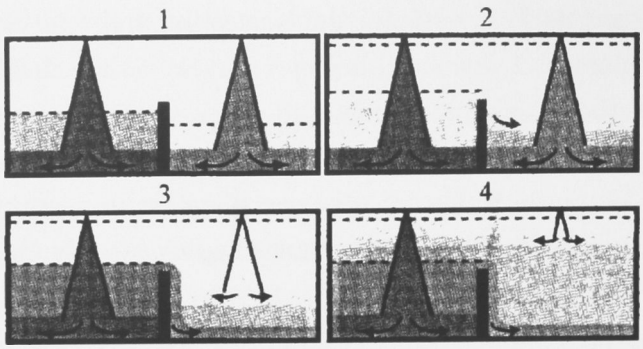

Figure 2.5: Four flow regimes for the two basin, two plume arrangement considered in Wong & Griffiths (2001).

z_s is the height of the gap above the sill, and Φ equals the weaker plume buoyancy flux divided by the sum of the plume fluxes, see area D in figure 2.6. The overflow is from the first basin (which, by definition, always contains the stronger plume) into the second basin, but the overflow intrudes above the bottom outflow of the weaker plume. The third regime is the final state for mid values of ζ_s and Φ, see areas B and C figure 2.6. The overflow is now denser than the outflow from the weaker plume, which is forced to intrude above the overflow spreading at the bottom of the second basin. The fourth regime is the final state for the special case of no sill ($\zeta_s = 1$) and for larger values of ζ_s if Φ is also small enough (area A in figure 2.6). For this regime the weaker plume is prevented from penetrating the second basin by the strength of the intruding overflow and so intrudes into the common region above the sill height.

In a steady state the direction of the overflow is always from the basin with the stronger plume to that with the weaker plume if $\alpha < 2$ or if $2 < \alpha < 10$ and $\Phi < 0.3$, where α is the area of the first basin divided by the second. If the second basin is small ($\alpha > 2$) but the flux driving the weaker plume is at least a quarter of the total buoyancy flux then the overflow is from the second basin into the first. For the transient flow, the filling time for each basin governs the initial direction of the overflow. Thus two buoyancy sources and a single topographic sill can lead to a rich range of flow behaviour.

2.4 Models of the meridional overturning circulation

There are two forces that may drive the mean large scale overturning circulation: wind stress and surface buoyancy gradients. This thesis examines horizontal buoyancy forcing and its ability to produce an overturning circulation. However, a large part of the literature discounts surface buoyancy forcing as a means of supporting

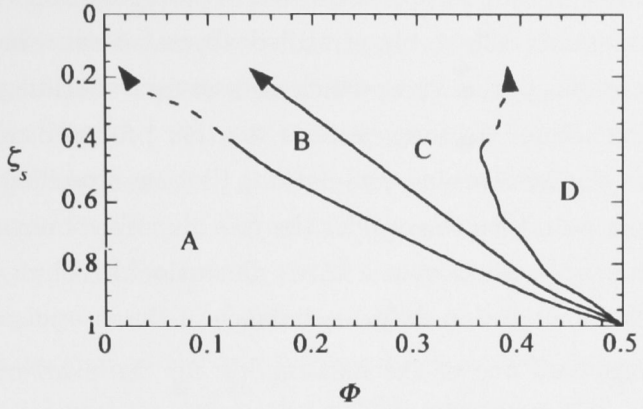

Legend

Area	Regimes from start to steady state
A	1 to 3 to 4
B	1 to 3
C	1 to 2 to 3
D	1 to 2

Figure 2.6: Flow regime phase diagram for basins of equal size for the two plume, two basin arrangement considered in Wong & Griffiths (2001). The lines represent boundaries between the regimes having differing temporal evolutions and final steady states. Refer to figure 2.5 for definition of regimes.

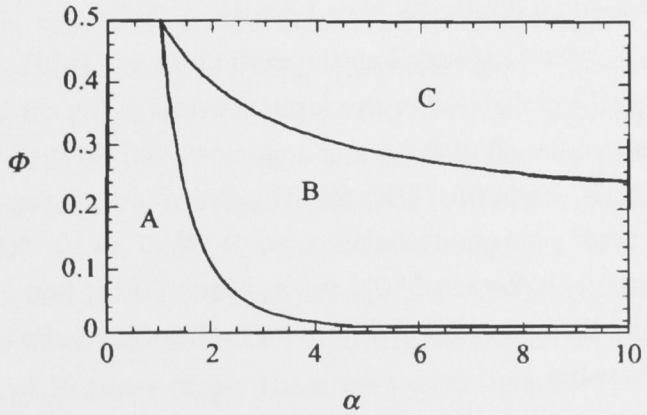

Figure 2.7: Phase diagram for the direction of the sill overflow for the two plume, two basin arrangement considered in Wong & Griffiths (2001) with a sill of half depth. α is the area of the first basin divided by the second, and Φ is the ratio of the weaker plume flux to the sum of plume fluxes. In area A the overflow is always from the first basin into the second. In area B the flow is initially from the second to the first basin but in the steady state the overflow is from the first to the second basin. In area C the overflow is always from the second basin into the first.

the meridional overturning circulation because it is perceived that it cannot provide enough energy to maintain the stably stratified abyssal ocean. In this section we review the modern origins of this view, which also serves to outline the need for turbulent mixing in the ocean. We then examine another proposed major mechanism that contributes to the overturning circulation, Ekman upwelling due to surface wind forcing. Finally we return to consider the role of surface buoyancy forcing and review work which couples sinking in a three dimensional turbulent slope current with a two dimensional advection-diffusion balance in the interior of the domain.

Munk (1966) proposed one of the first models for the overturning circulation of the abyssal ocean. In this model the bottom water is continually produced in the sinking regions and subsequently upwelled in the abyss. To keep the abyssal stratification intact there must be a matching downward diffusion of heat to balance the upward advection of abyssal waters. He assumed a one dimensional advection-diffusion balance in the interior of the ocean between 1 km and 4 km depth,

$$\omega \frac{\partial \rho}{\partial z} = \kappa \frac{\partial^2 \rho}{\partial z^2}, \tag{2.16}$$

where ω is the vertical upwelling speed, ρ is the density and κ is the diffusivity, see figure 2.8*a*. Using temperature, salinity, carbon-14 and oxygen profiles from the Pacific Ocean and equation (2.16) Munk (1966) found an average upwelling velocity of $\approx 1.4 \times 10^{-7}$m/s and a diffusivity of $\approx 1.3 \times 10^{-4}$ m^2/s.

Munk & Wunsch (1998) expanded on the work of Munk (1966). They take 30 Sv (1 Sv = 10^6m^3/s) as the global deep water formation rate in the ocean (Macdonald & Wunsch, 1996) and require all of this water to be upwelled through the full depth of the abyss, to the 3.5°C isotherm. They find the downward mixing of heat required to balance the upward advection of dense (cold) water to be characterised by a turbulent diffusivity of the order of 10^{-4} m^2/s. Munk (1966) and Munk & Wunsch (1998) therefore find the bulk vertical diffusivity in the ocean to be 1000 times larger than the molecular value.

For the rate of vertical diffusion in the ocean to be larger than the molecular rate of diffusion there must be a dynamic mixing process operating, such as turbulence. In addition, Munk & Wunsch (1998) consider the pelagic (open ocean) diffusivity can be supported by the internal wave spectrum. Eddy diffusivities much larger than molecular values indicate that there will also be a large viscous dissipation of energy and a large supply of energy to turbulence.

Munk & Wunsch (1998) explore the sources of energy for the turbulent mixing, considering winds, tides and geothermal heating from the mantle. Energy supply

from surface buoyancy fluxes was neglected on the basis of "Sandstrom's Theorem". The domain of their model excludes the upper one kilometer of the ocean, and focuses only on processes in the abyssal ocean (from 1 km down to 4 km beneath the surface). Using 1×10^{-4} m^2/s as an average value for the turbulent diffusivity of the global oceans and assuming a mixing efficiency of 0.2, they calculate roughly 2 TW of power is required for mixing in the abyssal ocean. Geothermal heating was found to supply a negligible amount of the required power. It was concluded that the winds (through generation of internal waves radiating from near the surface and from the interaction of the wind-driven large scale geostrophic motions with bottom topography) and the tides (through the generation of internal tides from the interaction of surface tides with ridges and seamounts) can provide the power required to maintain the abyssal stratification. It was conceded that outcropping isopycnals due to Ekman upwelling in the southern abyssal ocean may reduce the energy required to sustain the overturning circulation, but more investigation was required. We explore this mechanism later in this section.

The findings of Munk (1966) motivated oceanographers to find out where and how the vertical turbulent mixing was occurring. Direct measurements of "microstructure" (small scale fluctuations of temperature and velocity) have provided estimates for dissipation rates of thermal variance and of kinetic energy. "Finestructure" parameterizations have evolved out of microstructure measurements. These relate shear stress and strain in the oceanic internal wave fields, measured using conductivity-temperature-depth (CTD) instruments and acoustic doppler current profilers (ADCP), to dissipation rate. Microstructure measurements yield data along ship tracks and therefore these estimates of mixing rates or diffusivity give only sparse spatial coverage of the oceans. Values of the diffusivity measured by these methods are $O(10^{-5})$ m^2/s (Ledwell *et al.* 1993; Gregg 1989; Rudnick *et al.* 2003). Algebraic or statistical inversion techniques applied to hydrographic and climatological data allow for basin scale diffusivity averages to be obtained. However the values are on the order of 10 times bigger than those from microstructure measurements (Ganachaud & Wunsch, 2000).

Munk & Wunsch (1998) account for the difference between their prediction and the ocean measurements of turbulent diffusivity of $O(10^{-5})$ m^2/s by concluding that the pelagic (open sea) mixing is enhanced by regions of high turbulent diffusivity around topography. However, Webb & Suginohara (2001) argue that while there are regions in the ocean where the turbulent diffusivity is very large, they are not sufficient to yield an average turbulent diffusivity that is an order of magnitude greater than background levels. While there is not a clear consensus on the magni-

tude of the turbulent diffusivity in all parts of the ocean, it is clear that the simple advection-diffusion model of the ocean interior is not a complete story in describing the basin sized ocean overturning. Therefore we now explore the contribution of Southern Ocean wind forcing.

The divergence of surface waters in the Southern Ocean, driven by the westerly winds blowing along 40-60°S, brings water from below the thermocline, predominantly NADW, to the surface (Toggweiler & Samuels, 1995, 1998). The water that is predominantly brought to the surface by this process comes from NADW depths because the highest meridional boundary in the Southern Ocean is that of the Drake Passage sill. Gnanadesikan (1999) and Gnanadesikan *et al.* (2007) investigate numerically the effects of Southern Ocean wind forcing (see also the review by Kuhlbrodt *et al.*, 2007). Their domain of study only extends between the latitudes of North Atlantic sinking and the southern latitudes of Ekman upwelling ($\sim 50°$S) and from the surface down to ~ 4000 m. The AABW is therefore not included in these models. Nevertheless, models of this kind show that the Southern Ocean winds play a critical role in the location of the upwelling in the Southern Ocean. If there are no westerlies then the majority of the upwelling from depths > 1000 m occurs in the mid latitudes. However when the models are run with southern ocean wind forcing much of the upwelling shifts to the region of measured surface divergence. In fact, Ekman upwelling in the Southern Ocean has been proposed as capable of carrying a large percentage of the volume flux of the MOC (Nycander *et al.*, 2007). In this view (see figure 2.8*b*) the surface water in the North Atlantic loses heat to the atmosphere and becomes salty through evaporation as it flows northward. The surface water then sinks to abyssal depths in the North Atlantic basin and flows southwards. This NADW must return to the surface and Nycander *et al.* (2007) suggests that wind-driven upwelling is a major contributor. At the latitudes and depths where the Antarctic Bottom Water (AABW) and the North Atlantic Deep Water (NADW) meet, the NADW intrudes above the AABW. Ekman pumping then causes the NADW to be upwelled along the isopyncals that outcrop at the surface in the Southern Ocean. The outcropped water is modified by near surface mixing and flows northward in the Ekman transport layer. Some of the upwelled water may also move southwards, to be cooled and form part of the water mass that sinks to depth and contributes to Antarctic Bottom Water. The deep sinking off the Antarctic coast is not explicitly included by Nycander *et al.* (2007). However they, and others (e.g. Webb & Suginohara, 2001), see a role for the deep sinking in the Southern Ocean Ekman upwelling model. The formation of AABW places water below the NADW. The AABW only needs to be mixed from the bottom of the ocean up to the

level of the NADW (which is subsequently upwelled) and not all the way through abyss and into the thermocline. If this is the case then much less mechanical energy input is required and Munk's one dimensional advection-diffusion model need not be applied to the full depth of the abyssal ocean. Samelson (2004) also explores the middepth meridional overturning by Ekman pumping processes.

The sinking plumes in the Southern and Northern Hemispheres transport $10 - 30\,\mathrm{Sv}$ and $\sim 13\,\mathrm{Sv}$, respectively, into the abyssal ocean (Dickson & Brown, 1994; Macdonald & Wunsch, 1996; Orsi *et al.*, 2002). Including these regions of deep sinking in ocean models is therefore essential to a full understanding of the dynamics and driving mechanisms of the MOC.

Hughes & Griffiths (2006) develop a conceptual model of a convective ocean overturning by coupling a single three dimensional sinking region with a two dimensional advection-diffusion balance in the interior (which allows for horizontal entrainment flow into the dense current) to close the circulation, see figure 2.8*c*. The forcing in this model is from a point source cooling flux (for analytical simplicity) and a matching but uniformly distributed heat input over the whole surface. The cooling flux results in a single localized turbulent plume sinking down a sloping boundary to the bottom of the otherwise rectangular ocean basin. The plume entrains water as it sinks. There is no net heating in the model so that the system is in a steady state. The temperature distribution in the interior is maintained by a balance between downward vertical diffusion of heat and upwelling of cold water, similar to an earlier model of the Red Sea (Manins, 1973). The diffusivity is assumed to be uniform and the upwelling velocity can vary with depth due to the entrainment of interior water into the plume. Rotation is included and the slope current is assumed to be approximately in geostrophic balance.

Hughes & Griffiths (2006) compare their model results with ocean observations, as a function of vertical diffusivity, buoyancy input and slope current entrainment constant. They use best estimates of the single hemisphere surface cooling flux ($2 \times 10^{15}\,\mathrm{W}$, Houghton *et al.*, 1996, p. 212), the angle of the slope current to the horizontal ($0.1°$), the surface area of the global ocean ($3.6 \times 10^{14}\,\mathrm{m}^2$) and an average ocean depth ($3780\,\mathrm{m}$). They use typical values for the sea water density ($1025\,\mathrm{kg/m^3}$), specific heat capacity ($3990\,\mathrm{J/kg/K}$), coefficient of thermal expansion at $-2°\mathrm{C}$ ($2.54 \times 10^{-5}\,\mathrm{K}^{-1}$) and the Coriolis parameter, corresponding to a latitude of $70°\,\mathrm{S}$ ($1.37 \times 10^{4}\,\mathrm{rad/s}$). They find that the density profile through the depth of the ocean is reasonably predicted for a diffusivity of $10^{-5}\ \mathrm{m}^2/\mathrm{s}$, giving only a slightly weaker gradient in the thermocline than averaged profiles for the northern and southern hemispheres (figure 2.9). The horizontally averaged top-to-bottom

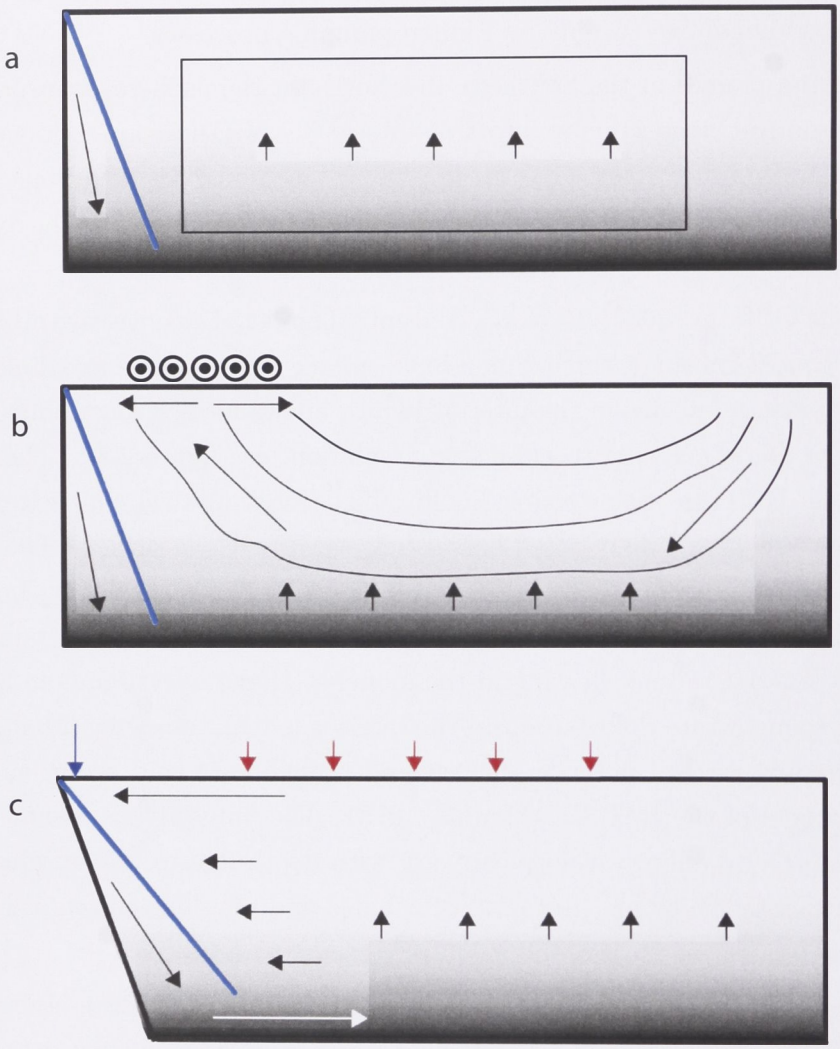

Figure 2.8: Schematic representation of various models for the meridional overturning circulation. a) Munk 1966 1D advection-diffusion model. The inside rectangle represents the region of their model. b) The Southern Ocean westerlies (dots out of the page) driving Ekman upwelling of NADW with the formation of Antarctic Bottom Water included in the Southern hemisphere. c) Hughes & Griffiths (2006) model. Light shading implies least dense waters, dark implies most dense waters.

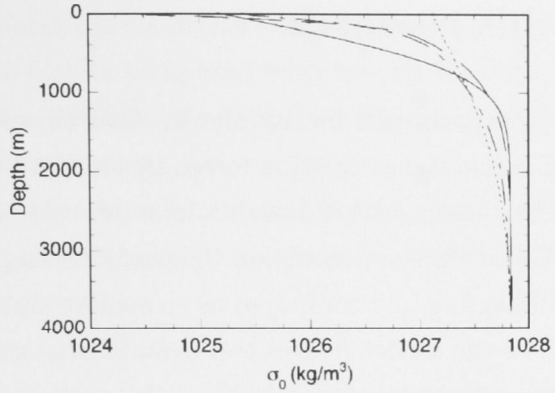

Figure 2.9: Density profiles predicted by the recycling box model from Hughes & Griffiths (2006) using values of 10^{-5}, —, and $10^{-4}\,\mathrm{m}^2/\mathrm{s}$, - - - . Potential density profiles averaged from the Levitus 1994 dataset for the northern (— —) and southern (— - —) hemisphere oceans are also shown for comparison.

density difference agrees well with the observed value. A diffusivity of 10^{-4} m^2/s gives a thermocline depth that is too deep and a top-to-bottom density difference that is too small (figure 2.9). Predictions for the slope current properties (e.g. buoyancy frequency profile, slope current width, thickness (above 2000m), along stream velocity and density, the upwelling velocity and entrainment flux) are more reasonable with the lower value for the vertical diffusivity. The overturning rate predicted for this diffusivity, assuming no wind forcing, was $\sim 18\,\mathrm{Sv}$ which is consistent with the rates inferred from ocean data (Cunningham *et al.*, 2007). The energy source for the turbulent mixing required to achieve the vertical diffusivity is not specified in this model, but was envisaged to be the winds and tides. For a diffusivity of $\kappa \sim 10^{-5}\,\mathrm{m}^2/\mathrm{s}$, which yields predictions that are consistent with a wide range of observational constraints, the requirement is an order of magnitude smaller that that suggested by Munk (1966) and Munk & Wunsch (1998). Thus this model illustrates the way in which buoyancy forcing and entrainment into turbulent sinking regions might contribute to the ocean overturning circulation.

In summary, the ocean overturning circulation is still poorly understood. Understanding how the flow in the abyss is related to the forcing at the surface is one of the main challenges to accurate and predictive modelling capability. In this thesis we extend previous idealised laboratory convection experiments to investigate the effects on the overturning circulation of two sinking regions and topographic sills. We also examine the internal wave field generated by the convection.

2.5 Aim of this research

There are four series of experiments in this thesis. Overall we aim to learn more about the dynamics of horizontal convection forced by steady differential heating at the surface, and thereby obtain further insights into the role of convective forcing in ocean circulation. We restrict our attention to steady forcing conditions and use a simple distribution of heating and cooling so as to achieve sinking plumes at both ends of a long box. Thus the model creates two destabilising regions, which mimic the destabilising regions currently existing in the polar regions of the northern and southern hemispheres. We also explore the influence of a sill that divides the box into two basins both in horizontal (surface forced) convection and in the case of endwall heating and cooling.

In Chapter 3 we examine the influence of a barrier on the flow within a rectangular cavity forced by heating and cooling at opposite vertical ends of the cavity. The horizontal temperature difference forces a horizontal baroclinic exchange above the barrier, and maintains a stratification throughout. We describe how the steady-state convective flow changes as a function of the barrier's height and position, and present measurements of the modified heat and mass transports in the cavity. The results provide insights into a range of flows that are affected by barriers, including natural ventilation in buildings and geophysical flows. While this forcing arrangement is not directly relevant to the ocean, the contrast with surface heating and cooling serves to highlight some of the important and distinctive features of horizontal convection.

In Chapter 4 we re-examine the classical experiments reported by Sandström (1908, 1916). Sandström's laboratory experiments included convection with heating and cooling at the same geopotential level. His conclusions have had a large impact on subsequent oceanographic work. For example, Munk & Wunsch (1998) and Wunsch & Ferrari (2004) interpret Sandström's work as implying that heating and cooling at the ocean surface is unable to drive a significant convective circulation in the oceans. Sandström's observations are however inconsistent with more modern reports of horizontal convection. Thus we replicate Sandström's experiments in order to explain this discrepancy and resolve this fundamental impasse. A summary of this Chapter has also been reported in Coman *et al.* (2006*a*).

In Chapter 5 we report experiments in a simple long rectangular box, where the base of the box is forced by cooling in a central region and heating near each end, producing two buoyant plumes. These experiments represent the first reported thermally-forced horizontal convection experiments with two plumes. We explore the flow for a range of input flux differences between the two destabilisng regions and

examine whether a steady flow exists. Computational simulations are also reported in Chapter 6 and the results compared with the experiments. The computed flow solutions highlight the existence of internal wave motions excited by the convection and their feedback onto the flow.

The final series of experiments reported in Chapter 7 combines elements of the other experiments by including a simple topographic sill in the horizontal convection experiment with two plumes.

Chapter 3

Experiments with thermal forcing at the endwalls

Here we report experiments with laminar free convection in a box with differentially heated endwalls and which is partially divided by a barrier, or sill, into two connected chambers. We investigate how the steady-state circulation, the temperature field and the transport of heat and mass depend on the height and position of the barrier.

3.1 Experiments

3.1.1 Experimental apparatus and procedure

The experiments were carried out in a tank, of length $L = 302$ mm, height $H = 196$ mm and width 150 mm, filled with de-aired water (figure 3.1). The base, lid and sidewalls of the tank were acrylic, with heat exchangers as endwalls. Each heat exchanger was kept at a constant temperature by recirculating water from a temperature-controlled bath. The temperature in the heat exchangers was monitored using embedded thermistors. The endwalls had temperatures of 50 °C and 5 °C, giving an applied temperature difference ΔT of 45°C. Holes along the length of the tank in the centre of the lid enabled temperature measurements and flow visualisation. This procedure ensured all visualisation and measurements were subject to minimal influence from the sidewalls. Barriers, of the same width as the tank and of various heights h, were inserted across the tank at the bottom so as to create two connected chambers with lengths L_1 and $L_2 = L - L_1$. The barriers were made of 20 mm thick Styrofoam to ensure minimal conductive heat transfer through the barrier. Rubber sealing on the three sides of each barrier in contact with the tank ensured that all mass exchange between chambers occurred above the barrier.

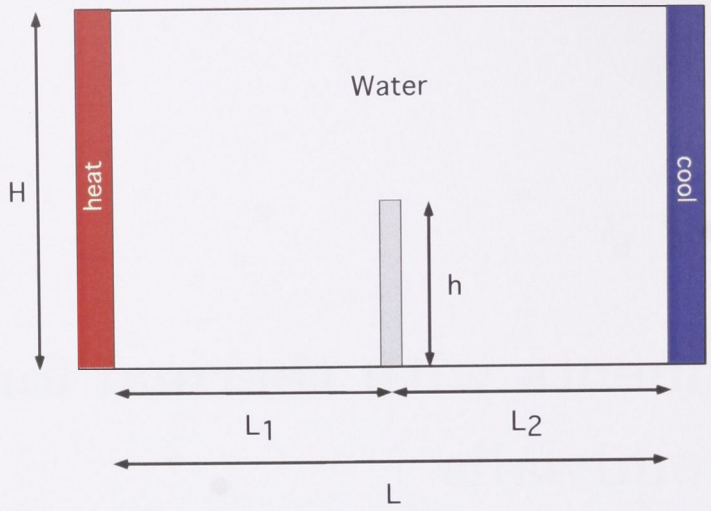

Figure 3.1: Experimental configuration (elevation view).

Heat loss from the tank was minimized by double glazed Perspex sidewalls. In addition, the tank was insulated on all sides with 50 mm thick polystyrene foam. The insulation on the two sidewalls was removed only when photographs and temperature profiles were being collected. The heat loss from the tank was found to be minimal, about 1% of the total convective heat flux in the no barrier case.

Two thermistors were placed in the interior of the tank, one in the middle of each chamber. Temperatures were logged as a function of time on a PC and the convective flow was observed to reach thermal equilibrium after about a day. Thermistors were used to measure temperature profiles through the two equilibrated chambers and in the gap above the barrier. The vertical resolution of the profiles was 10 mm except in the regions of large temperature gradients where the resolution was reduced to 2.5 mm. Visualisation of the flow was achieved using potassium permanganate crystals and food dye introduced into the flow through the holes in the tank lid. A slide projector was placed a few metres behind the tank illuminating a sheet of tracing paper attached to the back of the tank. The tracing paper acted as a light diffusing screen, against which the dye and crystals could be easily seen. A Nikon D100 digital camera was used to take photos during the experiments. Horizontal velocity measurements were made in the centre of the tank, above the barrier, in order to determine the mass and heat fluxes in the flow. These measurements were taken by dropping potassium permanganate crystals through the flow, generating approximately vertical dyelines. Photographs were taken at intervals between two and sixty seconds, and the velocities calculated (with an accuracy of $\pm 5\%$) using the horizontal displacement in dye line positions from one photograph to the next.

3.1.2 Temperature measurement

Each thermistor has a resistance (Ω) that is temperature dependent, and calibration of the dependency creates an accurate temperature measuring device. The resistance of a thermistor is measured by a bridge circuit that outputs a voltage through a data-acquisition card to the computer running a Labview program. For each thermistor, calibration of the voltage-resistance and resistance-temperature dependence was required. The bridges were calibrated by connecting a known resistance and measuring the output voltage on a data-acquisition card. The relationship between voltage and resistance is given by:

$$\frac{1}{R} = d + eV + fV^2, \tag{3.1}$$

where V is the voltage and d, e and f are constants. The constants are found by plotting $\frac{1}{R}$ vs. V and fitting a quadratic to the data points; the quadratic term is very small. An example of a bridge calibration plot is shown in figure 3.2*b*. The thermistors were calibrated by placing them in a temperature controlled water bath and measuring their resistance at a number of specified temperatures over the expected operational range. The relationship between temperature and resistance is given by:

$$\frac{1}{T} = a + b \ln R + c(\ln R)^3, \tag{3.2}$$

where T is the temperature in Kelvin, R is the resistance in ohms and a, b and c are constants. The constants are found by plotting $\frac{1}{T}$ vs. ln R and fitting the data points with a cubic equation without the quadratic term. An example of a temperature calibration plot is shown in figure 3.2*a*.

The calibrations of the bridges and thermistors remain stable. We occasionally test the calibrations, to ensure there has been no drift. The thermistors in the interior of the tank were Fasttip Thermoprobes series FP07 with a response time of 142 Hz in water and the thermistors in the copper plate were Thermoprobe series P60 with a response time of 3.3 Hz. While the precision of a thermistor is up to 0.002°C, the absolute accuracy of the thermistors used in our experiments was ± 0.1°C. There is also an error of ± 0.5 mm in the vertical positioning of the thermistors for monitoring the transition to steady state.

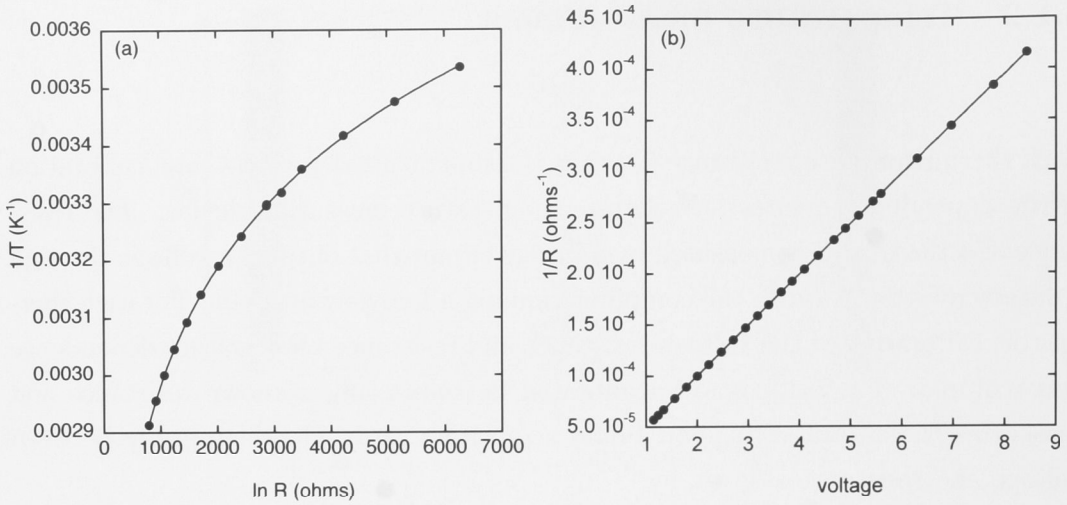

Figure 3.2: Examples of calibration plots for (a) thermistor resistance with temperature and (b) bridge resistance with voltage. • are the data points and the line is the fit to equation 3.2 in (a) and the fit to equation 3.1 in (b).

3.1.3 Dimensionless numbers

If we ignore the finite width of the tank (i.e. assume the convective flow is two-dimensional) as well as the non-zero thickness of the barrier, the experimental system is characterized by five dimensionless numbers: the Rayleigh number

$$Ra = \frac{\alpha g \Delta T H^3}{\nu \kappa}, \tag{3.3}$$

the Prandtl number

$$Pr = \frac{\nu}{\kappa}, \tag{3.4}$$

the tank aspect ratio

$$A = \frac{H}{L}, \tag{3.5}$$

the barrier height ratio

$$R_H = \frac{h}{H}, \tag{3.6}$$

and the chamber length ratio

$$R_L = \frac{L_1}{L}, \tag{3.7}$$

where α, ν and κ are the thermal expansion coefficient, kinematic viscosity and thermal diffusivity of the fluid and g is the gravitational acceleration.

In this work, R_H was varied by changing the barrier height h, and R_L was varied

Table 3.1: Dimensionless Numbers for the Experiments

Experiment	R_H	R_L
1	0	0.5
2	0.18	0.5
3	0.29	0.5
4	0.39	0.5
5	0.49	0.5
6	0.59	0.5
7	0.69	0.5
8	0.80	0.5
9	0.90	0.5
10	0.59	0.25
11	0.59	0.75
12	0.59	0
13	0.59	1.0

by changing the lateral position of the barrier (see table 3.1). The other parameters were fixed: $Ra = 5 \times 10^9$, $Pr = 7$, and $A = 0.65$. This Rayleigh number was as large as could practicably be achieved given the box dimensions. The Grashof number $Gr = Ra/Pr = 0.7 \times 10^9$ was below the value (about 10^9) at which turbulence sets in on a vertical plate Turner (1979), so laminar flow was expected in all of our experiments.

3.2 Experimental Results

Before examining the results of this study it is important to understand the basic circulation arising in a simple rectangular cavity heated at one endwall and cooled at the other endwall (see figure 2.1). We refer to this case as the 'no barrier case'. At high Rayleigh numbers (about 10^9 in the laminar regime), a strong boundary layer circulation accommodates most of the mass and heat fluxes: a buoyant (hot) plume rises up the hot endwall, flows along the top of the box, falls down the cold endwall as a dense (cold) plume, and then returns along the bottom of the box in a cold horizontal boundary layer (Cormack *et al.* (1974*b*), Imberger (1974) and Bejan & Tien (1978)). Fluid in the box interior or core is nearly stagnant and has a temperature field that varies linearly with depth and is independent of longitudinal position (Bejan *et al.* (1981) and Simpkins & Chen (1986)).

3.2.1 Dependence on Barrier Height

To examine the effect of R_H, we conducted 9 experiments in which the barrier height was varied, for connected chambers of equal lengths ($R_L = 0.5$; see table 3.1). The qualitative flow behaviour was similar in all these experiments. When a barrier was inserted into the tank, water in the cold horizontal boundary layer in figure 2.1 was prevented from flowing all the way to the hot plume. Instead the outflow from the cold plume pooled and slowly filled the right chamber in figure 3.1. Eventually, the coldest water totally filled this chamber to the height of the barrier, creating a 'cold chamber' whose final steady-state temperature profile contrasted dramatically with the temperature profile in the adjacent 'hot chamber' (figure 3.3). The presence of a barrier had a significant effect on the temperature profile at the uppermost levels in the tank only when the gap above the barrier was small (see figure 3.3*c*).

Figures 3.4 and 3.5 show visualisations of the steady-state convective circulation for some of the experiments. A hot laminar plume (not visible) rose up the hot endwall and detrained to form a hot horizontal boundary layer at the top of the tank. Similarly, a cold laminar plume formed at the top of the cold endwall and flowed down the plate, but it split into two at around the height of the barrier. The coldest water from the inner part of the plume (against the endwall) continued to flow downwards, but the water in the outer part of the plume was not cold enough (i.e. dense enough) to penetrate into the cold chamber: it instead detrained and flowed horizontally towards the barrier. Along the way, the intruding flow combined with upwelling water from the cold chamber to produce a strongly stratified overflow at the barrier (see figure 3.7). This flow then plunged over the side of the barrier to form a downflowing plume. Near the base of the barrier the momentum of fluid in the plume caused it to overshoot and oscillate about its level of neutral buoyancy in the heated chamber (figures 3.4 and 3.5). As the overflow was strongly stratified, only the very coldest water immediately adjacent to the barrier reached the tank bottom, while the remainder entered the interior of the hot chamber at a range of different levels (figure 3.5). This fluid was then gradually drawn towards the lower half of the hot endwall, where it was entrained into the hot plume. In the cold chamber, the flow was primarily driven by the cold sidewall plume, which produced a slow upwelling return flow (cf. Worster & Leitch, 1985). The cold chamber was also affected by stratified withdrawal into the barrier overflow, and by a small amount of heat transfer through the barrier (less than 3% of the total heat transfer, calculated by comparing the heat transfer through the barrier, due to the temperature difference across the barrier and thermal conductivity of the Styrofoam, to the heat transfer, by convection, above the barrier) that produced a slow up-flow against the

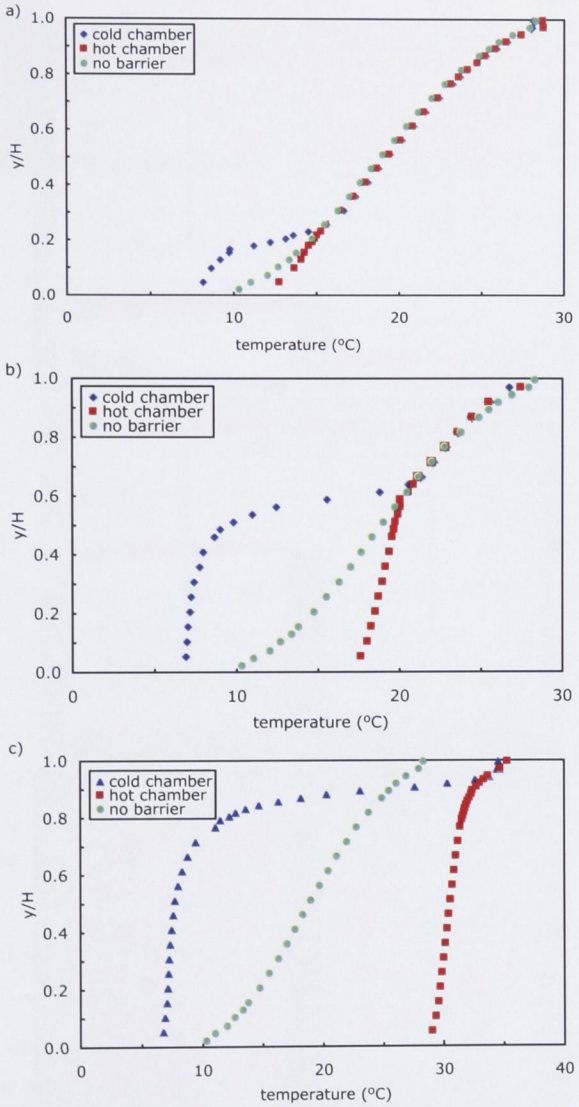

Figure 3.3: Steady-state temperature profiles through the two chambers as a function of barrier height: (a) experiment 2 ($R_H = 0.18$); (b) experiment 6 ($R_H = 0.59$); and (c) experiment 9 ($R_H = 0.9$). The profiles are compared with the steady-state temperature profile at the centre of the tank when no barrier is present (experiment 1).

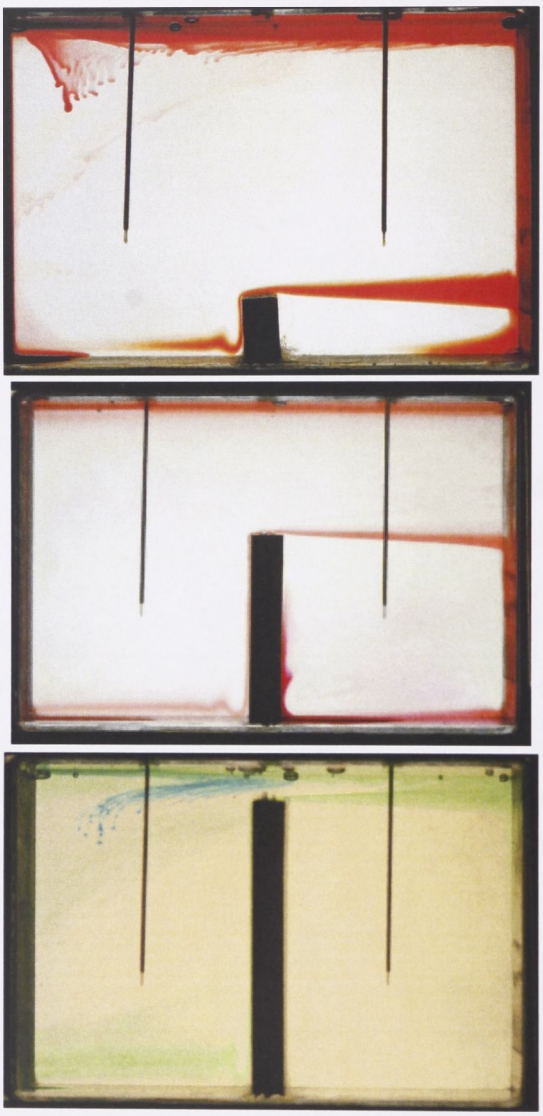

Figure 3.4: Visualisation of the boundary layer flow for experiments 2, 6 and 9. Red, blue and green dye was introduced into the boundary layer at the bottom of the hot chambers, and for experiment 6 red dye was also introduced into the boundary layer at the bottom of the cold chamber.

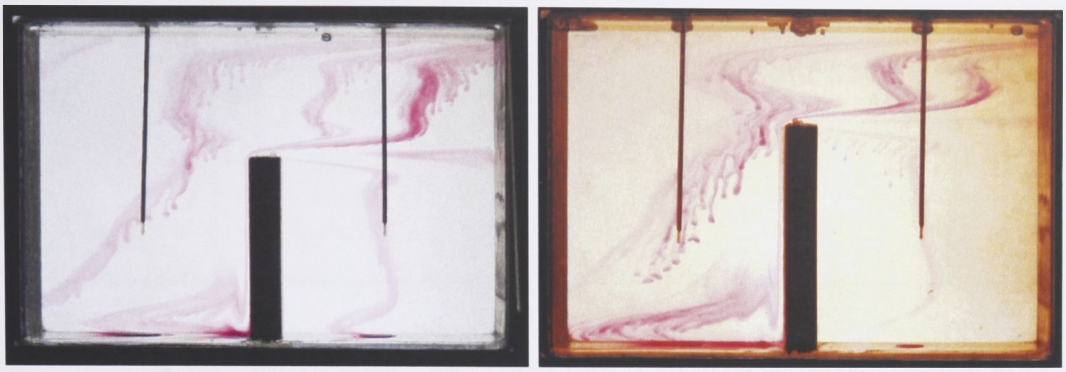

Figure 3.5: Visualisation of the interior flow for experiment 6 and 8. Initially vertical dye streaks were generated by dropping potassium permanganate crystals at three positions: the centre of the tank and aligned horizontally with the thermistors (visible in the centre of each chamber).

barrier (figure 3.4). Hence a balance between vertical conduction and advection is likely to be involved in maintaining the steady state vertical temperature gradient in the cold chamber.

The exchange flow above the barrier was found to be strongly dependent on the barrier height (see figure 3.6). In the no barrier case (figure 3.6*a*), we observed strong boundary layer flows at the top and bottom, with a weak uniform shear in the interior (cf. figure 2.1). With the addition of a small barrier (figure 3.6*b*), the top half of the flow was similar to the no barrier case (figure 3.6*a*), but the bottom half was significantly different: the return flow occurred in a thinner layer with a much faster velocity. This barrier overflow (like the hot boundary layer reaching the top boundary and the cold boundary layer reaching the base in the case of no barrier) also generated a number of horizontal 'shear layers', corresponding to local maxima or minima in the horizontal velocity profile. As h was increased, the region of uniform shear in the interior steadily decreased until it disappeared at $R_H = 0.59$ (figure 3.6*c*). When h was increased further, the number of shear layers decreased from six (for $R_H = 0.59$) to four (for $R_H = 0.69$, see figure 3.6*d*), and then to a simple bi-directional exchange flow for the highest barrier (figure 3.6*e*), where a layer of warm water flowed towards the cooled endwall above a cooler layer that overflowed the barrier.

In figure 3.7, the temperature profile above the barrier is shown for a number of different barrier heights. As the barrier height was increased, two main effects were observed. First, the temperature gradient in the barrier overflow systematically increased. Second, the temperature profiles were shifted to warmer temperatures. However, the temperature gradient above the barrier appeared to be unchanged (cf.

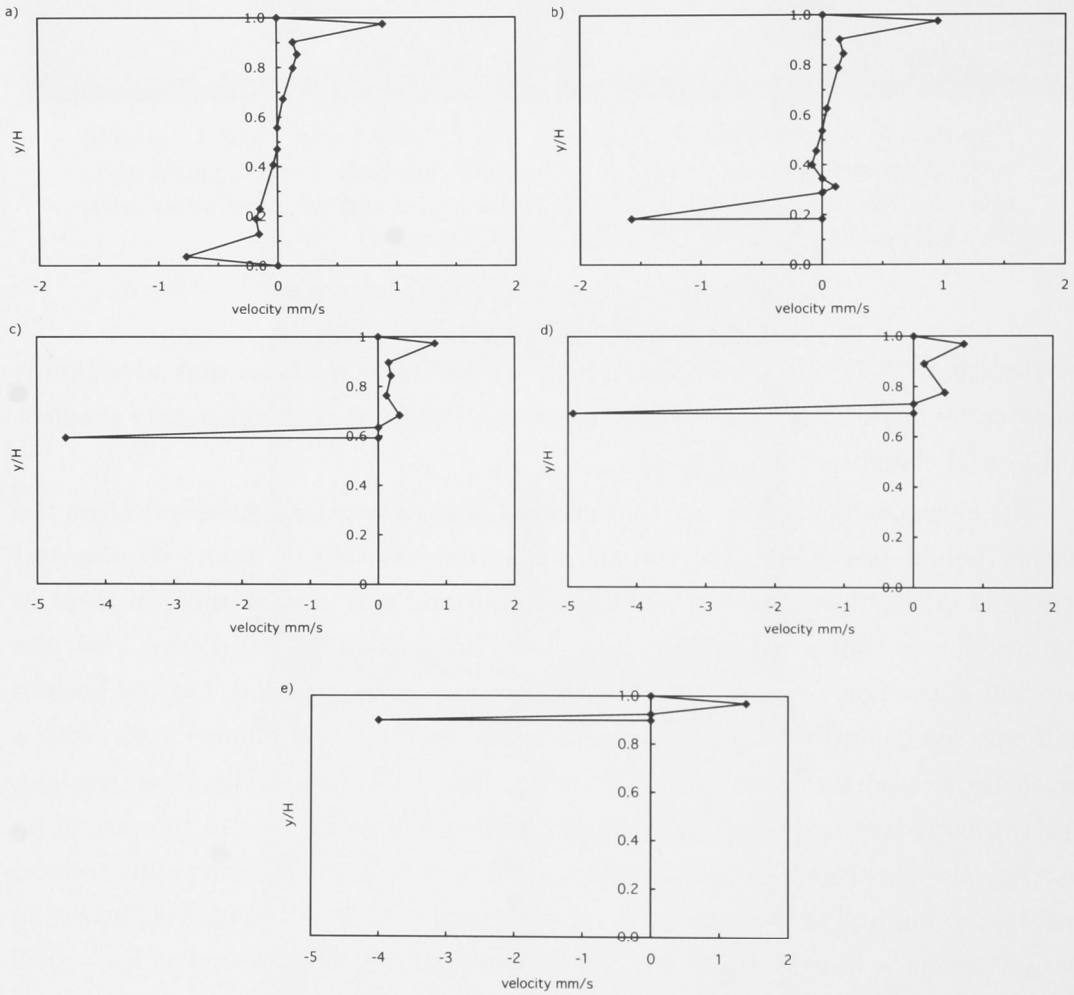

Figure 3.6: Velocity profiles above the barrier for a) $R_H = 0$, b) $R_H = 0.18$, c) $R_H = 0.59$, d) $R_H = 0.69$, e) $R_H = 0.90$. The points on the plots in (c) – (e) correspond to heights at which the velocity was either zero or a local maximum/minimum. Note that the horizontal scales in (a) – (e) are different.

figure 3.3).

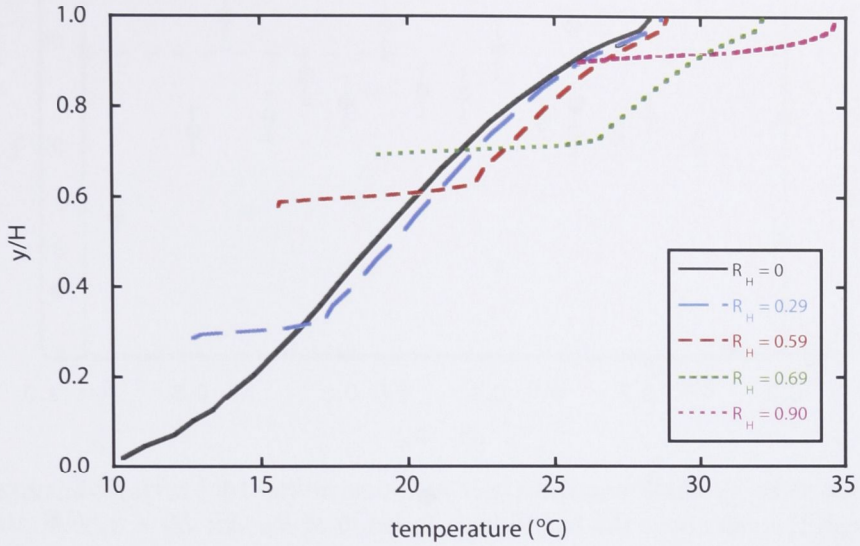

Figure 3.7: Temperature profiles above the barrier for $R_H = 0$, 0.29, 0.59, 0.69, 0.90, with the barrier located at the mid-point ($R_L = 1/2$).

From integration of the velocity profiles in figure 3.6 (between all heights with positive velocity) we determined the volume transport per unit width from the hot chamber to the cold chamber, as a function of the barrier height (figure 3.8). The magnitude of the volume transport is very similar, $1.75 \pm 0.25 \times 10^{-5}\mathrm{m}^2/\mathrm{s}$, for $0 \leq R_H < 0.8$, excepting the point at $R_H \sim 0.4$, where there is a suggestion of a maximum in flow rate. A substantial decrease in volume transport was only apparent when the barrier height became very large ($R_H > 0.8$), which satisfies the constraint that the volume transport must go to zero as $h \to H$ (and the gap closes).

From the measured velocity and temperature profiles, we determined the heat transport per unit width q across the barrier

$$q = \rho c_p \int_h^H uT \mathrm{d}y, \tag{3.8}$$

where ρ is the water density, y is the vertical coordinate and c_p is the specific heat of water at constant temperature. A Nusselt number can then be defined as

$$Nu = \frac{q}{k\Delta T} \tag{3.9}$$

where k is the thermal conductivity of water. The measured Nusselt number is

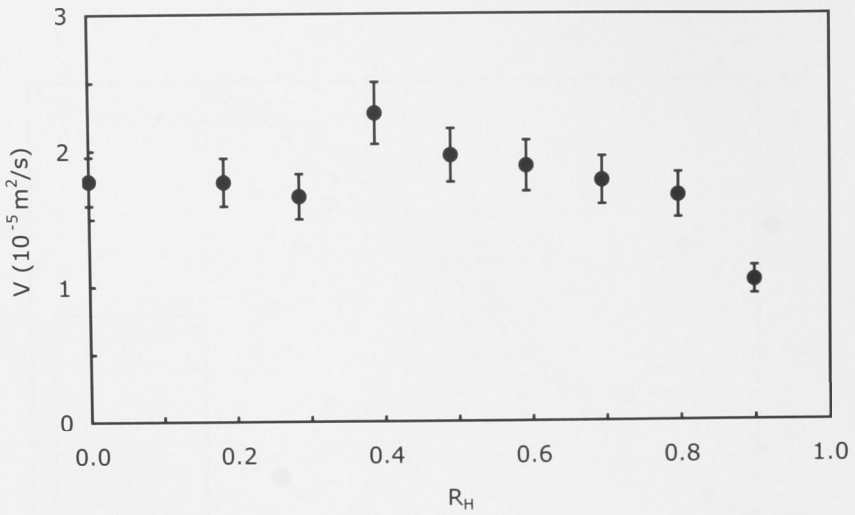

Figure 3.8: Volume transport per unit width (in $10^{-5}\,\mathrm{m}^2/\mathrm{s}$) exchanged through the gap above the barrier as a function of R_H, for $R_L = 1/2$.

plotted in figure 3.9 as a function of barrier height ratio R_H. For $0 < R_H < 0.4$, Nu is 29 ± 5; for $0.4 < R_H < 0.8$, Nu decreases slightly; and for $R_H > 0.8$, the heat flux was substantially smaller (satisfying the constraint that the heat transport must go to zero as $h \to H$).

A simple model for heat transport

In our experiments, the major impact of the barrier was the creation of the 'cold chamber'. The small temperature difference between the fluid in this cold chamber and the cold endwall implies that most of the heat transfer from this endwall must occur above the height of the barrier. It is therefore interesting to compare our results with a simple model where we assume that the heat transfer is effectively controlled by the gap height $h_g = H - h$. In a hypothetical rectangular cavity with the same height h_g, length L, and aspect ratio h_g/L (assumed small), the heat transfer (in the boundary layer regime) would be independent of aspect ratio and given by $Nu(h_g) \propto (\alpha g \Delta T h_g^3/\nu\kappa)^{\frac{1}{5}}$ (Bejan, 1980; Bejan & Tien, 1978). In figure 3.10, our heat transfer results are therefore re-calculated in the normalised form $Nu(h_g)/Nu(H)$ (where $Nu(H)$ is the Nusselt number for the box with no barrier) and plotted as a function of h_g/H. They are also compared with the simple model prediction $Nu(h_g)/Nu(H) = (h_g/H)^{3/5}$. We find that the model gives a good qualitative guide and understanding of the effect of the barrier. However, the model somewhat underestimates the observed dependence on gap height, which is

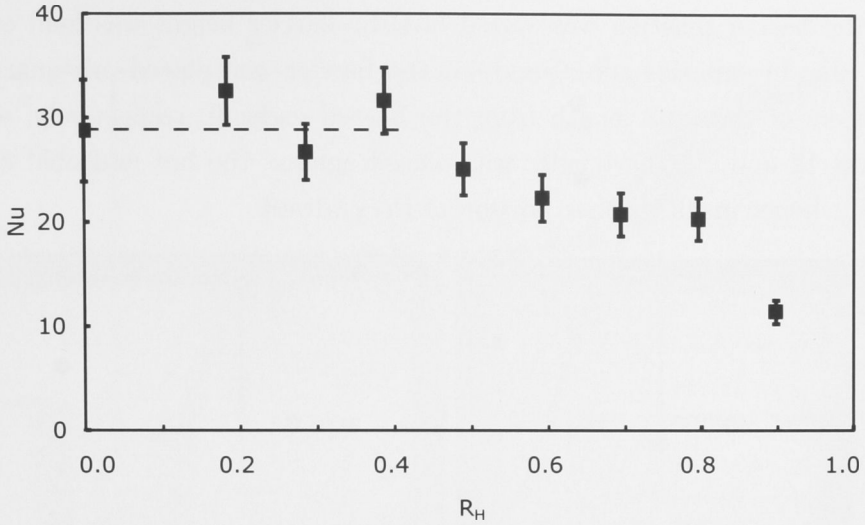

Figure 3.9: Nusselt number as a function of R_H, with the barrier at the centre ($R_L = 1/2$). The value of the dashed line is 29.

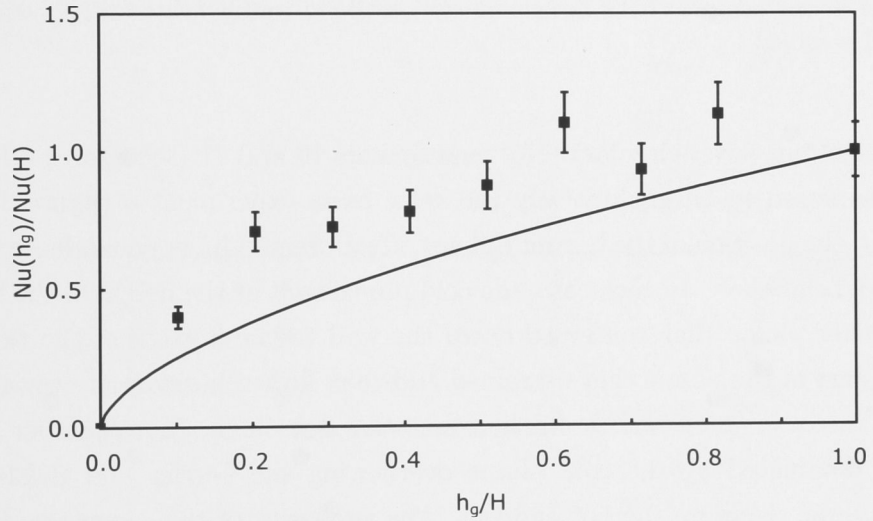

Figure 3.10: $Nu(h_g)/Nu(H)$ as a function of $h_g/H = 1 - R_H$ for $R_L = 0.5$. The curve is $(h_g/H)^{3/5}$.

not surprising as it takes no account of additional heat transfer through the endwalls below the barrier height.

3.2.2 Effect of Barrier Position

To investigate the effect of the barrier location, described by the ratio R_L, the results of experiment 6 were examined along with four further experiments (see table 3.1)

in which the barrier position was varied but the barrier height was held constant ($R_H = 0.59$). In experiments 10 and 11, the barrier was placed one-quarter and three-quarters of the tank length from the heated endwall, respectively, while in experiments 12 and 13, the barrier was placed against the hot and cold endwall, respectively, hence insulting that portion of the endwall.

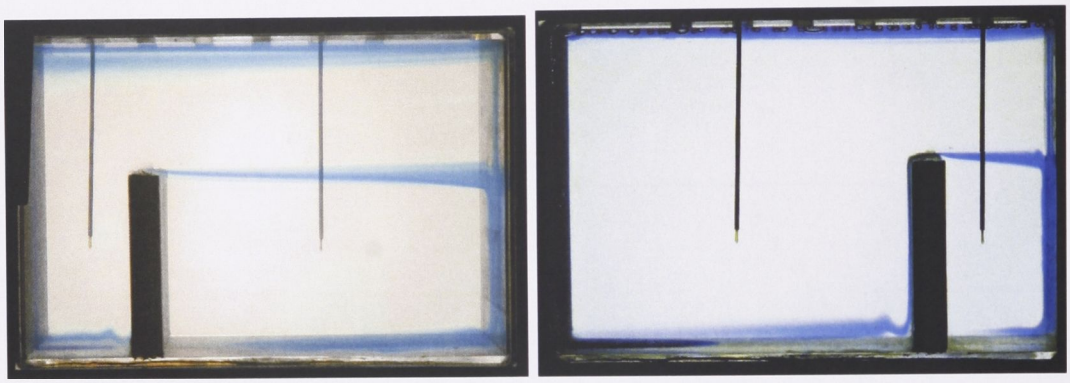

Figure 3.11: Visualisation of the boundary layer flow for experiment 10, a) and experiment 11, b). In each case blue dye was introduced into the boundary layer at the bottom of the hot chamber. Left hand wall is heated, right hand wall is cooled.

The boundary layer circulation for experiments 10 and 11 (see figures 3.11*a* and 3.11*b*) was found to be qualitatively the same as in experiment 6 (figure 3.4). In particular, the position of the barrier did not affect the ponding of cold dense fluid to form a 'cold chamber'. In each case, the cold plume split at the height of the barrier, into an inner plume that continued down the wall to the bottom of the tank and an outer part of the plume that detrained and then flowed horizontally towards the barrier. There was little change in the convective flow in the 'hot chamber', which was still dominated by the cold plume overflowing the barrier and the buoyant laminar plume rising up the hot endwall. The similarity of the convective flows in experiments 6, 10 and 11 is seen in both temperature profiles in the 2 chambers (figure 3.12) and velocity profiles above the barrier (figure 3.13).

In experiment 13, placing the barrier against the cold endwall eliminated the 'cold chamber'. The 'hot chamber' remained, and compared with experiment 6 there was little change in either the temperature profile (figure 3.12) or the velocity profile (compare experiment 6's velocity profile: figure 3.6*a* with experiment 13's: figure 3.14*b*). The elimination of the 'cold chamber' in experiment 13 has minimal effect on the dynamics of the 'hot chamber' because the cold dense fluid ponds below the height of the barrier, limiting the interaction of the convective flow with the cold endwall, wherever the barrier is positioned.

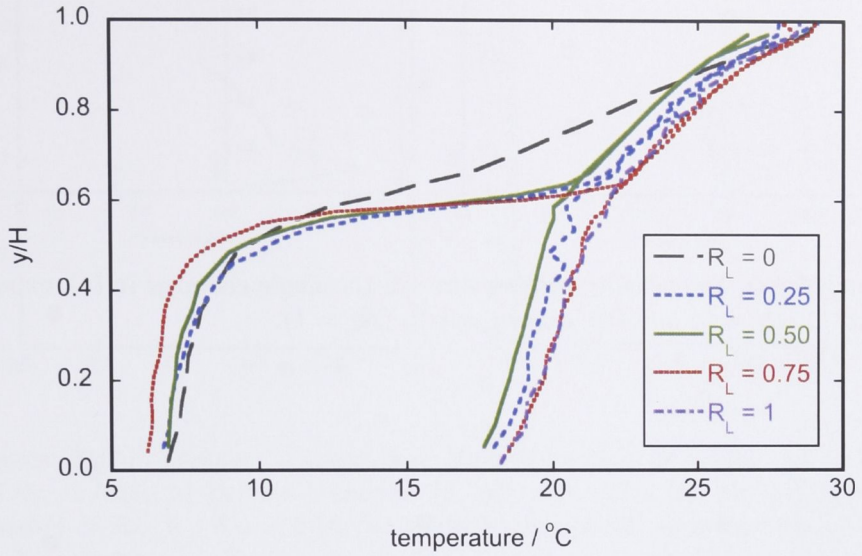

Figure 3.12: Steady-state temperature profiles with height, through the two chambers for barrier height $R_H = 0.59$ and different barrier locations (experiments 6, 10 and 11), and through the single chamber (experiments 12 and 13).

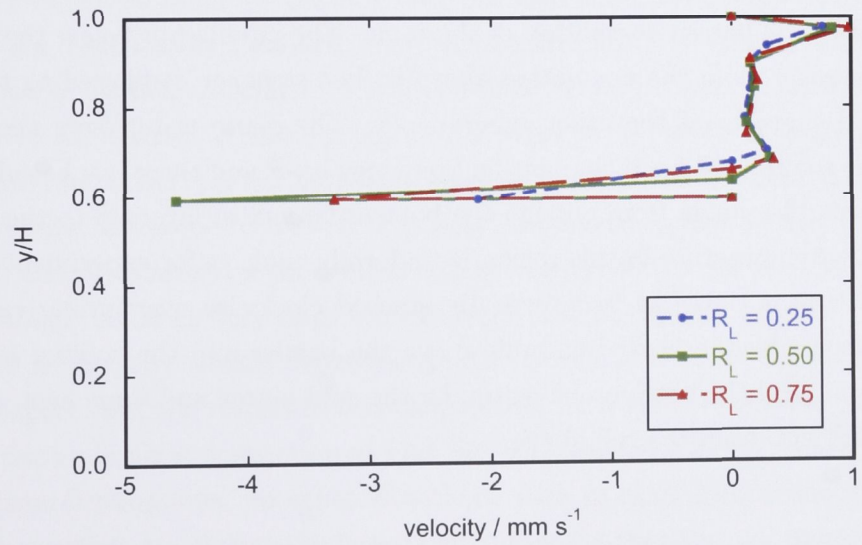

Figure 3.13: The velocity profiles above the barrier for different values of R_L (experiments 6, 10 and 11).

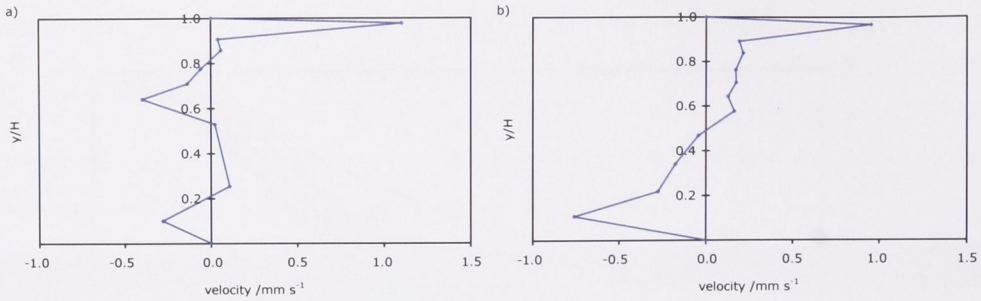

Figure 3.14: The velocity profiles through the single chamber in (a), experiment 12 ($R_L = 0$) and (b), experiment 13 ($R_L = 1$).

In experiment 12, placing the barrier against the hot endwall eliminates the 'hot chamber' and therefore limits the interaction of the convective flow with the hot endwall. Even so, the velocity in the top boundary layer is of comparable magnitude and thickness to experiment 6 (compare figure 3.14*a* with figure 3.13), but there is no option for a barrier overflow and so the strong temperature gradients seen in the cold chamber at the height of the barrier for experiment 6 do not develop (figure 3.12). Instead the temperature increases in an approximately linear fashion from the height of the barrier to the top of the tank. The circulation below the barrier height is weaker than the circulation above it, but stronger compared to the flow in the cold chamber of the other experiments. The dense water from the colder part of the cold plume feeds the bottom boundary layer and there is a broad return flow towards the plume from outside the bottom boundary layer up to the barrier height. The temperature in this region is uniformly cold, as for experiment 6. The overall picture is thus like two vertically stacked clockwise overturning cells, the top one driven by the heated endwall above the barrier and the cooling from the cold endwall, and the bottom one driven by the cold plume and some heat gain via vertical diffusion from the cell above.

From the measured velocity and temperature profiles, we also determined both the volume and heat transport per unit width from the hot chamber to the cold chamber, as a function of the barrier position. We found that moving the barrier towards the cold endwall results in a systematic increase in the volume transport (figure 3.15*a*), but has little effect on the heat transport (figure 3.15*b*).

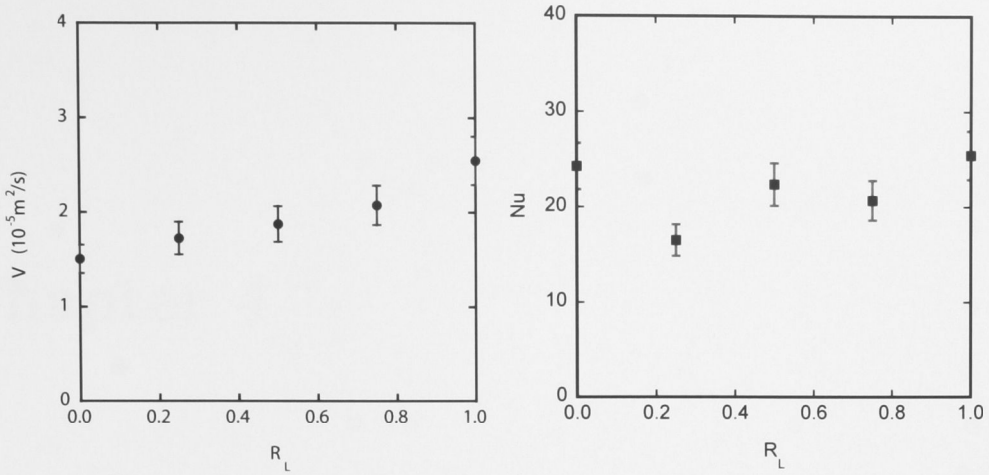

Figure 3.15: Volume transport and Nusselt number as a function of R_L, for $R_H = 0.59$. a) Volume transport (•) per unit width (in $10^{-5}\,\mathrm{m}^2/\mathrm{s}$) as a function of R_L, for $R_H = 0.59$. b) Nusselt number (■) as a function of R_L, for $R_H = 0.59$.

3.3 Conclusion

We have studied the convective flow in two connected chambers by placing a partial-height barrier across the base of a box with differentially heated endwalls. The introduction of the barrier severely disrupts the transport of heat and mass in the boundary layers adjacent to the box endwalls and base. Temperature profiles in the box are dramatically modified, with the formation of a very cold chamber and a moderately warmer chamber. A complex flow structure arises, featuring a fast overflow of the barrier, a varying number of shear layers in the density stratified flow above the barrier, partial boundary layer detrainment on the cold endwall, and slow upwelling in the cold chamber. The heat (and mass) transport is little changed by small and medium-sized barriers, and only begins to decrease rapidly when the barrier height becomes very large (in excess of 80% of the box height). The heat transport is also only weakly dependent on the lateral position of the barrier.

We expect that the results in this chapter will be useful in predicting the effect of a barrier on laminar convection at high Rayleigh numbers in some industrial and environmental situations. In other situations, such as most geophysical flows, the Rayleigh numbers are likely to be large enough that the overflow and boundary layer flows will all be turbulent, which might lead to very different behaviour. In chapter 7 we study the case of turbulent overflows, and will use the results here to guide the research and help understand the effect of barrier height in a turbulent case.

Chapter 4

Horizontal convection and Sandström's experiments revisited

We now turn to convection that is again forced by a horizontal temperature difference, but in this case the forcing is applied at a specific height. Sandström (1908, 1916) reported a set of laboratory experiments with heated and cooled pipes designed to heat or cool at only one level, at opposite ends of a long, narrow tank of water. The heating and cooling levels could be adjusted so as to place the heating source above, below, and at the same level as, the heat sink. These experiments were motivated first by the oceanographic question of whether the poleward transport of heat in the oceans is forced by the meridional gradient of heating of the ocean surface (Sandström, 1908) and, second, by the meteorological phenomenon of stable stratification formed over a coastal plain by circulation between cold mountain slopes and the warmer sea surface (Sandström, 1916). The experiments potentially provide fundamental insights into the nature of convection. The results and their geophysical implications have been under debate for close to a century – a debate recently rekindled by heightened interest in the dynamics of the global meridional overturning (or thermohaline) circulation of the oceans (Huang, 1999; Hughes & Griffiths, 2006; Kuhlbrodt *et al.*, 2007; Nycander *et al.*, 2007; Paparella & Young, 2002; Wang & Huang, 2005; Wunsch, 2000; Wunsch & Ferrari, 2004). The present work is prompted by the unexplained observations of Sandström, an inconsistency with modern experimental observations, and widely-held misconceptions about the conclusions.

4.1 The origins of Sandström's postulate

In Sandström's pioneering experiments the flow depended on the relative vertical position of the heat source and sink. In his first report of such experiments (Sandström, 1908) the heat source was placed 8 cm above or below the level of the cooling source, the sources being at opposite ends of the tank. When the heat source was placed at a lower level than the cooling source, convection persisted and the long-term flow was reported to be confined to depths between the two sources (figure 4.1*a*). When the heat source was placed at a higher level than the cooling source, a density stratification developed between the levels of the sources during an initial transient period of flow, after which circulation was reported to have vanished (figure 4.1*b*). Sandström (1908) postulated that a sustained circulation can occur only if the level of the heat source is below that of the cooling source. In a later report (Sandström, 1916) similar experiments were repeated in different apparatus, this time also including the case of heating and cooling sources at the same level. The circulation was again reported to vanish in the cases with the heat source above the cooling source or with the sources at the same level.

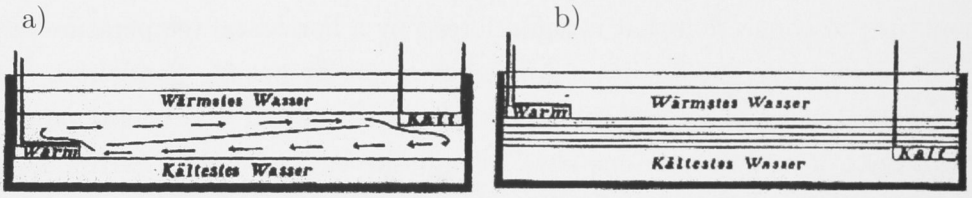

Figure 4.1: Sandström's two experiments reported in 1908.

Sandström's conclusions have become known as Sandström's 'theorem' (Bjerknes, 1916; Defant, 1961; Jeffreys, 1925; Sandström, 1922) although the term 'postulate' is more appropriate. Sandström (1908) originally stated his conclusion as (our translation from the German): "... there must be heating as well as cooling if a [sustained] thermal circulation is to develop in the ocean" and "From these two experiments we derive the conclusion that a [sustained] thermal circulation can occur only if the heat source is below the cold source". Defant (1961) stated the 'theorem' similarly as: "a closed steady circulation can only be maintained in the ocean if the heat source is situated at a lower level than the cold source" and argued (incorrectly; Jeffreys, 1925) that the 'theorem' is supported by the thermodynamics of a Carnot cycle (in which work is available to overcome friction only if the heating is at a higher pressure than, hence below, the cooling; Bjerknes, 1916; Huang, 1999). The Sandström conclusion has been used in recent years to help substanti-

ate the view that buoyancy fluxes at the ocean surface cannot drive a significant circulation in the oceans (Wunsch, 2000). However, Jeffreys (1925) showed on theoretical grounds that the conclusion is incorrect because the heating and cooling will create a horizontal density difference, hence a flow. He also reconciled a sustained flow driven by a heat source above, or at the same level as, a cooling source with thermodynamic principles by pointing out that diffusion of heat allows the heating and cooling of the fluid to take place at levels different from the sources. Others have interpreted this conclusion as implying a 'slow, diffusively-driven' circulation (Huang, 1999) although the magnitude of such a circulation was not predicted. The magnitude has since been predicted and measured in the particular case of heating and cooling along a horizontal boundary (see below). On the other hand it is well known that diffusion can drive vigorous convection, as in the case of heating from below and cooling from above or from heated or cooled sidewalls (Chapter 3; Coman *et al.*, 2006*b*). We also note that diffusion is essential, even at very large Rayleigh (Ra) and Péclet (Pe) numbers, if heat is to enter or leave the fluid from boundaries or other heat sources (except where penetration of radiative heating into the fluid, internal heating or mass injection play a role, in which case heating is again distributed away from the source). In the context of the complex process of heat transport across the atmosphere-ocean interface, the transport will involve turbulent mixing. Turbulence is also thought to be important to diffusion through the depth of the oceanic thermal boundary layer.

There are no clues in Sandström's text that tell us whether he was aware of the role of the conduction of heat. However, he formulated his conclusions from experiments with water, in which conduction was clearly present and essential for any heat transfer to or from the pipes. In comments overlooked by later proponents of "Sandström's theorem," Sandström (1908) also reasoned that his postulate would not apply to the oceans, where circulation would be made possible by the presence of vertical mixing processes[1], thus foreshadowing the point of Jeffreys (1925) (with vertical transport of heat owing to mixing rather than to conduction). He anticipated that circulation would extend to the maximum depth of vertical mixing, arguing that any circulation resulting from surface heating in the tropics and surface cooling at high latitudes would correspond to the case of heating below cooling because the heating of water, as it upwells from the ocean depths, occurs throughout the

[1]It is interesting that Sandström's discussion of the mixing recognised the capacity for mixing to be increased by loss of heat but retention of salt in sinking motions at the tropics, the process we now recognise as double-diffusive salt-fingering. The first salt finger experiment was by W. S Jevons in 1857, to model cirrus cloud formation (Schmitt, 1995). However, the phenomenon was not recognised in oceanography until 1956 (Stommel *et al.*, 1956).

temperature gradient region. Sandström envisaged convective circulation limited to the upper 1000 m (the thermocline). If viewed in the context of later ideas on abyssal circulation (Munk, 1966) involving downward mixing of heat throughout most of the ocean depth, Sandström's discussion might lead us to conclude that a buoyancy-forced circulation could even extend all the way to the bottom of the ocean. His reasoning was correct but is inconsistent with his report of no sustained flow in his experiments (where diffusion is crucial to heat transfer) and with the apparent neglect of diffusion in arriving at his primary conclusion.

Modern experiments (Mullarney *et al.*, 2004; Rossby, 1965; Wang & Huang, 2005) have demonstrated that a substantial convective circulation is initiated and indefinitely maintained in a box when different temperatures or heat fluxes are applied along a horizontal (geopotential) boundary. In these experiments the source area available for conductive heat transfer to or from the water is comparable to the dimensions of the box. Rossby (1965) and Wang & Huang (2005) applied a linear temperature gradient along the base, and Mullarney *et al.* (2004) used piece-wise-uniform boundary conditions applied over the base (either two imposed temperatures or an imposed heating flux applied to one half of the base and a cooling temperature applied to the other half of the base). All of these experiments were carried out under much more controlled thermal conditions than Sandström's. In particular, the side wall heat transfer coefficient in each case was much smaller. Rossby (1965) and Mullarney *et al.* (2004) also used much wider boxes so that the expected side wall heat gain or loss per unit volume of fluid was further reduced by an order of magnitude. Rossby observed a laminar circulation through the full depth and length of the box, including a narrow laminar plume against one end wall. The experiments of Mullarney *et al.* (2004), in a longer box and with substantially larger values of the Rayleigh number, revealed unstable flow involving a secondary convective instability in the horizontal thermal boundary layer (for $Ra_F \gtrsim \mathrm{O}(10^7)$), shear instabilities that caused mixing and entrainment into the end wall plume, and eddying in the horizontal plume outflow. Both of these studies showed a long-term equilibrium circulation through the full depth of the box. The experiments of Wang & Huang (2005) were carried out in a narrow slot-shaped box surrounded by a vacuum for the purposes of insulation. Again a sustained and unsteady circulation was observed, though it was of only partial depth. The modern laboratory results are supported by two-dimensional numerical solutions (Beardsley & Festa, 1972; Mullarney *et al.*, 2004; Paparella & Young, 2002; Rossby, 1998) and theoretical analyses (Hughes & Griffiths, 2006; Hughes *et al.*, 2007; Killworth & Manins, 1980), which are also at odds with Sandström's conclusion.

The discrepancy between the modern experiments and numerical solutions, on the one hand, and Sandström's observations on the other, has not been explained. In view of continued appeal to the Sandström studies to discount a significant role for convective forcing in the ocean overturning circulation, we resolve the disagreement by repeating Sandström's experiments under conditions similar to those used a century ago, and again with some improvements. Our observations are in direct contradiction to Sandström's report. We conclude that the original observations were incorrect and that there is no basis for Sandström's 'theorem'. The experiments also demonstrate some important principles.

4.2 The experiments

The original experiments of Sandström (1908) were carried out in a long but very narrow tank (1 m long × 25 mm wide × 250 mm high, figure 4.1) having walls of 6 mm thick glass and end walls and base of wood. The working fluid was a 2% NaCl solution and we can infer that the depth of the fluid was 200 mm. The tank had no insulation and there was little control on the room temperature. The heating and cooling sources were not described but were made from metal pipe (the exact design will have influenced the heat fluxes attained but is otherwise unimportant). The heating water passed through one pipe was at 40°C and the cooling water passed through the other pipe was at 0°C. Two experiments were reported: one with the heating source 80 mm below the cooling source, and one with the heating source 80 mm above the cooling source, the sources being at opposite ends of the box in each case. In later experiments (Sandström, 1916) a third case was included: the heating and cooling sources at the same (mid-depth) level. In these experiments the tank was of similar construction but 0.5 m long, 50 mm wide and 0.5 m high. The heating and cooling sources "were constructed according to the same principle as a modern domestic heater which consists of a metal cell system that carries flowing cold and hot water". The temperature difference between the heating and cooling water entering the pipes "from two large wooden drums of considerable capacity" was "small but constant". Room conditions were controlled by double glazed windows, thick walls of the building, and heating from "an oven that was burning night and day so the room temperature was very constant".

In reconstructing the essence of the original experiments we aimed to closely reproduce the original design, fully recognising that it is poorly suited to controlled experiments with thermal convection. We chose an existing acrylic box 0.75 m long and 70 mm wide, filled with water to a depth (H) of 200 mm, see figure 4.2. It should

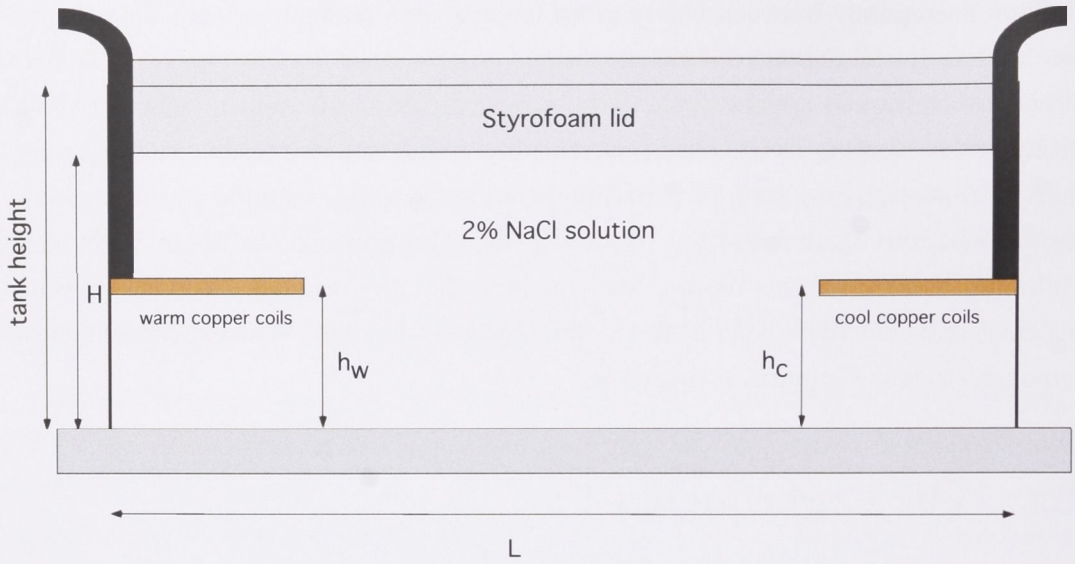

Figure 4.2: Side view of the experimental set-up for our Sandström style experiments.

be kept in mind that the use of both acrylic walls and the larger box width reduced the effect of sidewall heat transfer to the room compared with that in Sandström's narrower, glass-walled tanks. Although the water tank in the original experiments apparently had an open free surface, we used either a free water surface separated from the room air by a layer of 'cling wrap' plastic over the top of the box (to limit evaporation), or as an improvement, an insulating lid of 80 mm foam board fitted firmly within the tank walls and in contact with the water (in addition to the 'cling-wrap' seal). Our tank was in all runs placed on 30 mm of expanded polystyrene foam board and a wooden bench top. The air-conditioned laboratory temperature varied between 20°C and 22°C. We first carried out runs with neither sidewall nor surface insulation (the conditions closest to the original experiments). We also carried out runs with a close-fitting layer of 40 mm foam board against all sides of the tank and the 80 mm foam board on the water surface.

For the heating and cooling sources we used 6.35 mm o.d. copper pipe to construct two planar coils each comprising four 130 mm arms parallel to the sidewalls and equally spaced across the width of the tank (making a total pipe length of 593 mm in contact with the water in each source). The coils were placed horizontally at the desired depth and connected to insulated supply pipes through which water at 0°C or 40°C was rapidly re-circulated from temperature-controlled water baths (constant to within 0.02°C). These temperatures were those used by Sandström (1908) and are also symmetric about our room temperature.

The flow was visualized by dropping potassium permanganate crystals through holes in the lid and by slowly releasing streams of neutrally-buoyant solutions of food dye at strategic locations. The crystals gave rise to vertical dyelines, which were subsequently distorted by horizontal flow and allowed quantitative measurements of velocities. The food dye was carried around with the circulation and indicated the overall pattern of flow, along with any instability or mixing. A slide projector was placed 5m behind the tank, illuminating a piece of tracing paper attached to the back of the tank. This acted as a light diffusing screen against which the food dye and potassium permanganate could be clearly seen. A Nikon D100 digital still camera and a Sony digital video camera were used to capture images of the flow.

The important parameters for these experiments are: the tank aspect ratio,

$$A = \frac{H}{L}, \tag{4.1}$$

where H is the water depth and L is the tank length; the Prandtl number,

$$Pr = \frac{\nu}{\kappa}, \tag{4.2}$$

where ν is the kinematic viscosity and κ is the thermal diffusivity of water; the Rayleigh number,

$$Ra = \frac{g\alpha\Delta T H^3}{\nu\kappa}, \tag{4.3}$$

where ΔT is the difference in source temperature and g is the gravitational acceleration; and the relative height of the sources,

$$\eta = \frac{h_c - h_w}{H}, \tag{4.4}$$

where h_c and h_w are the heights of the cold and warm source, respectively. Values of $\eta > 0$ correspond to the cooling source above the heating source.

Table 4.1: Insulation conditions for each experiment

η	Insulation		
	None	Partial	Full
-0.4		√	
-0.2		√	
0	√	√	√
0.4		√	
1.0		√	

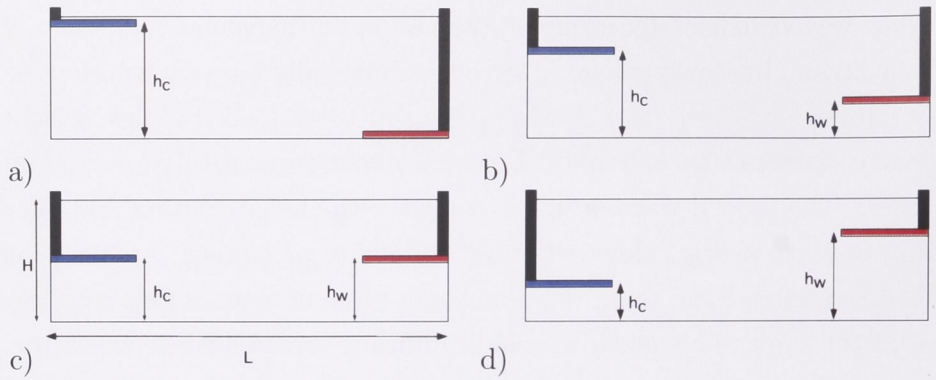

Figure 4.3: Sketches of the four arrangements of the heating and cooling sources used in our reproduction. The heating coil is at the right, and the cooling is at the left end. a) $\eta = 1$, b) $\eta = 0.4$, c) $\eta = 0$, d) $\eta = -0.4$. Case a) provides a reference for the normalisation of results. Cases b) and d) are similar to the experiments reported in Sandström (1908) and cases b) to d) were reported in Sandström (1916). We used two different relative heights in case d). The immersed supply pipe (shown as a black vertical band above each source) was insulated.

We examined five values of η, in which the heating and cooling sources were placed at different depths at opposite ends of the box. These cases are summarised by the four arrangements in figure 4.3. Thus only one parameter was varied, namely, the relative height of the sources η. In addition, the amount of thermal insulation surrounding the tank, which also imposed the top boundary condition, was varied, Table 4.1. The case (figure 4.3*a*) with the heat source at the bottom of the box and the cooling source at the top is an extreme arrangement of the sources and will give rise to the strongest circulation of any η, thus providing a useful end-member benchmark with which to compare the other experiments. This will give meaning to terms such as "strong" and "weak" circulation. We always placed the sources equal distances from the mid-depth, about which any flow is expected to be approximately symmetric (apart from effects of asymmetric top and bottom boundary conditions). Note that the case of heating and cooling sources at the same depth (figure 4.3*c*) is not identical to the case of differential heating distributed along a horizontal boundary as in Rossby (1965), Mullarney *et al.* (2004) and Wang & Huang (2005), where heat transfer to or from the boundary occurs over the whole length of the box. In the Sandström style of experiment, the sources have relatively small areas and will therefore provide a smaller heat flux, or weaker forcing.

For completeness sake we determined the average heat transfer coefficient for the tank boundaries by measuring the rate of change of heat content at known temperature differences while the water in the tank was cooling by natural convection.

With no sidewall insulation we obtained a heat transfer coefficient of 7.18 $Wm^{-2}K^{-1}$ and with insulation this coefficient reduced to 2.16 $Wm^{-2}K^{-1}$. However these coefficients are not of direct use because the heat input and output from the coils could not be determined without carrying out a much more substantial project to correlate velocity and temperature perturbations over the flow field in the vicinity of each coil. This was thought to be of little value given the existing more detailed experimental and numerical studies with boundary heating and cooling and much smaller (laboratory) or zero (numerical) sidewall transfer (Mullarney *et al.*, 2004). Further experiments of this nature will also be reported in sections 5 and 6.

Experiments were set up with the water initially close to room temperature, and the heating and cooling sources were activated (by turning on the pumps providing water from the temperature baths). Transient flows were observed, equilibrium was approached after 2 - 3 days, and measurements of the final flow were not made until after at least 3 days. Experiments were run for at least one week, and in some cases for two weeks.

4.3 The circulation

The initial transient flows were similar to those reported by Sandström (1908, 1916). The heating and cooling source generated plumes that ascended to the top or fell to the bottom of the box, respectively. These plumes were not turbulent under the conditions used, and there was little mixing and entrainment, but they were unstable and unsteady. The plumes filled the top and bottom regions of the box with pools of almost (but not quite) uniform density. In the reference experiment (figure 4.3*a*), both plumes travelled through the full depth of the box. In case (b) (figure 4.3*b* and figure 4.4*a*) only the layer between the levels of the sources was directly affected by both plumes. Beyond this layer there was a top region directly affected by the warm plume only and a bottom region affected by the cold plume only. In cases (c) and (d), where either the two sources were at the same depth or the heater was above the cooler, there was no intermediate region in which both plumes maintained the flow but again the separate volumes above and below the sources were each filled by the warm and cold plume, respectively. With the sources at the same level a large vertical temperature gradient developed across an interface at the source level (figure 4.3*c* and figure 4.4*b*). With the heater above the cooler a large temperature gradient developed across a thick gradient region between the levels of the sources (figure 4.3*d* figure 4.4*c*).

While the transient flows are interesting (and would be even more so for turbulent

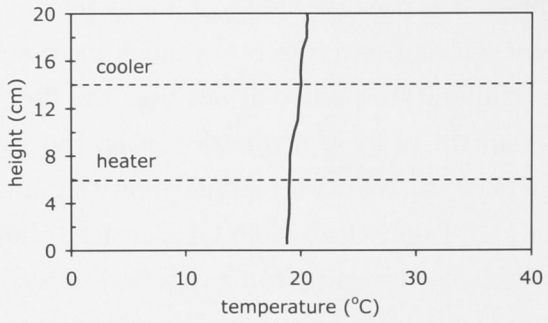

(a)

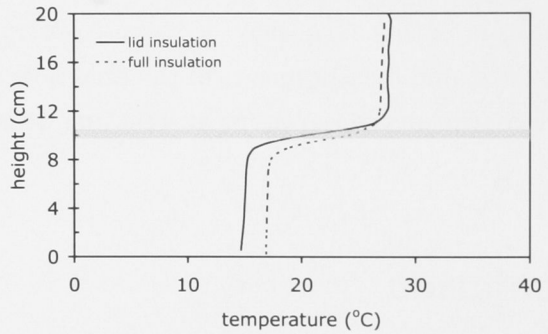

(b)

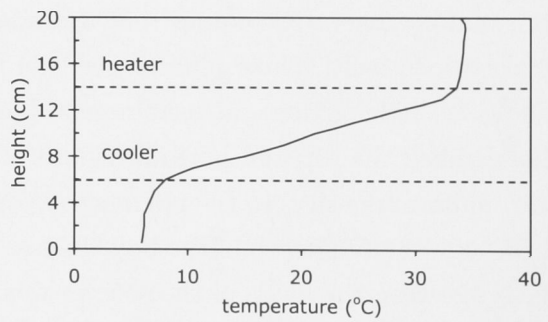

(c)

Figure 4.4: Plots of the vertical profiles of temperature measured in the long-time equilibrium flow in the cases shown in figure 4.3*b*, *c* and *d*, respectively. In a) and c) the dashed lines indicate the heights of the heating and cooling coils (approximately 80 mm apart), and in b), where the sources are at the same height, the thickness of the sources is indicated by the grey band. All three profiles (solid lines) are for the case with an insulating lid but no side wall insulation, and included in b) is a profile (dashed line) for the corresponding case with full lid and sidewall insulation.

plumes) it is the long-term equilibrium circulation that has provoked controversy, and is the focus of this chapter. We first describe the flow behaviour for the different source positions in a set of experiments using the same boundary conditions: a plastic 'cling-wrap' seal and a foam lid in contact with the surface, and no foam insulation on the side or end walls. Apart from the improved upper boundary conditions these are close to the poorly controlled experiments of Sandström. Figure 4.5 shows side views of the distortion of a vertical dye line in each of the cases in figure 4.3. When the heating coil was at the base and the cooling coil was at the surface (figure 4.3*a*), there was one overturning cell with well-defined plumes on the end walls and horizontal plume outflows against the base and lid. The horizontal flow at the top had a speed nearly 20% larger than that at the bottom, a difference consistent with the known increase of thermal expansion coefficient with increasing temperature. (As the equilibrium state was one in which there is no net heat input to the water, and the mean water temperature was close to room temperature, there was an approximately equal heat flux at each coil, and hence a greater buoyancy flux owing to a larger expansion coefficient in the warm plume compared with that in the cooled plume.) We chose to use a single speed - the average of the two maximum speeds for the flow in figure 4.3*a* - to normalise the velocities measured in all other cases. In this reference case there was a small stable temperature gradient throughout the depth of the box (similar to that in figure 4.4*a*), but the top-to-bottom temperature difference ($\sim$ 1°C) was only 2-3% of that applied between the sources.

When the heating coil was 80 mm below the cooling coil (figures 4.3*b* and 4.5*b*), there was again a single overturning cell in the equilibrium state, the plumes each falling or rising to the furthest boundary and forcing motion throughout the box. The velocity maxima (figure 4.5*b*) were at the level of the sources rather than close to the top and bottom of the tank. These maxima were broad and of approximately equal magnitude, with the velocity vanishing at the top and bottom (rigid, no-slip) boundaries and passing through zero at mid-depth. Thus the plume outflows were centred near the level of the opposite source, but with a thickness comparable to the distance of that source from the nearest horizontal boundary (60 mm). This flow structure is a new observation that may be of interest in many problems involving two buoyancy sources, notably building ventilation with a source of heat below a source of cooling, and where (turbulent) vertical diffusion may play a role. The flow was significantly different from that reported by Sandström (1908, 1916), who described the long-term motion as being confined strictly to depths between the two source positions. The temperature gradient in the recreated experiments varied little

through the depth (figure 4.4*a*) and the top-to-bottom difference was approximately 2°C, or 5% of the applied temperature difference. The top and bottom regions were not of uniform temperature nor were they distinct from the region between the source levels.

The case with heating and cooling sources at the same depth (figures 4.3*c*) is shown in figure 4.5*c*. There was again an obvious, sustained circulation. This consisted of an anticlockwise circulation cell (which included the cold plume) below the density interface and another anticlockwise cell (including the warm plume) above the interface. To the eye, the velocities were comparable to those in the reference case (heating coil at the bottom, cooling coil at the top). The change from a single cell (figures 4.3*a*, *b*) to two cells gave rise to a large temperature gradient near the source level (figures 4.4*b*), a large temperature difference (33% of the applied difference) between the weakly stratified upper and lower regions, and a strong vertical shear across the density interface. Of the four velocity maxima in figure 4.5*c*, the two in the upper cell were slightly larger than the corresponding maxima in the lower cell, and the two maxima nearest the density interface were only 30-50% of those near the top and bottom of the box. It will be seen below that the velocities in this case are comparable even to those in the case of heating at the base and cooling at the top. Video footage of the advection of passive tracer released near each source more effectively revealed the unsteadiness and eddying motion in the plumes, the pattern of the box-scale circulation and the rate at which water was carried around the overturning cells. The flow is a consequence of a horizontal temperature difference at the level of the sources. This flow is in sharp contrast to the original reports of vanishing circulation (Sandström, 1908, 1916) and some subsequent interpretations (Defant, 1961).

Perhaps more remarkable is the flow in case (d) of figure 4.3 with the heating source well above the cooling source (either 40 mm or 80 mm). The temperature difference between the upper and lower regions in the case of a 80 mm source separation (figure 4.4*c*) was 29°C, substantially greater than for sources at the same level (and increasing with height difference between the sources). There were three anticlockwise cells - one above the heater, another below the cooler, and another (much weaker) cell between the levels of the sources (figure 4.5*e*). There was a horizontal velocity maximum at the level of each source, and the maximum velocities were again comparable to those in the previous cases. Speeds in the upper cell were 50-100% larger than those in the lower cell. This is possibly a result of the increase of expansion coefficient with temperature, and possibly because under these conditions the sidewall heat transfer is likely to have been the dominant source, or sink,

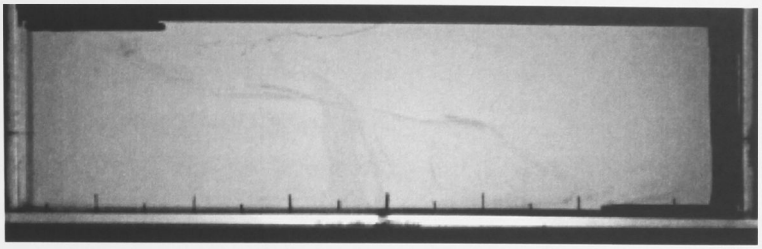

(a)

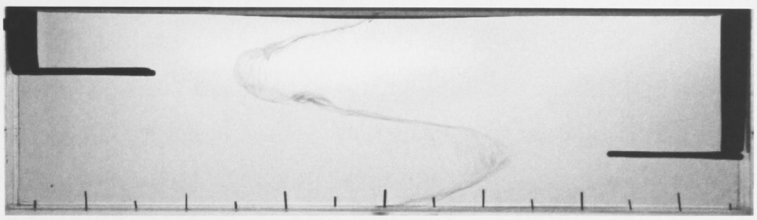

(b)

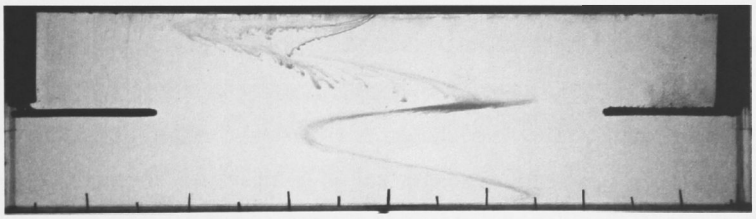

(c)

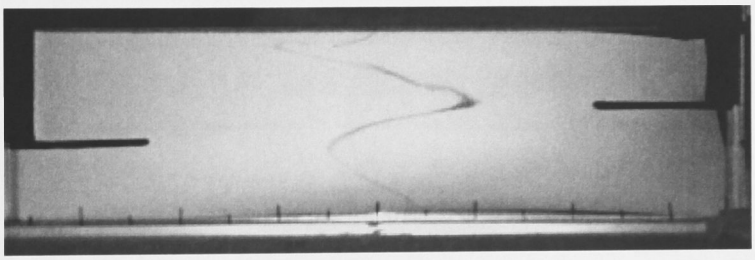

(d)

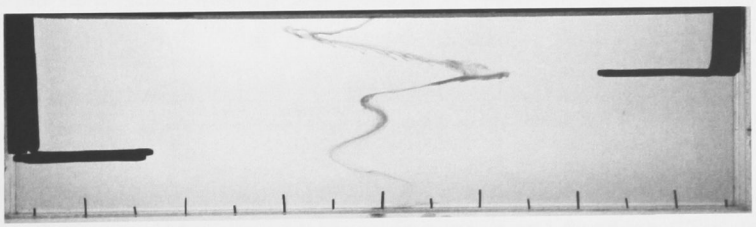

(e)

Figure 4.5: Photographs of the advection of an initially vertical dyeline formed by dropping potassium permanganate crystals in cases a) $\eta = 1$, b) $\eta = 0.4$, c) $\eta = 0$, d) $\eta = -0.2$ and e) $\eta = -0.4$. Approximate time lapse after crystals dropped: a) 23 seconds, b) 68 seconds, c) 55 seconds, d) 35 seconds, e) 57 seconds. Heater is on the right, cooler is on the left. The photos were taken after the flow had reached thermal equilibrium. The dye streaks are representative of the time-mean circulation.

of the heat required to balance the cooling, or heating, of the cell from the adjacent cooling, or heating, coil. This would make the flow sensitive to any asymmetry about the ambient room temperature. The anticlockwise cell between the levels of the sources is primarily driven by a horizontal temperature gradient maintained by the vertical diffusion of heat to/from each of the sources (although sidewall heat transfer is also important in these experiments). When the heating source is 40 mm above the cooling source (figure 4.5*d*) there are only two anticlockwise cells. The reduced area between the sources is not deep enough to contain a cell; it is a transition region between the cell above the heating source and the cell below the cooling source. We do not show the case where the heat source is moved to the top boundary and the cold source to the bottom boundary, in which there is a single buoyancy driven anticlockwise cell, similar to that seen at mid-depth in figure 4.5*e*.

While re-calling that these experiments are poorly designed regarding sidewall heat transfer and carried out in order to check Sandström's (1908, 1916) report, we proceed to evaluate convection velocities, rather than arbitrarily classifying them as 'weak' or 'vigorous'. The horizontal velocity maxima measured for each case are plotted in figure 4.6. These have been normalised by the average maximum horizontal velocity measured in the extreme case of maximum possible convection, (figure 4.3*a*), and plotted against the normalised height difference, η. The cases of heating and cooling sources at the same level, and heat source above cooling source, gave velocities 15 to 30% of those in the reference case. When insulation was added around all sides of the tank, the normalised maximum velocities for heating and cooling sources at the same level decreased to approximately 10%. Also plotted are the results for sources at the same level when both the sidewall and surface insulation were absent (keeping only the plastic cling film seal to prevent evaporation): the normalised velocities are around 20%. These velocities correspond to a Péclet number $Pe = \frac{uh}{\kappa} \sim 10^3$ (based on the half depth h of water).

The significant velocities (relative to the extreme reference case) and the large Péclet number both warrant the description of 'strong' or 'vigorous' flow. It is likely that the measured flows for $\eta \leq 0$ were strongly influenced by sidewall heat transfer, which will increasingly replace vertical conduction through the interior of the flow when the heat source is raised further above the cooling source. Hence the velocities do not continue to decrease with η in these experiments for $\eta < 0$. However, we conjecture that, had there been no side wall heat loss or gain, the velocities would have continued to decrease with decreasing η.

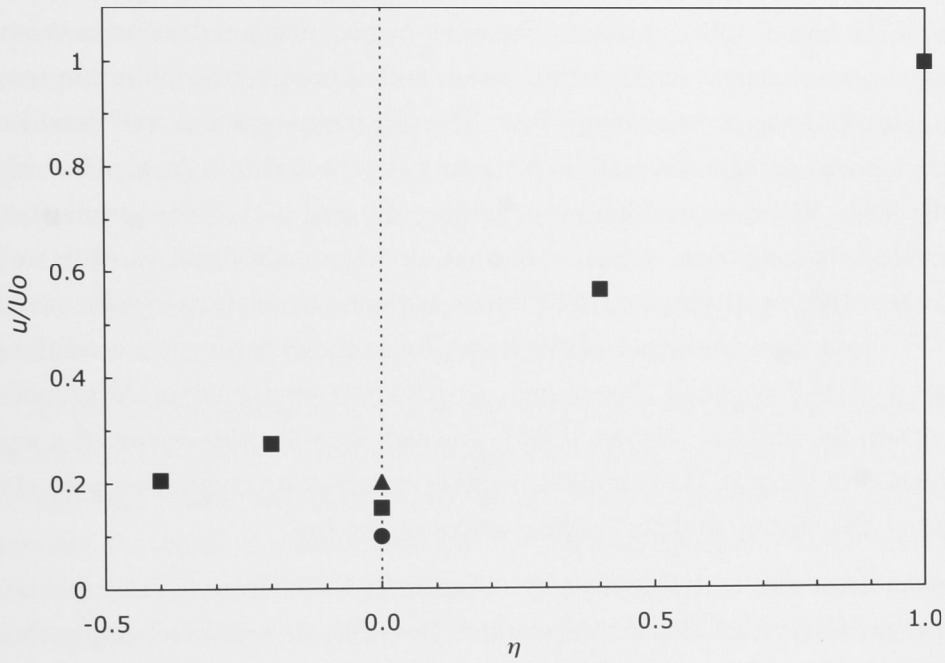

Figure 4.6: The measured maximum horizontal velocities as a function of the normalised height of the cooling source relative to the heating source. Each point represents the average of the upper and lower horizontal velocity maxima. Velocities are normalised by $U_0 = 8.54\,\mathrm{mm/s}$, the average of the upper and lower maximum horizontal velocities in the extreme case of figure 4.3*a*. Squares - foam insulation on the water surface and plastic cling seal; triangles - no insulation other than plastic cling seal; circles - foam insulation and seal on water surface as well as insulation on all walls.

4.4 Concluding remarks

Our aim here was to re-examine and explain the puzzling experimental observations of Sandström (1908, 1916). Despite a close reconstruction of his apparatus and methods we were unable to obtain results consistent with his report of no sustained circulation for heating and cooling sources at the same level or for the heat source above the cooling source. We conclude that his report was incorrect. The error may have occurred because the steady states (even at $\eta = 1$) have velocities much smaller than those of the initial transient flows. The order-of-magnitude reduction in velocities during the development of the stratification and approach to equilibrium may have been interpreted as a "vanishing" flow. The apparatus was not well designed for thermal convection, and side wall heat transfer is expected to have significantly affected the flow. However, we found that adding sidewall and surface insulation, which decreased the long term velocities, did not alter the main result: heating and cooling sources at the same geopotential led to a sustained circulation (characterised by large Pe) throughout the depth of the box. Under the experimental conditions this was not a 'slow' flow (small Pe), as some authors have envisaged on the grounds that it is driven by diffusion (Defant, 1961). Instead the velocities remained a significant fraction of those in the strongest possible steady-state convection with the heat source at the bottom and the cooling source at the top.

Heat must enter and leave the fluid by diffusion at the sources (or at a boundary), as it does in Rayleigh-Bénard convection. However, this does not imply that flow must be sluggish or laminar, as large temperature gradients across the boundary layers can facilitate large buoyancy fluxes. What is different in horizontal convection (in the absence of side wall heat transfer) compared with Bénard convection, however, is that circulation depends to some extent on interior vertical diffusion through the depth of the circulation (Hughes & Griffiths, 2006; Jeffreys, 1925; Killworth & Manins, 1980; Manins, 1973). In our experiments the depth of the circulation is always the depth of the box. The requirement that there be a matching diffusion of heat through the depth of overturning imposes a greater constraint on the overturning rate, relative to Bénard convection, and a bound on the viscous dissipation of mechanical energy (Paparella & Young, 2002). It also makes the flow only weakly dependent on the relative heights of the heat input and withdrawal. In our steady state laboratory experiments, the warm and cold plumes continued to reach the top or bottom of the box, respectively, in all cases, because the plume fluxes to those upper and lower regions were balanced by a combination of vertical diffusion of heat and sidewall heat transfer. The initial transient flows can be much faster than the

steady flows, but this interesting aspect of the system is beyond the scope of this thesis.

In Sandström's experiments, the heating and cooling sources had surface areas that were small relative to the horizontal area of the box. The experiments of Rossby (1965), Mullarney *et al.* (2004) and Wang & Huang (2005), on the other hand, used heating and cooling distributed over the full surface area of one horizontal boundary of a box. This arrangement allowed larger heat fluxes, hence a faster circulation, for a given temperature difference. The effect of sidewall heat transfer in the above experiments was greatly reduced compared with that in the Sandström-style experiments, by virtue of the greater heat throughput, effective thermal insulation schemes and large box width (larger ratio of fluid volume to surface area). Two-dimensional numerical solutions have addressed the case of no sidewall heat loss, and also the sensitivity of the flow to sidewall heat transfer (Mullarney *et al.*, 2006). The result in all of these studies was again a substantial circulation. We note that the numerical solutions show that the interior circulation maintains a stable vertical density gradient as a result of diffusion through the depth of the overturning.

As the Rayleigh number becomes infinitely large, we expect the effects of vertical diffusion in the interior to vanish. Hence the density gradient and the buoyancy of the end-wall plume will both vanish in the interior. In that limit the plume will ventilate the whole of a well-mixed interior while diffusion will be confined to a very thin boundary layer. This state is more closely approached in solutal experiments, such as those of Pierce & Rhines (1996), in which molecular diffusion of solute is so small and the buoyancy fluxes achieved are so much greater than in thermal convection experiments, that the flux-based Rayleigh numbers achieved are around five orders of magnitude larger. Such experiments involve volume fluxes from sources of salt solution and freshwater and require a withdrawal of volume (through a sink that was placed at the surface) to match the two input volume fluxes. The flow approaches a steady state in which the salinity at the sink is forced to be equal to the average salinity of the two inputs. Hence the flow and density stratification are inadvertently controlled by the sink location (as in double-diffusive experiments with two sources and a volume sink; Turner & Veronis, 2000), while the volume throughput may also influence the stratification that is maintained (by the small solute diffusivity) against vertical advection. However, further experiments with sources of salt solution and freshwater at differing levels, concentrating on earlier quasi-steady states and using mechanical stirring to enhance vertical diffusion (as in Whitehead & Wang, 2008), could test the flow patterns observed here while removing sidewall heat transfer effects.

Circulation owing to surface heating and cooling (of the oceans) has also been discussed on thermodynamic grounds. Bjerknes (1916), Defant (1961) and Huang (1999) viewed convection as a Carnot cycle, in which heating causes expansion at constant pressure, cooling causes contraction of volume at a constant (but different) pressure, and the cycle is closed by adiabatic paths between the high and low pressures. Marchal (2007) has developed a formal mathematical statement for the more general case of an unsteady convective flow with background rotation. Pressure forces can do net work (against friction) only if the heating of the fluid is at higher pressure than the cooling. Bjerknes (1916), Defant (1961) and Huang (1999) argued that for the oceans the surface heating is not at a higher pressure than the surface cooling, and so there can be no net work done, and no circulation. However, we point out that diffusion of heat (whether by molecular conduction or turbulent mixing) allows heat to enter and leave the fluid at the boundary and causes the heating (in the case of surface forcing of the oceans) to be distributed throughout at least the depth of the thermal boundary layer (the thermocline) and possibly through the full depth of the oceans. Ironically, Sandström (1908) recognised this. Warmed water ascends towards the surface after having warmed and expanded at pressures higher than the surface pressure (Hughes & Griffiths, 2006; Jeffreys, 1925).

The total amount of cooling which is equal to the amount of heating in a steady state, here is distributed over a portion of the ocean surface and is destabilising. The cooled water supports convective mixing in a surface layer, which on average deepens with increasing latitude (as also observed in laboratory experiments (Mullarney *et al.*, 2004). Surface cooling can also force a mean sinking flow as a plume, which then tends to cool the surrounding interior water by heat conduction or mixing. However, convective mixing from the surface and the deeper mixing of cold plume water with warmer surroundings produce merely a local redistribution of heat that entails equal amounts (in a Boussinesq fluid) of cooling and warming at the same depth. As there is no net thermal contraction of water associated with this convective part of the circulation, the convection does not increase the pressure at which the cooling takes place. Hence the relevant cooling in the thermodynamic cycle remains tightly confined to the vicinity of the surface, and is at lower pressures than the vertically distributed heating.

As an illustration, in the high Rayleigh number experiments of Mullarney *et al.* (2004) (which were inverted, so that heating and cooling from the bottom have destabilising and stabilising roles, respectively) the heating took place in a conductive boundary layer just $\sim$1 mm thick beneath a layer of convective mixing that was approximately 20 mm thick. Both of these lay beneath the thicker conductive

thermocline throughout which the water experienced cooling. Thus as before we conclude that the role of diffusion leaves the magnitude of circulation insensitive to small changes in the relative height of the heating and cooling sources. Indeed, Jeffreys (1925) concluded that "the relative levels of the sources of heat and cold have nothing to do with the argument" regarding the presence of a convective circulation. Positive work is available from the heating and cooling cycle, even when the heating source is above the cooling source. There is no basis for Sandström's 'theorem'.

Chapter 5

Experiments with non-monotonic thermal forcing at the base

In this chapter we investigate the circulation maintained by differential thermal forcing applied along one horizontal boundary of a long box such that the supply of buoyancy is destabilising near both ends and stabilising near the centre. In the ocean the thermal forcing is predominantly applied at the surface and consists of net heating at equatorial latitudes and net cooling towards the two poles. In the laboratory we force the bottom boundary and therefore cool at the center of the base and heat at the two ends of the base. Confined downwelling or upwelling plumes are maintained in the polar or endwall regions of the flow. Paparella & Young (2002) report numerical solutions for a related case having surface heating at both ends and cooling at the centre. This configuration leads to a single downwelling plume at the centre of the box.

In the ocean the pattern of the 'conveyor belt' basin circulation is dependent on rotation (Stommel, 1958). However for the purpose of this thesis we do not include the effects of rotation. In the ocean the isopycnals are horizontal, implying the lateral transport is much faster than the vertical transport, and as such, the interior temperature structure of the MOC can be considered one dimensional.

5.1 Apparatus and Procedure

5.1.1 The tank

Experiments were conducted in an acrylic tank, of length $L = 1.25\,\mathrm{m}$, height $D = 0.20\,\mathrm{m}$ and width $W = 0.15\,\mathrm{m}$, filled with de-aired water, see figure 5.1. The front and back sidewalls were double glazed with an inner wall that was 19 mm thick and

an outer wall that was 3.5 mm thick. The gap was filled with Argon gas and was 18 mm wide. The endwalls and the lid were 19 mm and 10 mm thick, respectively. The tank base consisted of a 10 mm copper sheet sitting on top of (and in contact with) a heat exchanger in the center of the tank (length 0.63 m and width 0.15 m) with a heating mat (length 0.30 m and width 0.15 m) at either side. The water that circulates through the heat exchanger is kept at 16°C by a temperature controlled water bath. The water channels in the heat exchanger were arranged so that a channel carrying water that had been in the exchanger for t seconds was situated next to the channel carrying water that had been in the exchanger for $t_{total} - t$ seconds, where t_{total} is the total flow time through the heat exchanger. This ensured a nearly spatially uniform applied temperature from the heat exchanger. The heating mats applied a uniform heat flux over their entire area. Over the lifetime of this project two different power controllers were used to set the heat flux. The first controller (experiments 2 - 16; see table 5.1) used a thyristor with a power meter added into the circuit to measure the resultant power output. However the mains supply did not give a sufficiently constant voltage, and the power from the thyristor contained variations up to 10 W in amplitude. The second power controller (experiments 17 - 30; see table 5.1) was specially designed to deliver a power constant to within 0.1 W.

In addition to the double glazed sidewalls the heat transfer with the surroundings was further minimized by insulating the sidewalls of the tank with 45 mm thick Styrofoam and the endwalls with 100 mm thick Styrofoam. The lid insulation was 100 mm thick. The entire tank sat upon a 100 mm thick Styrofoam layer on a wooden table top. The insulation on the sidewalls was only removed when taking temperature profiles and visualising the flow.

There were 10 interior thermistors positioned in the water throughout the tank, see figure 5.1*a*. Five thermistors were all placed at a height $z/D = 0.025$ (the base being $z/D = 0$) and positioned horizontally at $x/L = 0.08$, 0.24, 0.5, 0.72 and 0.92 (the left endwall being $x/L = 0$). One thermistor was placed at $z/D = 0.15$, $x/L = 0.5$, and the final two interior thermistors were placed at the same height, $z/D = 0.85$, but near either end of the tank, at $x/L = 0.24$ and 0.72. Holes along the length of the tank, eight along the center of the lid and three off-set slightly towards the front by $\Delta y/W = 0.17$ (see figure 5.1*b*) allowed the interior temperature measurements and flow visualisation to be undertaken with minimal influence from the sidewalls. The temperature in the centre of each section of the base was monitored by thermistors embedded in the copper base.

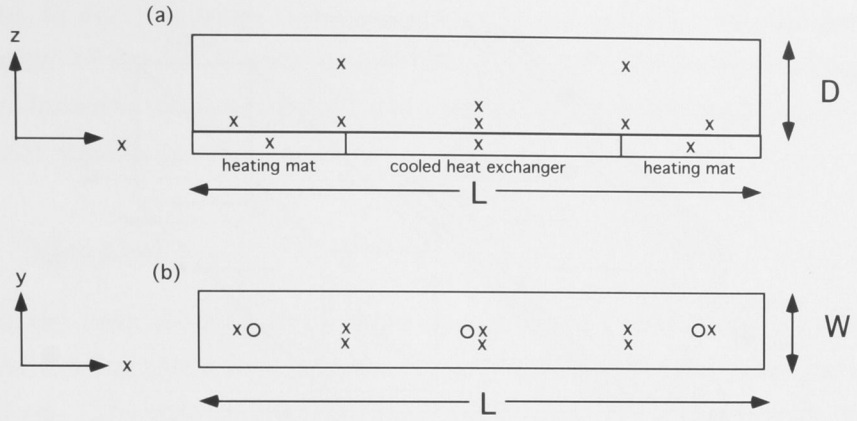

Figure 5.1: (a) Side view of the location of thermistors inside the tank, (b) top view of the location of thermistor tubes, ×, and visualisation holes, ○, in the lid of the tank.

5.1.2 Flow visualisation

A rectangular board of white expanded PVC (1.5 m long by 0.3 m high) was placed behind the experimental apparatus at an angle of about 60 degrees to the horizontal. Three fluorescent light tubes were placed above and below the expanded PVC board so that the light reflects off the board and travels through the tank (see figure 5.2). Each endwall contained a plug at $(z, y) = (10\,\text{mm}, 7.5\,\text{mm})$ to enable a thin hypodermic needle to be placed inside the tank. This allowed the introduction of neutrally buoyant food dye for visualisation of the circulation. The dye is advected with the flow and can be clearly seen against the white background. Full strength food dye was diluted to one part in nine or one part in ten (for blue and red dye, respectively) with distilled water. The final density for each colour was very close to 1.001 kg/m^3. Salt was added to the de-aired water in the tank ($\sim$ 0.3%) for experiments 19 - 30 to make the diluted food dye neutrally buoyant. Crystals of potassium permanganate were used to produce vertical dye lines. The subsequent distortion of dye lines gave a qualitative picture of horizontal velocities.

Photos were taken using a Nikon D100 digital camera and digital video was recorded using a Sony HDV handycam. The digital video record required leaving the sidewall insulation off for the entire visualising time, thus leading to an increase in the small heat losses from the tank. These losses lead to a cooling of the fluid near the sidewalls and a weak subsequent flow down the sidewalls. This water falls as far as the top of the boundary layer because it is not cooled enough to penetrate into the boundary layer. This effect is confined to the sidewall and does not directly affect flow in the tank interior. Hence the small portion of dye which enters the

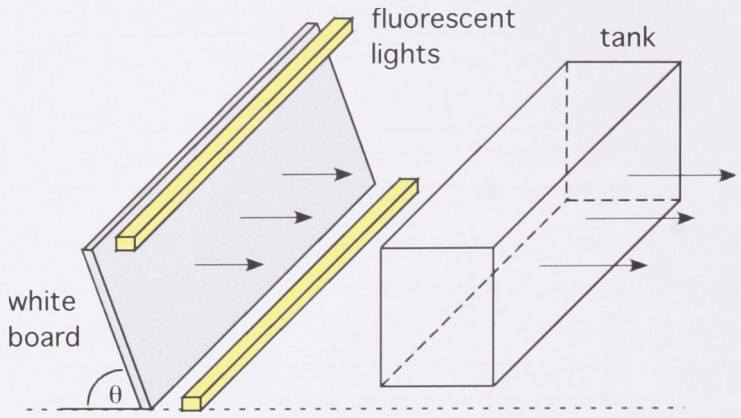

Figure 5.2: Sketch of the setup to illuminate the tank used for the horizontal convection experiment.

sidewall boundary layers is not representative of the flow through most of the tank width. When digital video was not required the insulation was replaced between still photographs and other visual measurements.

5.1.3 Temperature measurement

Vertical temperature profiles were obtained with the use of a traversing mechanism. Individual thermistors were mounted at the end of a 300 mm long section of stainless steel syringe tubing. All of the thermistors were attached to a horizontal bar, which could be secured to the traversing mechanism. This design allowed the entire rack of thermistors to be removed from the tank when cleaning was required, and for the positions of thermistors, relative to each other, to be kept constant.

Normalised temperatures are defined by

$$T^* = \frac{T - T_c}{\overline{T_{1/2} - T_c}}, \tag{5.1}$$

where T_c is the temperature of the cold plate, as measured by the thermistor embedded in the centre of the cold plate, and $\overline{T_{1/2} - T_c}$ is the average over experiments with nominally equal flux applied to either end of the tank, of the temperature difference between $z/D = 0.5$ and the cold plate.

We use the same apparatus as that of Mullarney *et al.* (2004) and can therefore use their value of the heat loss coefficient from the insulated box. They found the heat loss (W) to be $0.7425 \times (T_{tank} - T_{lab})$, where T_{tank} is the average interior temperature of the tank in steady state and T_{lab} is the laboratory temperature.

Therefore, in our two series of experiments, $2-16$ and $17-30$, the heat loss as a percentage of the total input heat is 2.7% and 3.2%, respectively. Thus the net difference between the heat applied and the heat removed through the bottom base plate is not significant.

5.1.4 Method

We filled the tank with de-aired water then lowered the thermistor rack into the tank. The heating mats, heat exchanger and thermistor logging program were then switched on. The approach to thermal equilibrium was monitored by plotting a time series of the temperatures logged at 10 second intervals. Thermal equilibrium was judged to be reached after the interior mean temperature had been stationary for at least one day. The approach to thermal equilibrium typically took five days. Once the flow was in thermal equilibrium the traverser was used to measure vertical profiles at the five x positions shown in figure 5.1. A measurement was taken every 0.01 mm and the results averaged over 10 readings to give a vertical resolution of 0.1 mm. This averaging widow removes bit level noise in the digitised record while maintaining sufficient resolution. Observations of the flow were made using potassium permanganate crystals and neutrally buoyant food dye.

The following parameters were all held constant for this set of experiments: the aspect ratio

$$A = \frac{D}{L}, \tag{5.2}$$

where D is the tank height and L is the tank length; the Prandtl number

$$Pr = \frac{\nu}{\kappa}, \tag{5.3}$$

where ν is the kinematic viscosity and κ is the thermal diffusivity; and the flux Rayleigh number

$$Ra_F = \frac{g\alpha F_T L^4}{\rho_0 c_p \kappa^2 \nu}, \tag{5.4}$$

where g is the gravitational acceleration, α is the thermal expansion coefficient, F_T is the heat flux ($\mathrm{W/m^2}$) supplied by the heating mats, ρ_0 a reference density and c_p the specific heat capacity.

The parameter we varied was the heat flux ratio

$$R_Q^* = \frac{H_2 - H_1}{H_{total}}, \tag{5.5}$$

where H_1 is the rate of heat input (W) from the left heating mat, H_2 is the rate of

heat input (W) from the right heating mat and H_{total} is the total rate of heat input, $H_1 + H_2$, from the heating mats.

Initially the two heating mats were set to supply 140 W at each end, giving $F_T = 3111\,\mathrm{W/m^2}$. The next experiment consisted of increasing the flux through one mat at the expense of the other (thus keeping the total heat input into the tank constant). The adjustment was often made to each power controller without restarting the experiment from room temperature. A series of experiments were thus carried out and, following each new power setting, the experiment was left to reach thermal equilibrium, which took about five days. The methodology of systematically increasing R_Q^* to our maximum (positive value), then decreasing it to the minimum (negative value) and finally increasing it back to $R_Q^* = 0$ was to look for hysteresis in the system. However, none was found. In thermal equilibrium the heat supplied to the tank (through the heating mats) is exactly balanced by the heat removed by the cooling exchanger (ignoring the minimal heat loss to the surroundings). For a given heat input the temperature of the water bath and cold plate control the flow temperature at thermal equilibrium.

When the heating mats at each end were set to supply the same amount of power (regardless of whether the thyristors or the more sophisticated power controllers were in use) the circulation was systematically biased towards one end. The size of the asymmetry was consistent over the R_Q^* range explored in this thesis. Despite an extensive search the source of the asymmetry was not found. Further, an internal flow mechanism to support the bias is not known. Therefore, we apply a correction to all R_Q^* values based on the observed asymmetry in measurements of the horizontal position of the confluence point of the two plumes. The correction was found to be

$$R_Q = R_Q^* - 0.0357. \tag{5.6}$$

Thus R_Q refers to the corrected data, and the flow was symmetric about the centre of the box for $R_Q = 0$. The term 'nominal heat flux ratio' refers to R_Q^* based on the original instrumental settings for that experiment.

Due to a calibration error in the second power controller the total heat input to the tank in the second series of experiments was 310 W instead of the desired 280 W. The noticeable impact of this $\sim$ 10% increase in the heat input was to increase the average interior temperature and the top-to-bottom temperature difference. Therefore, all parameters were evaluated at the average interior temperature for each experiment. We were also able to adjust the top-to-bottom temperature

Table 5.1: Experimental Parameters. The physical properties of water at the average interior temperature were used to calculate Ra_F for each experiment. For experiments $2 - 16$ the average interior temperature was 33°C, while for experiments $17 - 30$ the average interior temperature was 35°C.

Experiment	H_1 (W)	H_2 (W)	R_Q	Ra_F	Pr
2	140	140	-0.0357	3.575×10^{14}	5.10
3	140	140	-0.0357	3.575×10^{14}	5.10
4	139	141	-0.0286	3.575×10^{14}	5.10
5	137	142	-0.0179	3.575×10^{14}	5.10
6	135	145	0	3.575×10^{14}	5.10
7	130	150	0.0357	3.575×10^{14}	5.10
8	125	155	0.0714	3.575×10^{14}	5.10
9	115	165	0.1429	3.575×10^{14}	5.10
10	115	165	0.1429	3.575×10^{14}	5.10
11	125	155	0.0714	3.575×10^{14}	5.10
12	130	150	0.0357	3.575×10^{14}	5.10
13	135	145	0	3.575×10^{14}	5.10
14	138	142	-0.0214	3.575×10^{14}	5.10
15	140	140	-0.0357	3.575×10^{14}	5.10
16	140	140	-0.0357	3.575×10^{14}	5.10
17	156	154	-0.0422	4.309×10^{14}	4.86
18	158	152	-0.0551	4.309×10^{14}	4.86
19	158	152	-0.0551	4.309×10^{14}	4.86
20	161	149	-0.0744	4.309×10^{14}	4.86
21	166	144	-0.1067	4.309×10^{14}	4.86
22	171	139	-0.1389	4.309×10^{14}	4.86
23	181	129	-0.2035	4.309×10^{14}	4.86
24	171	139	-0.1389	4.309×10^{14}	4.86
25	166	144	-0.1067	4.309×10^{14}	4.86
26	161	149	-0.0744	4.309×10^{14}	4.86
27	158	152	-0.0551	4.309×10^{14}	4.86
28	161	149	-0.0744	4.309×10^{14}	4.86
29	158	152	-0.0551	4.309×10^{14}	4.86
30	156	154	-0.0422	4.309×10^{14}	4.86

difference by using the scaling from Hughes *et al.* (2007) (see equation 2.11 or 5.7) which relates the top-to-bottom temperature difference to the flux Rayleigh number.

5.2 Results

5.2.1 Qualitative observations

The flow in the bottom boundary layer was similar for all R_Q values investigated. The heating near the ends of the tank and cooling in the centre of the tank establishes a temperature and pressure gradient along the base. Cold water from the centre of the tank is drawn towards the heated ends of the base where it gains buoyancy and rises up the endwalls as unsteady, eddying plumes. The convective mixed layer (CML), first described by Mullarney *et al.* (2004), was also present in these experiments. However, the experiments presented in this chapter had the heat input divided between the two end regions whereas the Mullarney *et al.* (2004) experiments had the heat input towards one end. Although the total heat input was the same, the convective mixed layers feeding each of our plumes were therefore shorter, less vigorous and thinner than the CML in the single plume Mullarney *et al.* (2004) experiments. Depending on the heat flux ratio three different circulation regimes were observed:

Regime 1: For $R_Q = 0$ the flow was observed to be almost symmetric about $x/L = 0.5$ (see figure 5.3). Each plume rises through the full tank depth and feeds into an outflow along the upper boundary. There is some mixing at the confluence point (the point where the outflows from the two plumes meet), but essentially the water from each plume turns under itself and travels back towards its original end. It is then either entrained into the plume or advected into the bottom boundary layer. The flow in the stable bottom boundary layer at the mid-point of the box is almost stationary so that on either side of the mid-point the boundary layer flow is towards the closest endwall. The direction of flow above this boundary layer is controlled by the position of the confluence of the two plumes.

Regime 2: Moderate values of R_Q, $0.02 < |R_Q| < 0.1$, fall into this regime. As for regime 1 both plumes penetrate through the full tank depth and feed outflows along the upper boundary, see figure 5.4. However the outflow from the stronger plume, which is usually visibly more turbulent, has larger velocities and penetrates in the horizontal beyond the mid-point of the tank to the confluence point. Some

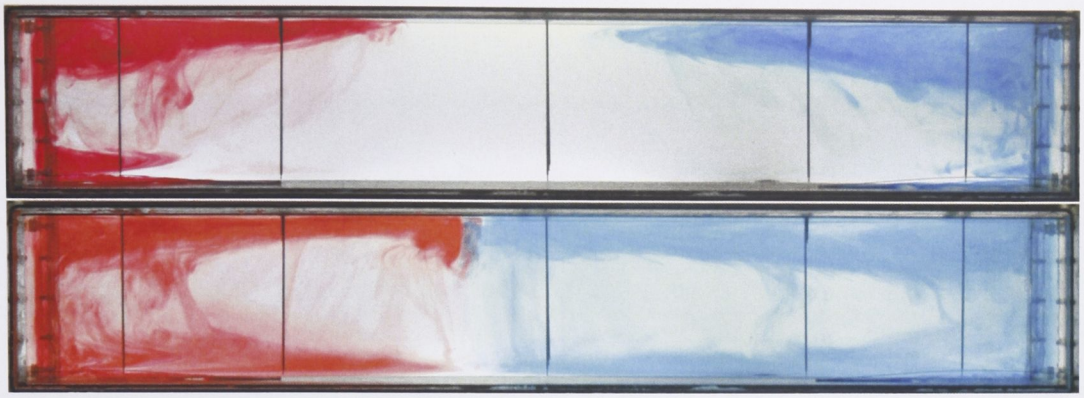

Figure 5.3: Flow visualisation of the circulation for regime 1, $R_Q = 0$. Neutrally buoyant food dye was injected into the bottom boundary layer $\sim 1/4$ of the way along the tank from each end. The initial release of the two colours occurred about the same time. The dye was advected towards the respective endwalls in the convective mixed layer and then rose into the tank interior in the endwall plumes. The time elapsed between the two photos is $\sim$ 20 minutes. The dye that is sitting on top of the thermal boundary layer in the second photo is not indicative of the bulk of the circulation in the tank, as discussed in section 5.1.2. The thermistors are visible as dark vertical lines.

mixing is evident at this point, then both outflows turn back underneath the stronger plume outflow. The circulation in the remaining bottom two thirds of the tank consists of a broad flow towards, and subsequent entrainment into, the dominant plume, and a slow downwelling into the bottom boundary layer. Disturbances originating from the mixing at the confluence point propagate towards the strong plume end, along the shear interface between the strong plume outflow and the return flow underneath it.

Regime 3: For $|R_Q| > 0.1$ one plume is buoyant enough to prevent the second plume from reaching the upper boundary, see figure 5.5. The outflow from the stronger plume penetrates right along the upper boundary, turns the corner and may flow down the endwall as far as $z/D = 0.25$. The weaker plume, not having enough buoyancy or momentum to force its way to the top, intrudes into the interior above the boundary layer and below the water from the strong plume outflow (which flows down the weaker plume's endwall and then intrudes). Thus there is a slow horizontal flow in the interior towards the strong end (with entrainment into the stronger plume) and an even slower downwelling into the bottom boundary layer.

Figure 5.4: Flow visualisation of the circulation for regime 2 ($0.02 < |R_Q| < 0.1$). Neutrally buoyant food dye was injected into the bottom boundary layer $\sim 1/4$ of the way along the tank from each end. The initial release of the two colours was at different times, red injected about 10 minutes before blue. The dye was advected towards the respective endwalls in the convective mixed layer and then rose into the tank interior in the endwall plumes. The time elapsed between the two photos is ~ 20 minutes. The red dye that is sitting on top of the thermal boundary layer in each photo is not indicative of the bulk of the circulation in the tank, as discussed in section 5.1.2. The thermistors are visible as dark vertical lines.

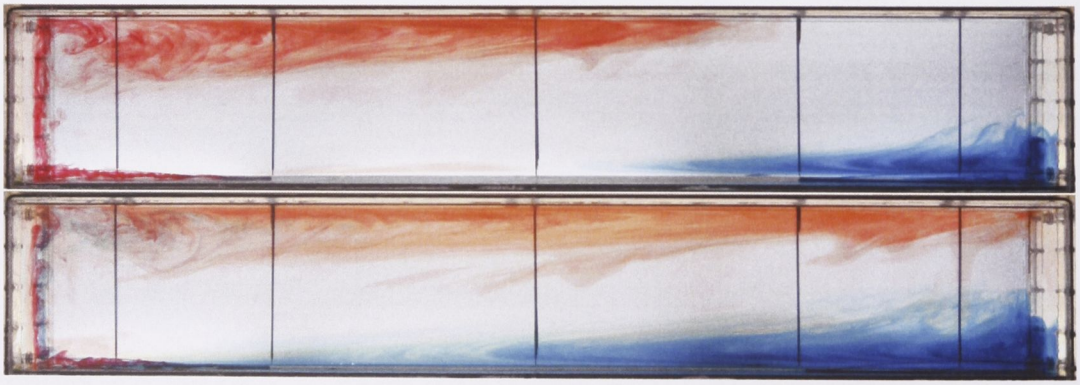

Figure 5.5: Flow visualisation of the circulation for regime 3 ($|R_Q| > 0.1$). The dye was injected as described for figure 5.4. The time elapsed between the two photos is ~ 13 minutes.

5.2.2 Quantitative measurements

The horizontal position, x_c, of the confluence of the two plume outflows was measured for all experiments. When the location of the confluence is on an endwall it is counted as being at either $x_c = 0$ or 1.25 m. Figure 5.6 plots the normalized horizontal position of the confluence point, x_c/L, against the ratio of the input heat fluxes. The largest error in the measurement x_c was the time variation of the confluence point, rather than the accuracy to which we could measure the point at any one time. Thus we base the error bars on the range of observed confluence point positions. We include the regime boundaries in figure 5.6. The gradual transition between regimes 1 and 2 is in contrast to the sudden change in slope of the confluence point data between regimes 2 and 3. In regimes 1 and 2 both plumes are continuing to reach through the full depth of the tank so that they are both competing for interior fluid to entrain. However the transition between regime 2 and 3 is a fundamental change in the circulation, because one plume is prevented by the other from extending through the full depth of the tank and so there is no competition for interior fluid. To better explore regime 3 we introduce, z_{weak}, the penetration

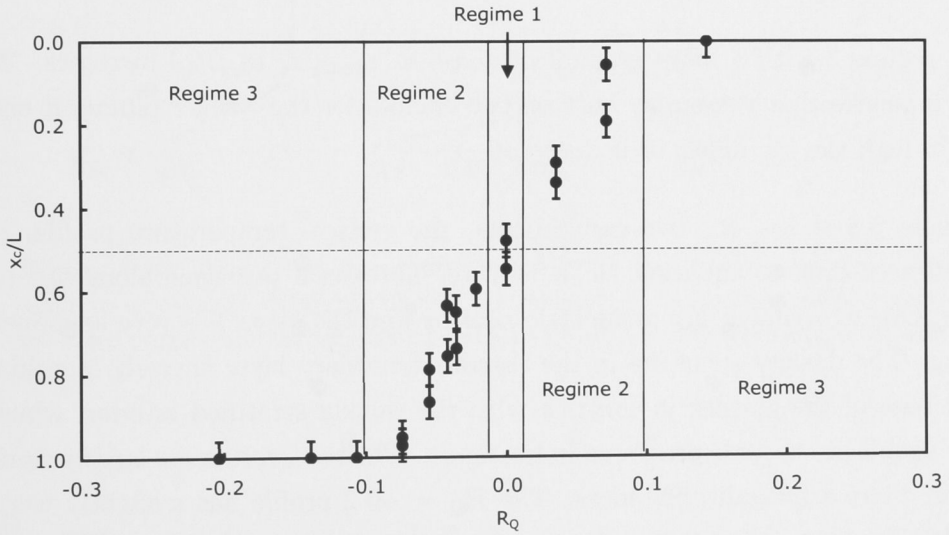

Figure 5.6: Location of the confluence point, x_c (normalized by L), of the two plumes against the ratio of input heat fluxes, R_Q. The flow regimes are superimposed on the graph.

height of the weaker plume up the endwall. Figure 5.7 plots z_{weak} normalised by the tank depth against the ratio of the input heat fluxes. Again we have used the variation in time of z_{weak} to place the error bars on these data points. Figure 5.7 shows a sharp drop in the penetration height of the weaker plume when the flow first

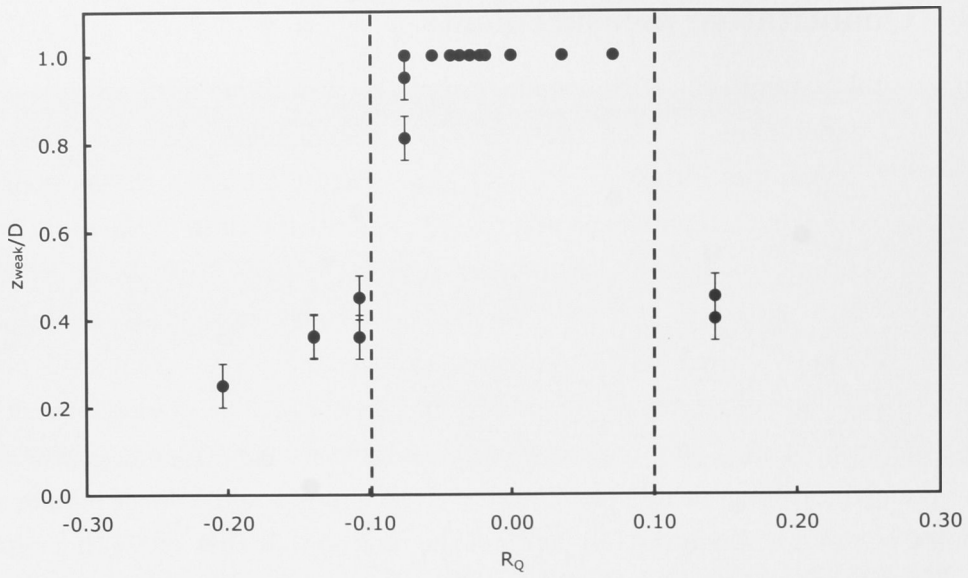

Figure 5.7: Penetration height of the weaker plume, z_{weak}/D. The vertical dashed lines show the regime 2-3 boundary.

enters regime 3 with a more gradual decrease in z_{weak}/D as $|R_Q|$ increases. This figure indicates that there may only be two choices for the weaker plume, it either rises through the full depth or it does not.

Figure 5.8 shows, for two experiments, the vertical temperature profile, normalised according to equation (5.1), at three horizontal positions along the tank length. One experiment has symmetric heating and the other has very asymmetric heating. The density structure in the thermal boundary layer is easily identifiable at the base of the graphs, in contrast with the weakly stratified interior, which is barely visible at the scale presented in the figure. The two profiles are largely similar, however there are small differences. The $R_Q = -0.2$ profile has a slightly warmer boundary layer at $x/L = 0.24$ reflecting the greater heat input at that end, and the interior gradient is slightly larger for the same experiment at $x/L = 0.76$.

The vertical temperature profiles measured in the centre of the tank have been used to calculate the interior stratification in each experiment (figure 5.9). The temperature gradient (°C/m) for each profile was measured by fitting a linear profile between $0.4 \leq \frac{z}{D} \leq 0.7$. This gradient was normalised by the tank depth, D, divided by $T_{1/2} - T_c$. Using the theory from Hughes & Griffiths (2008) (our equation 2.11), the data from the second series, experiments 17 - 30, have been scaled by a

multiplying factor of

$$\frac{\Delta T|_{max}\,(280\,W)}{\Delta T|_{max}\,(310\,W)} = \left[\frac{H_{total}\,(280\,W)}{H_{total}\,(310\,W)}\right]^{5/6} = 0.9^{5/6} = 0.92, \tag{5.7}$$

to adjust for the increased total heating applied to the second series.

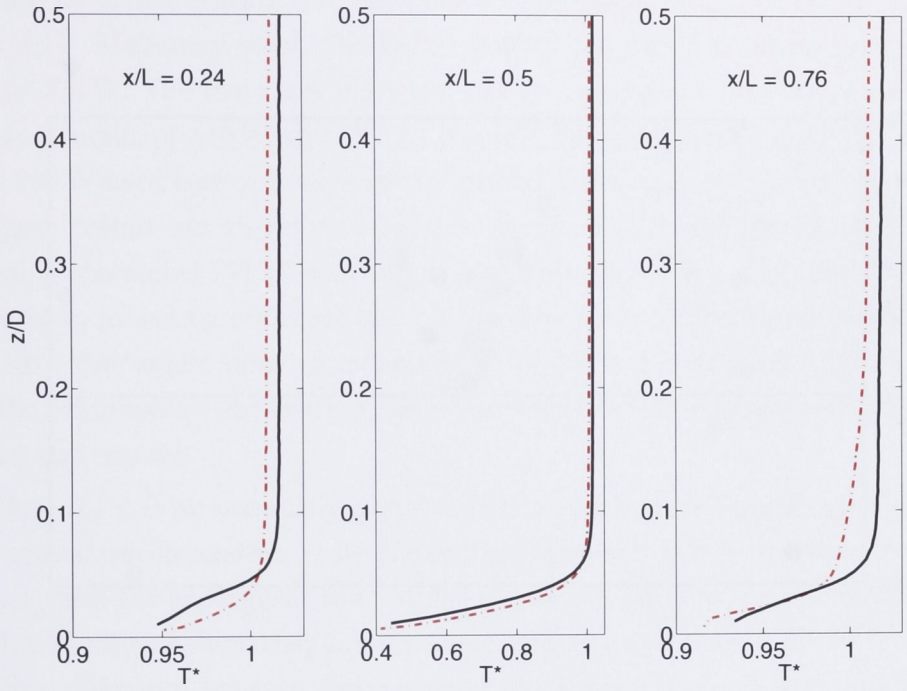

Figure 5.8: Normalised temperature profiles for two experiments with R_Q equal to -0.04 and -0.20, the black solid line and red dashed line, respectively, for three horizontal positions along the tank. Note the different horizontal axis scales.

5.3 Discussion

The R_Q parameter space that we explore with the present experiments (blue dots in figure 5.9) extends over the range $|R_Q| \lesssim 0.2$. We find that the normalised stratification doubles as the magnitude of R_Q increases from 0 to 0.2. We do not expect the stratification to change beyond this because the circulation is in regime 3 and the stronger plume is dominating the flow. To achieve $|R_Q| = \pm 1$ the heat flux must be applied through one heating mat only. This situation will give rise to a box-scale overturning circulation driven by just one plume. The main difference between

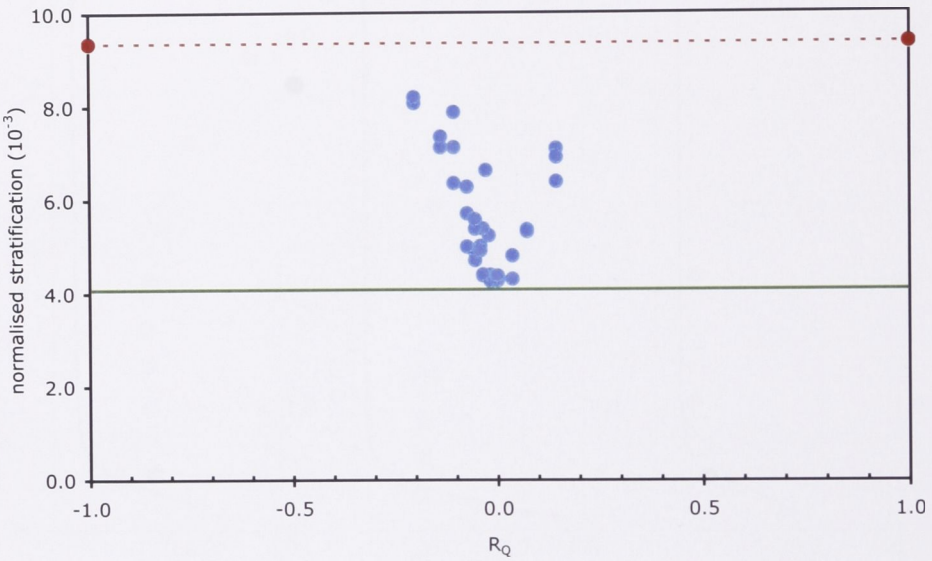

Figure 5.9: Interior stratification at $x/L = 0.5$ normalised by, D divided by $T_{1/2} - T_c$, for the experiments reported in this chapter (blue dots). Also included is an upper bound extrapolated from the results of Mullarney *et al.* (2004) which can represent the extreme case ($R_Q = 1$ or -1, red dots, connected by dashed line), and a lower bound extrapolated from the same authors (green line). See section 5.3 for the full details.

an experiment with $R_Q = \pm 1$ (using the apparatus presented in this chapter) and those of Mullarney *et al.* (2004) is the nature of the bottom boundary condition. The forcing on the bottom boundary in Mullarney *et al.* (2004) consisted of an imposed flux condition over the left half of the base and a constant temperature condition applied over the right half of the base. This contrasts with the present configuration with a constant temperature condition over the centre half of the base and all of the heating through either the left or right quarter of the base (for $R_Q = \pm 1$). Mullarney *et al.* (2004) investigated several heat inputs ranging from 10 W to 374 W. The two cases most relevant for comparison here are those using a total heat input of 140 W and 271 W. The 3% increase in heat input from 271 W to the 280 W used here will increase the stratification by only 2.7% (equation 2.11). An upper bound can therefore be placed on the normalised stratification (figure 5.9) using the scaled 271 W heat input data from Mullarney *et al.* (2004) (the red data points, joined by a dashed line in the same figure). This upper bound lies at 9.1×10^{-3}; the largest value we measure (for $|R_Q| \sim 0.2$) is 8.8×10^{-3}. This suggests that the temperature structure is not particularly sensitive to the configuration of heating and cooling.

When $R_Q = 0$ we nominally supply 140 W to each plume and observe an essentially symmetric circulation about the centre of the box. It is instructive to compare this case with the experiment from Mullarney *et al.* (2004) for a single plume forced by a 140 W input (where they measured the stratification to be 4.4×10^{-3} °C/mm). The only difference between this case and one overturning cell from our $R_Q = 0$ experiment is that the horizontal scale in our case is halved. Using the scaling from Hughes *et al.* (2007) (their equation 4.3) one can adjust for the different horizontal scales and we find for the one plume experiment (allowing for the horizontal scale to be effectively doubled) that the top-to-bottom density difference will need to be reduced by a multiplying factor of $2^{1/3} = 0.79$ for comparison with the two plume data. This gives a lower bound for our data of 4.1×10^{-3} (green line in figure 5.9).

We see in figure 5.9 the normalised stratification for the fixed total heat input of 280 W varying from the two 140 W plumes at $R_Q = 0$ and quickly approaching the upper bound of a single 280 W plume at $R_Q = 0.2$. Thus figure 5.9 shows that the interior stratification for one plume in a box will be similar to the interior stratification for two plumes in the same box, if each plume is supplied with the same buoyancy flux, F_0. Similarly if the flux supplying the two plumes in one box is made unequal then the stronger plume will control the interior stratification.

Hughes *et al.* (2007) define the dimensionless thickness of the thermal boundary layer in two ways, as either, $\delta_{0.95}$, the region incorporating 95% of the top-to-bottom

density difference or δ_e, the thickness incorporating $1 - e^{-1}$ of the top-to-bottom density difference. They find that the specific buoyancy flux at these heights, $F(\delta_{0.95})$ or $F(\delta_e)$, takes well defined values. The ratio of the specific buoyancy in the plume at a height of $z = \delta_{0.95}$ to the specific buoyancy at the base of the plume is ≈ 0.14. Outside the thermal boundary layer the plume therefore retains less than 14 % of its original buoyancy. When a second plume is introduced we expect that it will intrude at levels about the top of the boundary layer if $F_2 \lesssim 0.86F_1$, or at a greater depth if $F_2 > 0.86F_1$. Here, F_1, F_2 are the buoyancy flux of each plume in the box. When $F_2 = 0.86F_1$, $R_Q = |0.075|$, which compares well to the boundary between regime 2 and 3 at about $R_Q \approx 0.1$ (figure 5.6). For R_Q greater than this critical value, the flow is in regime 3 and the second plume is not strong enough to intrude into the interior. The interior stratification will be governed by the stronger plume Killworth & Turner (1982).

A comparison with ocean data is informative here. Using the Levitus 1994 data set to calculate the interior stratification between depths of 1000 m and 5500 m, we found the normalised potential density gradient averaged over the whole ocean to be ~ 0.2. This is about 20 times more stratified than the strongest normalised interior stratification we measured in the experiments. Hence convection driven by two destabilising plumes in a simple rectangular geometry underestimates the interior stratification in the ocean. If the ocean is in a steady state we must look for other reasons to help explain the strength of the stratification. The normalised density gradients measured in the boundary layer in the experiments, on the other hand, are about two times larger than those in the ocean thermocline. Hughes *et al.* (2007) showed that plume geometry (eg. two dimensional or axisymmetric plume) is very important in influencing the density profile in an ocean basin, for which the dynamics of geostrophic currents on a slope need to be considered. The line plumes in our experiments are far from the highly turbulent entraining slope currents that carry Deep and Bottom waters to great depth in the Southern and the North Atlantic oceans and there should be no pretense that a simple laboratory geometry will yield the same stratification as that in the oceans. The aim has been, however, to examine the dynamics of the circulation with two sinking regions, and we have shown that for a given rate of buoyancy forcing, the interior stratification can increase by up to a factor of approximately two from the weakest value, obtained when the sinking regions are identical. In chapter 7 we extend the experiments of this section to examine the influence of a sill on the circulation and stratification.

Chapter 6

Numerical experiments with thermal forcing at the base

6.1 Numerical methods

To complement the laboratory results presented in Chapter 5 we ran a series of numerical experiments. In comparison to the laboratory results the numerical results provide a higher resolution data set of the velocity and temperature fields. The numerics also provide a stream function solution and an accurate record of the time variability for stream function, velocity and temperature. Therefore, in this chapter we are able to confirm the key results from Chapter 5 regarding the dominance of the stronger plume at $R_Q > 0.1$, and then use the data not obtainable in the laboratory to investigate the stream function, the horizontal velocity structure and the origins of the variability in the flow.

The two-dimensional momentum, continuity and heat equations were solved numerically using the computational fluid dynamics package FLUENT, version 6.2, on the ANU supercomputer facility, which is part of the Australian Partnership for Advanced Computing (APAC). The computations employ a finite-volume method. We used the two-dimensional implicit segregated solver with the PRESTO! interpolation scheme for pressure, the PISO algorithm for pressure-velocity coupling and the QUICK scheme for discretisation of the momentum and energy equations. The Boussinesq approximation was made and the fluid properties (κ, ν, $\rho_\circ$, c_p, α) were evaluated at the steady state temperature from the laboratory experiments. The solver is non-hydrostatic and a turbulence closure model is not required because the grid resolution and time steps are smaller than the Kolmogorov scales.

The grid was constructed using the package GAMBIT version 2.0, see figure 6.1. The solution grid was designed with the same overall dimensions as the laboratory

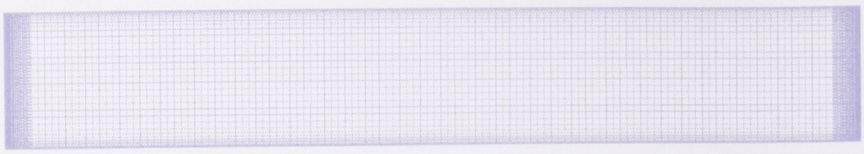

Figure 6.1: The two dimensional grid used for the numerical calculations.

tank from Chapter 5, having a depth of 0.20 m and a length of 1.25 m. The cell dimension in the interior of the grid was 10 mm × 10 mm and the boundary regions on all sides had a higher resolution. In most runs the higher resolution grid near the bottom and top boundaries consisted of 12 rows. The height of the grid cell next to the boundary was 0.5 mm and the height of each successive row of cells in the horizontal boundary region increased by a factor of 1.3. The total thickness of the region of higher resolution was therefore 37.2 mm ($z/D = 0.19$). The vertical endwall region of higher resolution consisted of 32 columns of cells. The width of the grid cell next to the vertical wall was 1 mm and the width of each successive column was increased by a factor of 1.015; this produced an endwall region of higher resolution that was 40.7 mm thick ($x/L = 0.03$). Solutions were tested for dependence on the grid spacing by trialing grids that had both a higher and lower resolution than the grid outlined above. The chosen grid provided the best compromise between solution accuracy and computational running time. To quantify this statement, figure 6.2 shows the vertical volume transport per unit width (m^2/s) as a function of the number of nodes in the grid. The value of the vertical volume transport quickly rises for lower resolved grids (i.e. less nodes) but tends to level out between the two highest resolved grids. This trend was also discovered when comparing the vertical and horizontal velocity fields from each different grid resolution run, to the circulation observed in the laboratory. The two highest resolved grids had circulation's that were almost identical and which also matched with the circulation observed in the laboratory experiments. Whereas the lower resolved grids showed a circulation that was quite different to that observed in the laboratory.

A final series of six numerical simulations obtained after testing are presented in this chapter. Table 6.1 shows the parameters examined in this series of experiments. The Rayleigh and Prandtl numbers match the range achieved in the laboratory. All boundaries had a no slip condition, and the top and endwalls were all perfectly insulating. The bottom boundary applied flux and thermal conditions for the first four runs were chosen to match four of the laboratory experiments from chapter 5, with heat flux ratios chosen to span the three regimes defined there. Run 5 is an extension of the laboratory experiments to $|R_Q| = 1$. All the flux is applied to the

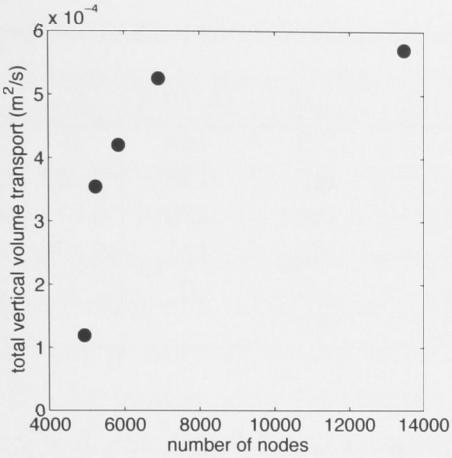

Figure 6.2: One hourly average of the total vertical volume transport per unit width (m^2/s) as a function of grid resolution. The grid used in the final experiments contained 6916 nodes.

left quarter of the base and none to the right quarter, resulting in an overturning circulation containing just one plume. Run 5 is used to test the scaling prediction of Hughes & Griffiths (2008) relating the stream functions of horizontal convection with one and multiple plumes, presented in this thesis as equations 2.14 and 2.15. The bottom boundary condition for runs $1-5$ is 16°C for $0.25 \leqslant x/L \leqslant 0.75$ and an applied constant flux either side of this region. Run 6 is used to compare our results directly with the study of Mullarney *et al.* (2004). As such, we use the same bottom boundary condition of 16°C applied to the right half of the base and a constant flux of 280 W applied to the left half of the base. The only difference is the exclusion of a non-conducting spacer that separated the flux and constant applied temperature regions in the experiments of Mullarney *et al.* (2004). This bottom boundary condition results in an overturning circulation containing just one plume, which is driven by the same total heat flux as applied in runs $1-5$. While our definition of heat flux ratio is not valid for boundary conditions in run 6, we will want to compare runs 5 and 6 and for this purpose run 6 will be plotted at $R_Q = 1$.

The steady state conditions from the laboratory experiments were used to initialize runs 1 and 4. Specifically, $\rho = 994.74\,\mathrm{kg/m^3}$, $\alpha = 3.282 \times 10^{-4}\,\mathrm{K^{-1}}$, $\nu = 7.535 \times 10^{-7}\,\mathrm{m^2/s}$, $\kappa = 1.477 \times 10^{-7}\,\mathrm{m^2/s}$ and $C_P = 4177.54\,\mathrm{Jkg^{-1}K^{-1}}$, giving a Rayleigh number of 3.5×10^{14} for all runs. All water properties were evaluated at the laboratory interior steady state temperature from experiments 2 - 16, which was 33°C. In the laboratory experiments the interior steady state temperature did not vary significantly over the small R_Q range we tested. The time-averaged solution

Table 6.1: Parameters explored in the numerical experiments.

Run	H_{total} (W)	H_1 (W)	H_2 (W)	$\lvert R_Q \rvert$	Ra	Pr
1	280	140	140	0	3.46×10^{14}	5.1
2	280	142	138	0.014	3.46×10^{14}	5.1
3	280	150	130	0.071	3.46×10^{14}	5.1
4	280	165	115	0.179	3.46×10^{14}	5.1
5	280	280	0	1	3.46×10^{14}	5.1
6	280	280	-	-	3.41×10^{14}	5.1

from run 1 was used to initialise the remaining runs and the flow was allowed to re-equilibrate to new boundary conditions by stepping in time. The time step used for the duration of each run was 0.25 s. The approach to thermal equilibrium was monitored using the time series of flux through the cooled part of the base. The flow was judged to be in equilibrium once the flux into the domain matched the flux leaving the domain to within 0.5%.

6.2 Results and discussion

In this section we present the time-averaged fields of stream function, horizontal velocity, vertical velocity and temperature for runs 1 through 5. The averaging time was five hours. The instantaneous flow fields for run 1 are also included. For runs 1, 4 and 5 we present the horizontal velocity profiles from three locations along the box and the vertical temperature profiles from five locations along the box. To test our results against previous work we compare the flow fields from run 5 and run 6 with the results of Mullarney *et al.* (2004). We also measure the confluence point and the interior stratification of each run to make comparisons with the laboratory data. Finally we test the scaling prediction of Hughes & Griffiths (2008) relating the stream functions of horizontal convection with one and multiple plumes, using runs 1 and 5.

There was substantial continuing variability in the flow fields after thermal equilibrium was reached. Therefore we obtained the mean flow fields by averaging over 3600 instantaneous data fields, spaced five seconds apart, to give a five hour average. The mean contour plots of stream function, horizontal velocity, vertical velocity and temperature are shown in figures 6.3, 6.4, 6.5 and 6.6, respectively, for runs 1 through 5. The lower boundary condition establishes a horizontal temperature gradient that drives fluid in the bottom boundary layer towards one of the endwalls. Near the endwall fluid in the thermal boundary layer gains enough buoyancy to rise

through the stable stratification, creating an endwall plume. Depending on the heat flux ratio, $|R_Q|$, both endwall plumes may reach the upper boundary, or the weaker plume intrudes beneath the outflow from the stronger plume (as for the laboratory experiments). The dominance of one plume over the other as the heat flux ratio is increased from $|R_Q| = 0$ to 0.179 is clear in the stream function, horizontal velocity and vertical velocity plots. The two oppositely signed overturning cells, in figure 6.3, are each associated with an endwall plume. They become more asymmetric as $|R_Q|$ is increased and the negative cell dominates (reaches along the entire box length) once $|R_Q| \geq 0.179$. Similarly, the outflow from the stronger plume travels further horizontally as $|R_Q|$ is increased (horizontal velocity, figure 6.4, vertical velocity, figure 6.5). In all runs the outflow from plumes penetrating the full depth is almost half the box depth, which is a little greater than that observed in the laboratory experiments. Runs 1, 4 and 5 show a horizontal antisymmetry about $z \sim 0.5$ in the horizontal velocity plots.

The vertical velocity plots (figure 6.5) reveal the presence of a weak downwelling region beside each of the rising endwall plumes. A corresponding mean recirculation cell is present in figures 6.3 and 6.4, which increases in strength as $|R_Q|$ is increased. This effect is revealed by the appearance of regions near the upper boundary at $x = 0.3\,\mathrm{m}$ of oppositely signed stream function and horizontal velocity, and by a downward deflection of the isotherms near $x = 0.2\,\mathrm{m}$. In the laboratory one also sees this wave-like, standing feature for much of the time.

Animations of the flow showed the evolution of coherent motion in time. Figure 6.7 shows a sequence of fourteen instantaneous horizontal velocity plots spaced at 2.5 minute intervals, thus covering 32.5 minutes of flow time. The striking coherent motions observed in the animations are also visible in these plots. In the centre region of the first plot a diagonal band of negative horizontal velocity is visible. In the next three plots this band moves closer to the right endwall and a diagonal band of positive horizontal velocities is present in the centre region. This band is present for about three frames, during which time it moves towards the left endwall, before being replaced by a diagonal band of negative horizontal velocity. This cycle continues throughout the sequence in figure 6.7. The end regions of the box also show periodic coherence. In the second frame we see a band of negative horizontal velocity extending at an angle from the top right corner towards the centre at the base of the box. This band is present for the next three frames after which it appears to be modified by interaction with the band moving to the right from the centre, as described above. After this interaction the band in the top right corner is re-established. A similar cycle is visible for a band of positive velocities extending

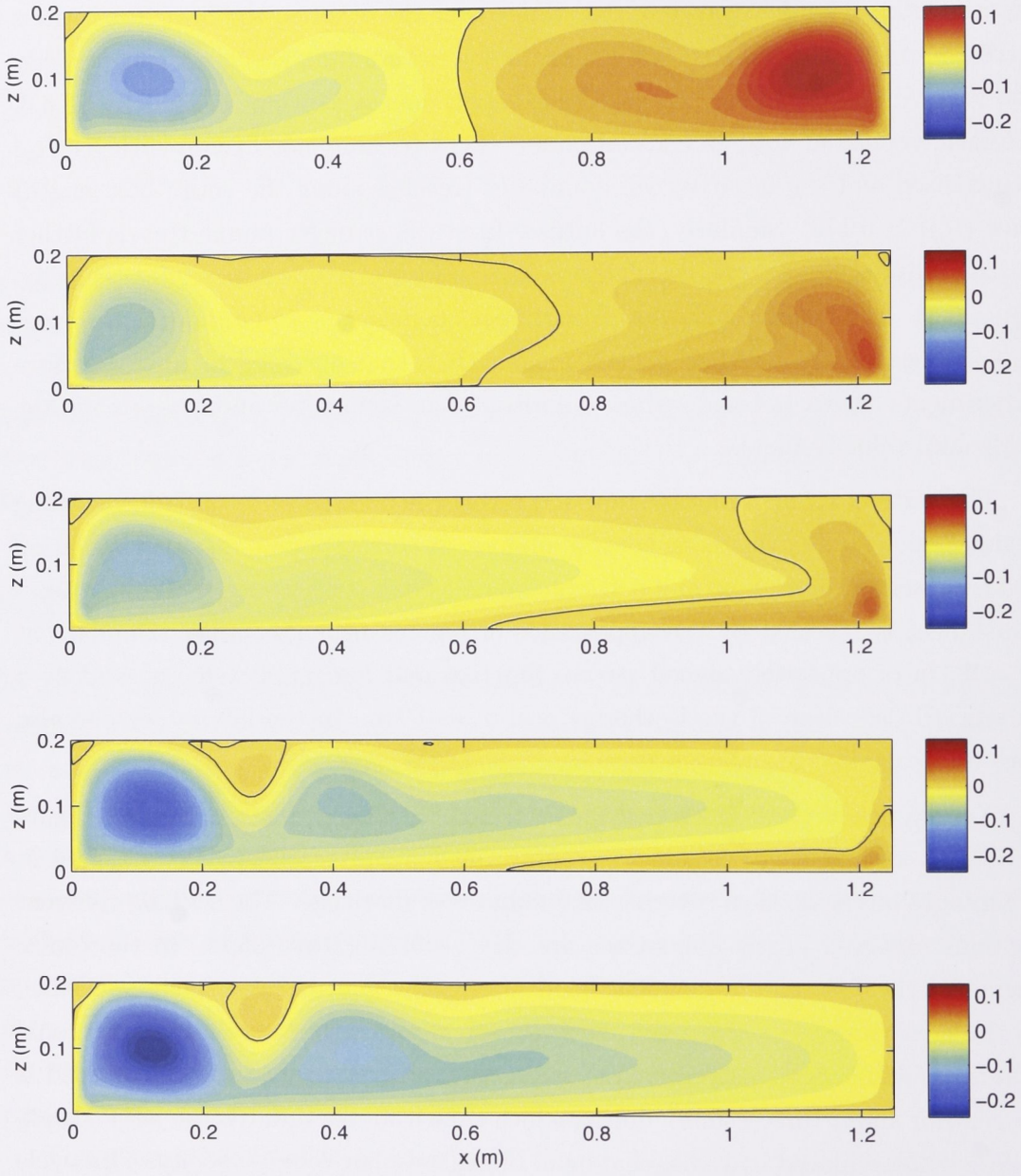

Figure 6.3: Time-averaged stream function (kg/ms) over five hours of flow time for (from top to bottom) run 1, $|R_Q| = 0$, run 2, $|R_Q| = 0.014$, run 3, $|R_Q| = 0.071$, run 4, $|R_Q| = 0.179$ and run 5, $|R_Q| = 1$. The solid line is the zero contour.

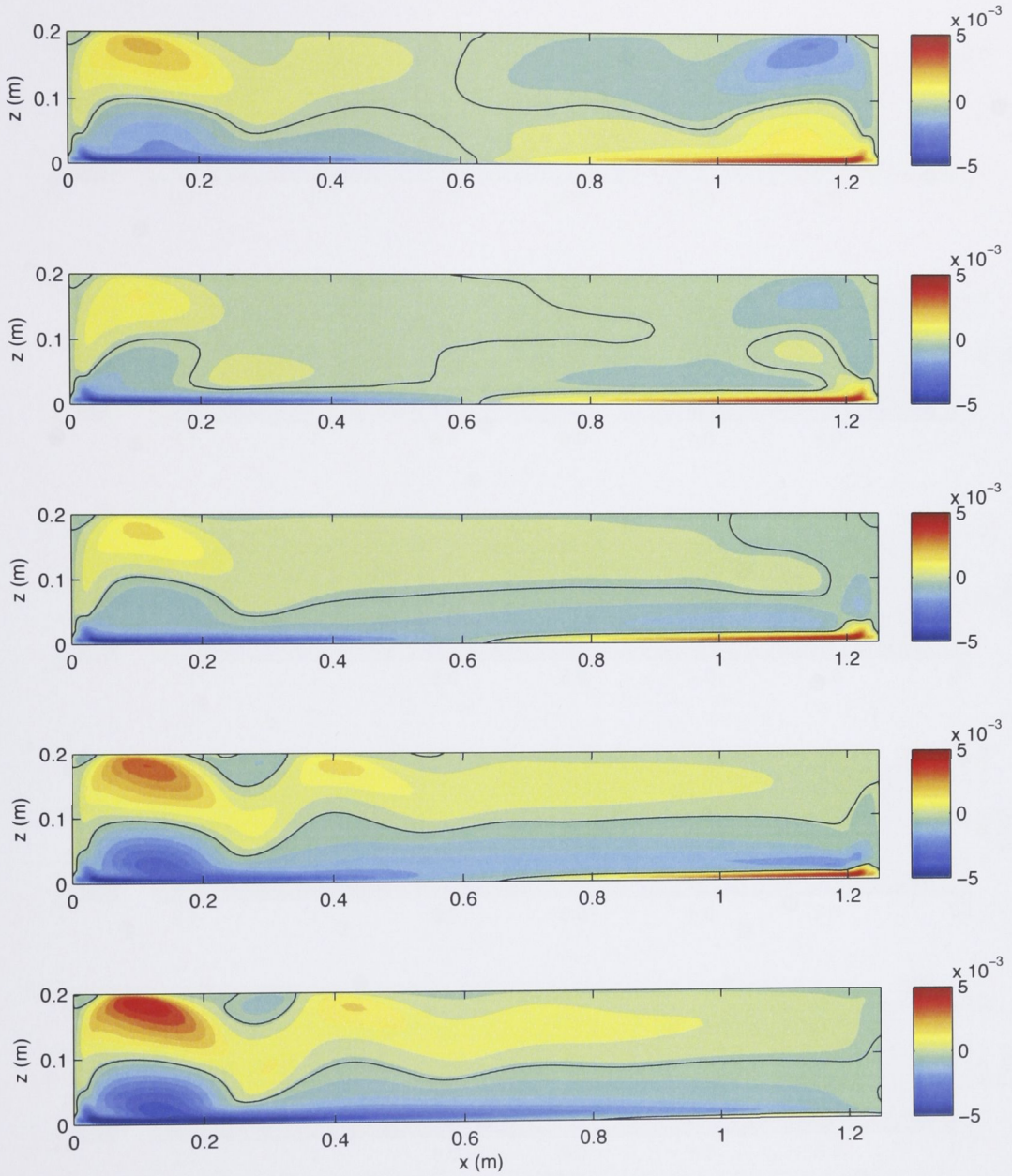

Figure 6.4: Time-averaged horizontal velocity (m/s) over five hours of flow time for (from top to bottom) run 1 $|R_Q| = 0$, run 2 $|R_Q| = 0.014$, run 3 $|R_Q| = 0.071$, run 4 $|R_Q| = 0.179$ and run 5 $|R_Q| = 1$. The solid line is the zero contour.

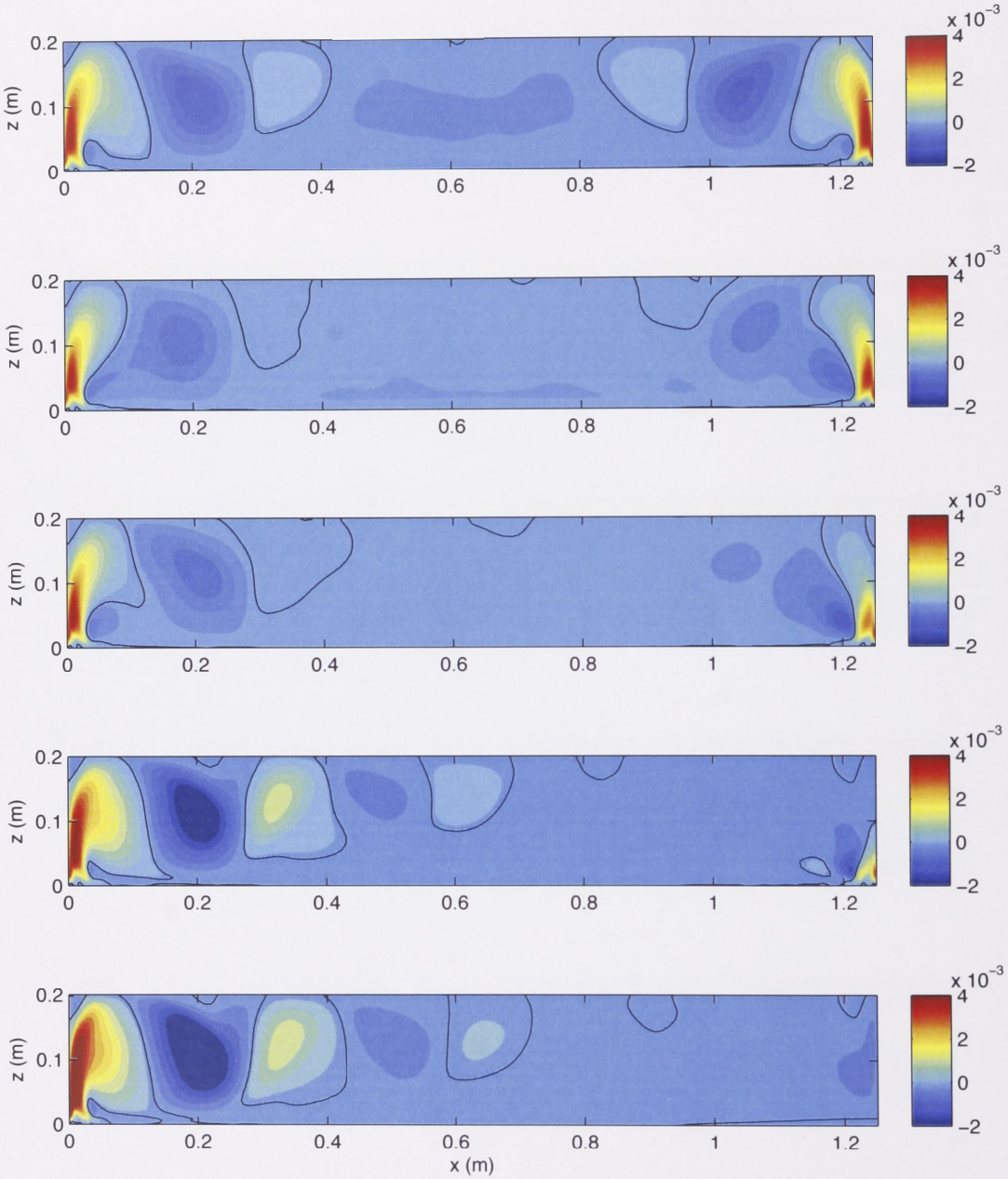

Figure 6.5: Time-averaged vertical velocity (m/s) over five hours for (from top to bottom) run 1 $|R_Q| = 0$, run 2 $|R_Q| = 0.014$, run 3 $|R_Q| = 0.071$, run 4 $|R_Q| = 0.179$ and run 5 $|R_Q| = 1$. The solid line is the zero contour.

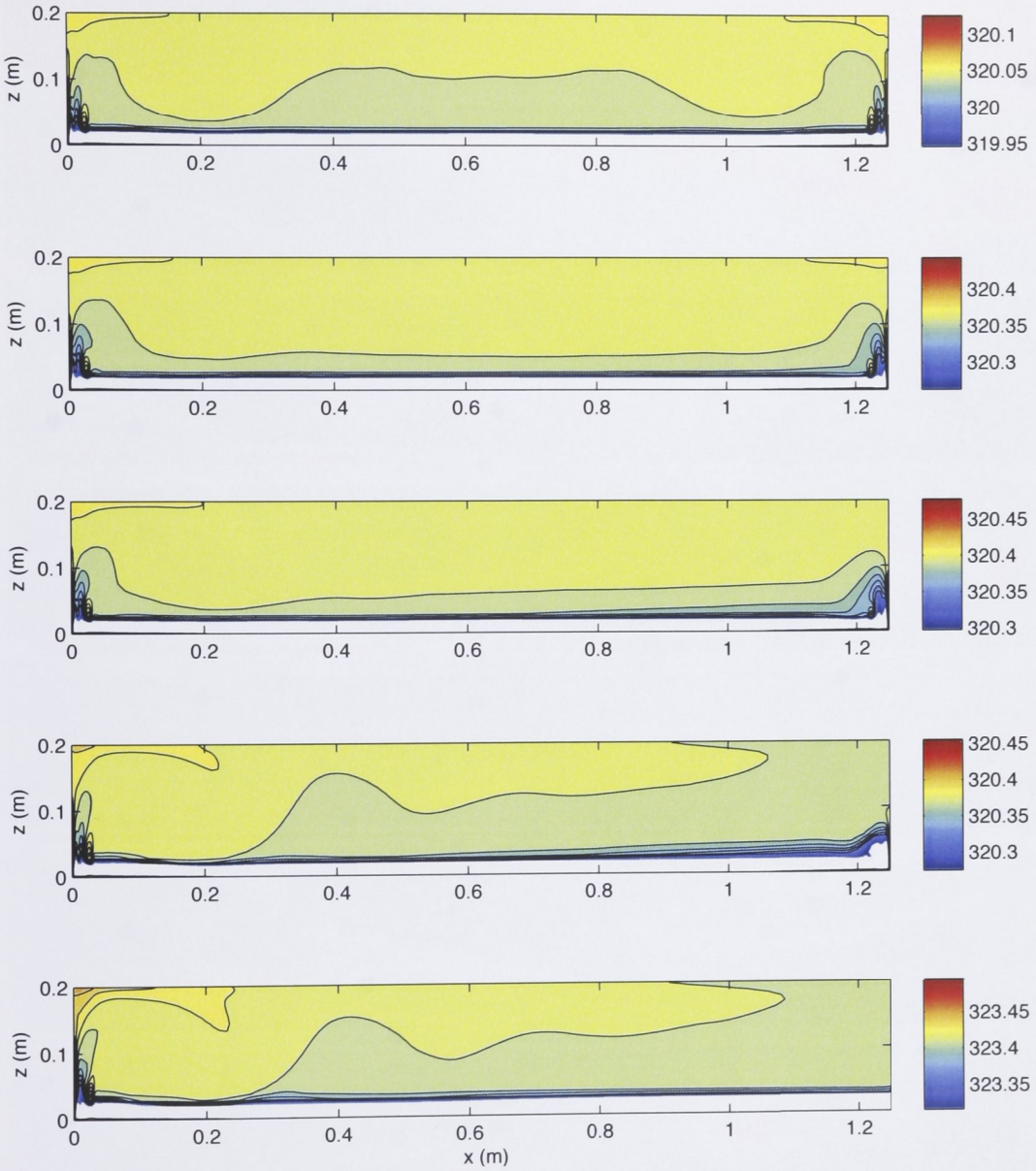

Figure 6.6: Time-averaged temperature (K) over five hours for (from top to bottom) run 1 $|R_Q| = 0$, run 2 $|R_Q| = 0.014$, run 3 $|R_Q| = 0.071$, run 4 $|R_Q| = 0.179$ and run 5 $|R_Q| = 1$. The black contour lines are 0.01° apart. The thermal boundary layer is unresolved.

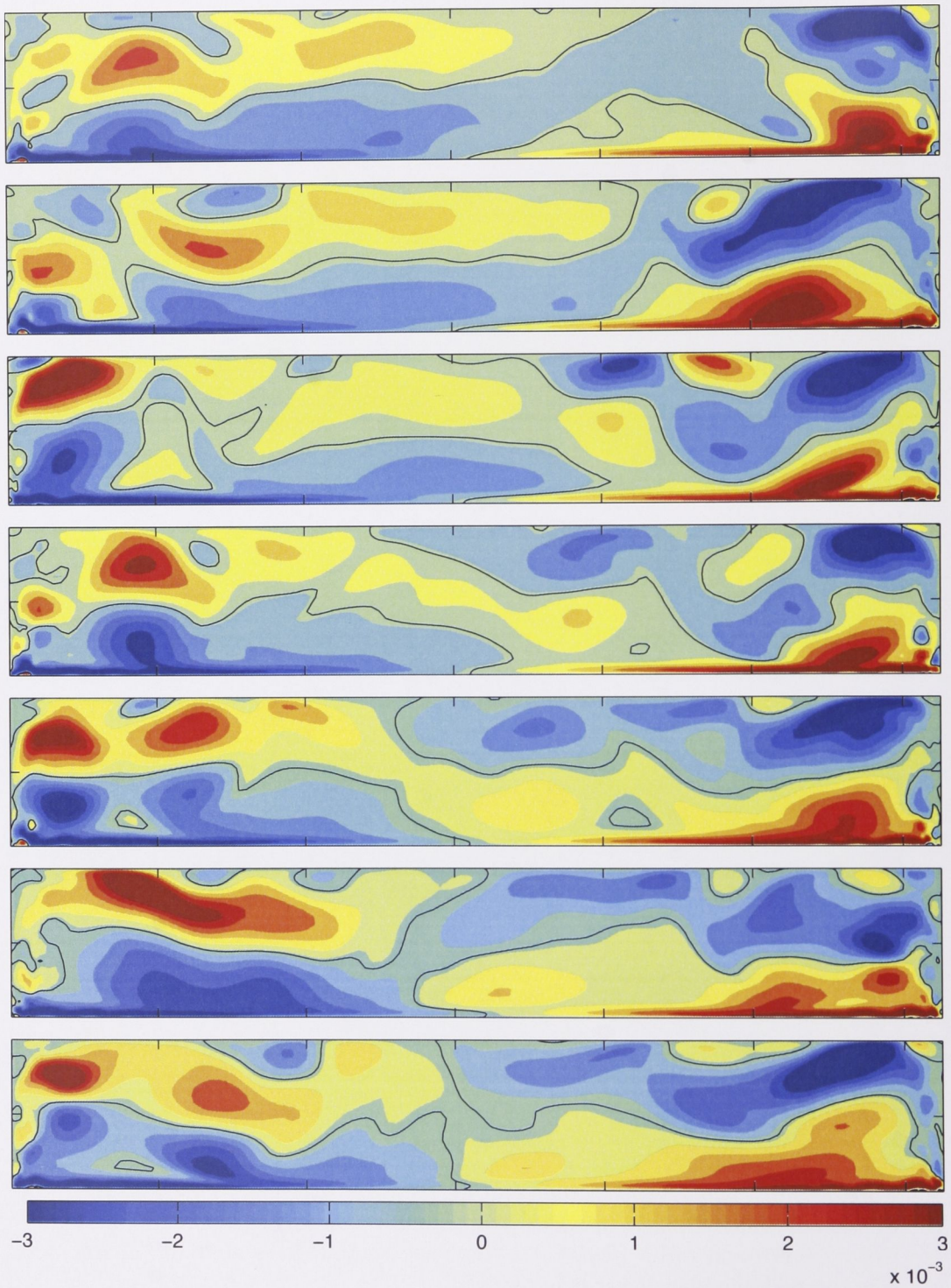

Figure 6.7: Time sequence of the horizontal velocity (m/s) for run 1. The time difference between each frame is 2.5 minutes. Continued on next page.

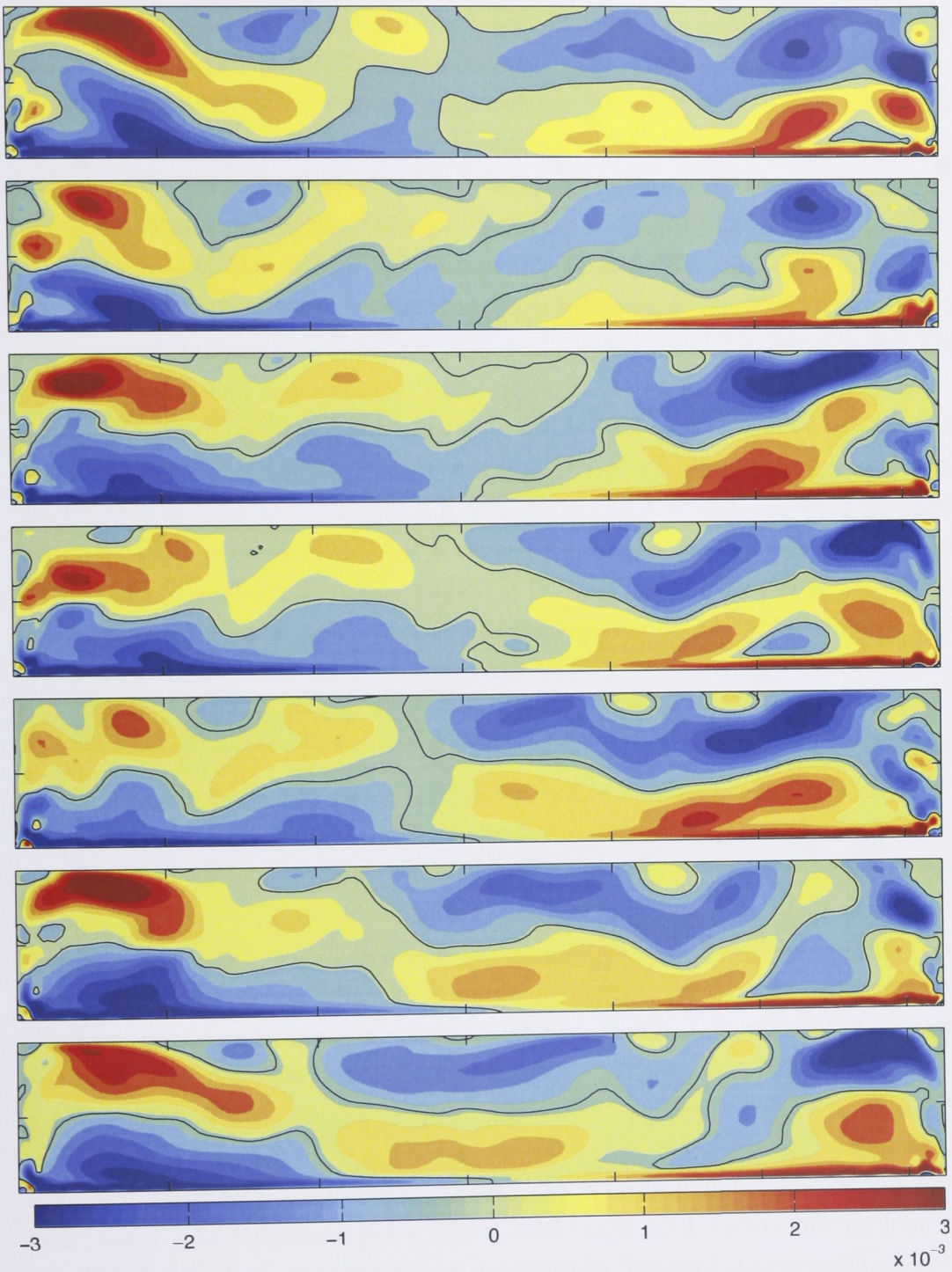

Figure 6.7: Time sequence of the horizontal velocity (m/s) for run 1. The time difference between each frame is 2.5 minutes. Continued from previous page.

downwards towards the box centre from the top left hand corner. These coherent motions in the opposite corners at the top of the box appear to be out of phase with each other. The mechanism for this coherence in the flow was found to be internal wave propagation, and this is discussed in detail in section 6.3. Eddies are also apparent in the time sequence of horizontal velocities as blobs of positive or negative velocities that propagate to the right or left, respectively. Animation of the vertical velocity field (not shown) reveals the unsteady behaviour of the rising plumes. For run 1 each plume generally reaches through the full tank depth. However detrainment sometimes occurs at shallower depths. The plumes are turbulent (in so much as a two dimensional flow is turbulent) and entrainment is still important.

In figure 6.8 we show for run 1 examples of instantaneous flow fields of stream function, horizontal velocity, vertical velocity and temperature. Upon comparison with the average fields in figures 6.3, 6.4, 6.5 and 6.6 the amount of variability that exists in the flow is striking. The variability involves, in part, the eddies and the movement of the confluence point. A train of alternately signed velocity perturbations is visible in the thermal boundary region at the base of the vertical velocity plot (figure 6.8). This is analogous to the convective mixed layer we observed in the laboratory experiments, but is forced to be two dimensional in the numerics. The instantaneous plots for $|R_Q| \neq 0$ are ostensibly similar to those for $|R_Q| = 0$ shown in figure 6.8.

To highlight the amount of variability in the flow we also show in figure 6.9 for run 1, the anomalous stream function, horizontal and vertical velocity and temperature contour plots. These were simply obtained by finding the difference between the time-averaged field and the instantaneous field shown in figure 6.8. The magnitude of the stream function and velocity anomalies are comparable with the time-average values throughout much of the flow. Figure 6.9*a* and *c* show, respectively, the stream function and vertical velocity anomalies to be predominantly vertically aligned whereas the horizontal velocity contour plot, figure 6.9*b*, has anomalous structure extending lengthwise through the tank. The vertical velocity perturbations at the base of the vertical velocity plot (figure 6.9*c*) are seen to be coupled with similar perturbations in horizontal velocity (figure 6.9*b*). The variability in the anomalous temperature field, figure 6.9*d*, is only a few hundredths of a degree, however the time-averaged vertical temperature gradient is at most one hundredth of a degree, so the magnitude of the temperature anomalies is significant. Additionally, the convective mixed layer is visible in all subfigures of figure 6.9.

The bottom boundary condition of run 5 and 6 is such that each produces a single full depth plume which drives a large scale overturning circulation. As outlined in

section 6.1 there are slight differences in the structure of the bottom boundary condition between these two runs. The following comparison is required to understand the extent to which the circulation is changed using each of these slightly different boundary conditions. Figures 6.10, 6.11, 6.12 and 6.13 show the average flow fields for stream function, horizontal velocity, vertical velocity and temperature, respectively, for runs 5 and 6. The plots for runs 5 and 6 are striking in their similarity. In more detail, the overturning strength in run 5 is $\sim 5\%$ stronger and the velocities are slightly larger than run 6. The temperature structure throughout the interior is largely the same, although a difference arises in the horizontal gradient through the

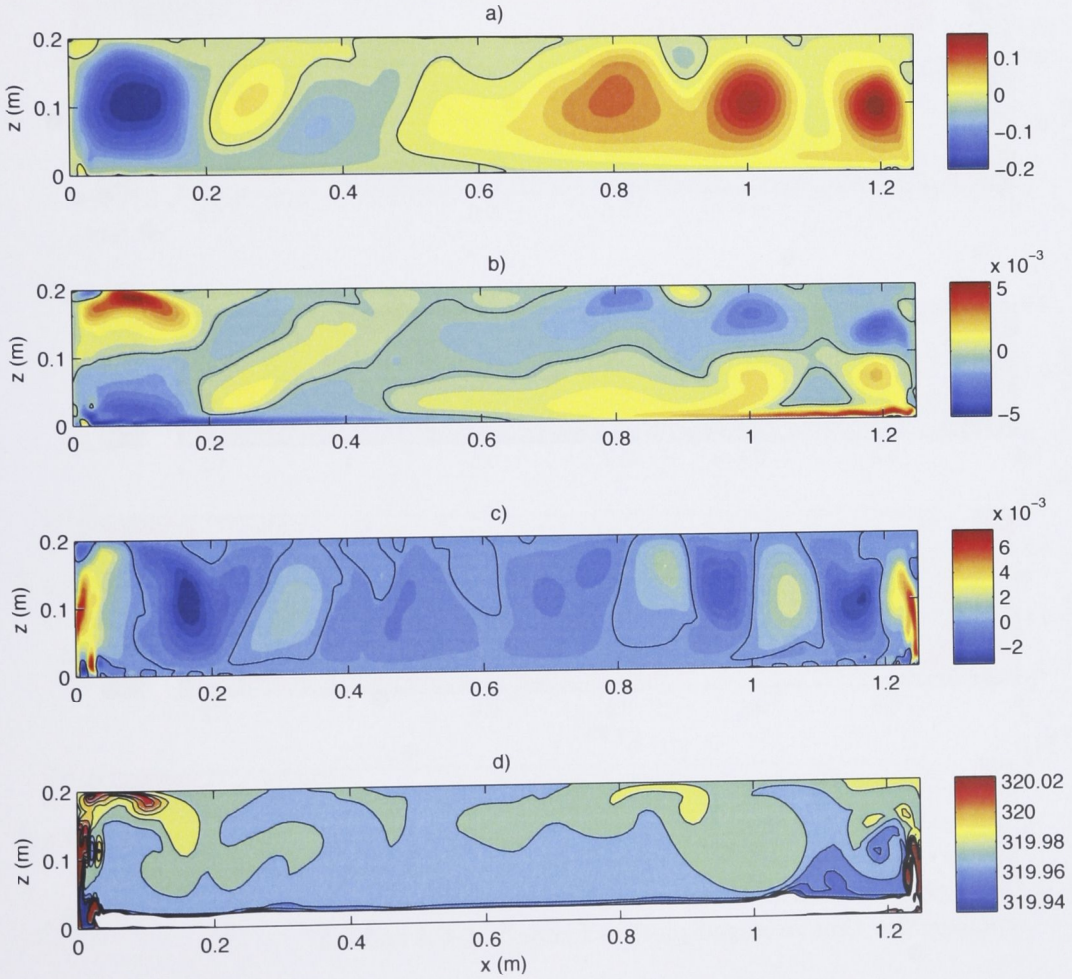

Figure 6.8: The instantaneous flow fields for the numerical experiment with $|R_Q| = 0$ a) stream function (kg/ms), b) horizontal velocity (m/s), c) vertical velocity (m/s) and d) temperature (K). In a), b) and c) the solid line indicates the zero contour line. In d) the black contour lines are 0.01° apart over the range 319.93 K to 320.03 K and the thermal boundary layer is unresolved.

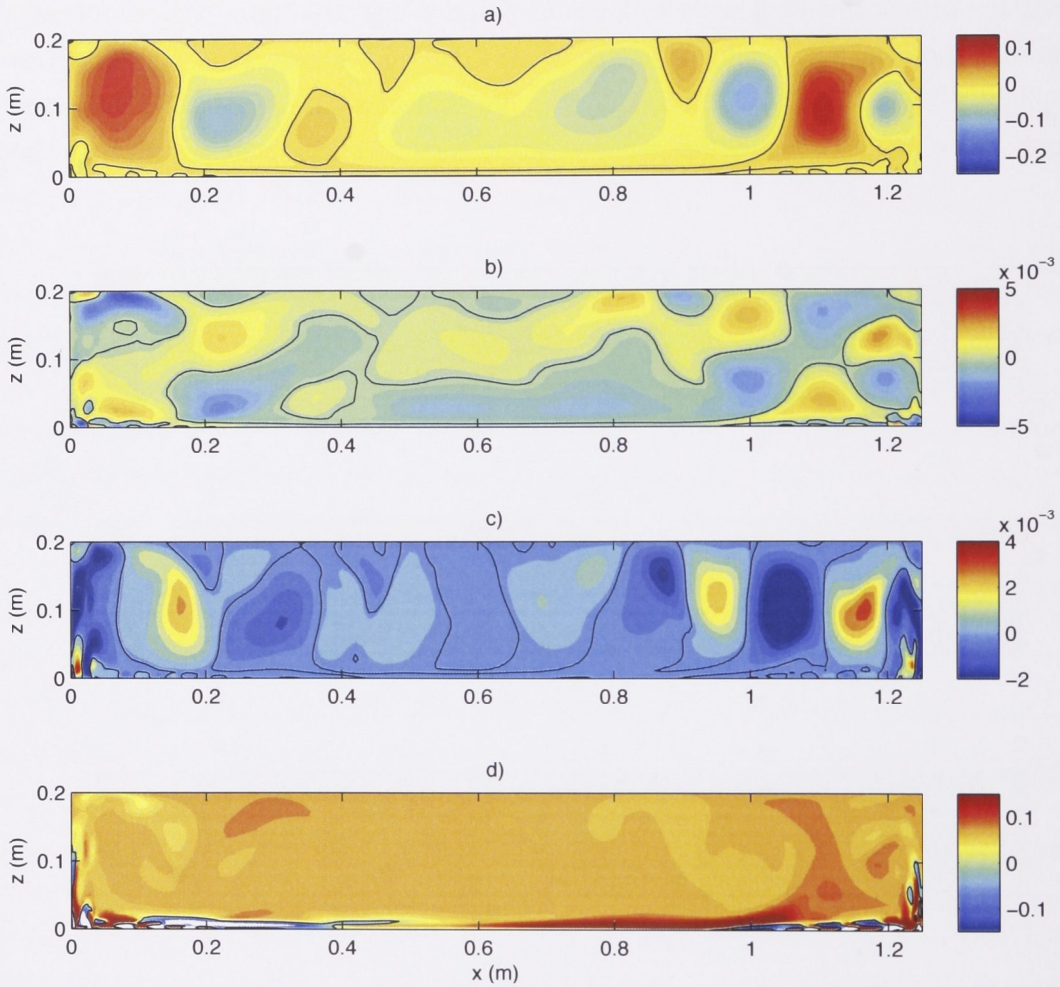

Figure 6.9: The anomalous flow fields for the numerical experiment with $|R_Q| = 0$ a) stream function (kg/ms), b) horizontal velocity (m/s), c) vertical velocity (m/s) and d) temperature (K). In all plots the solid line indicates the zero contour line. Plots a), b) and c) have the same colour scale as the comparative time averaged plots in figures 6.3, 6.4 and 6.5.

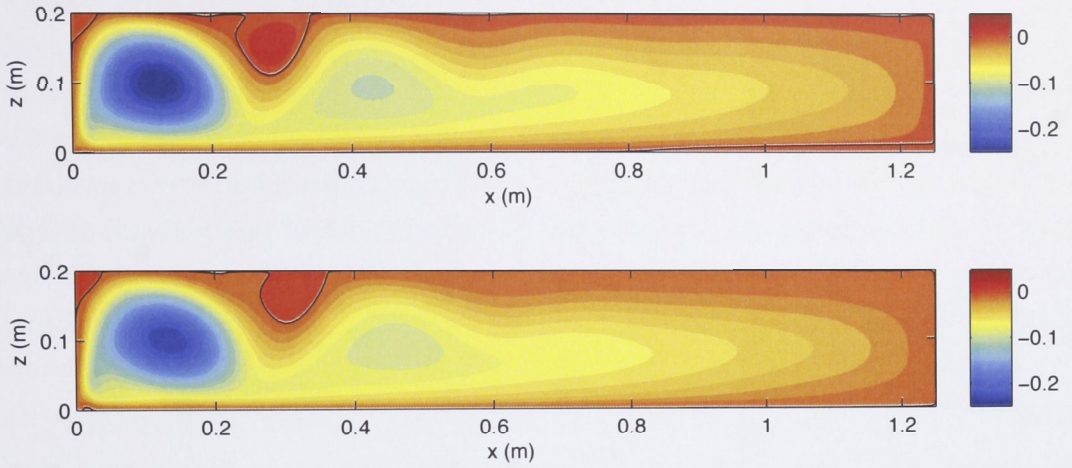

Figure 6.10: Time-averaged stream function (kg/ms) over five hours of flow time for (from top to bottom) run 5 and run 6. The solid line is the zero contour.

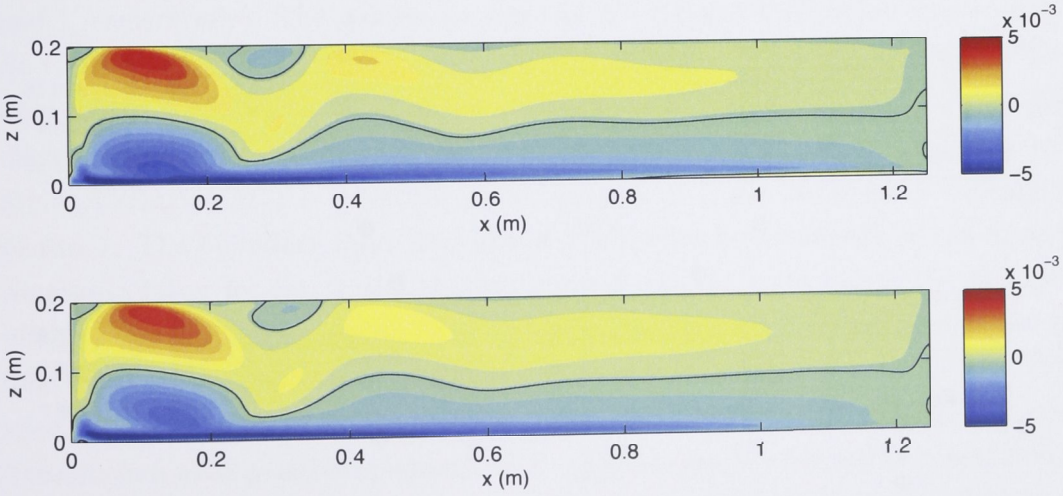

Figure 6.11: Time-averaged horizontal velocity (m/s) over five hours of flow time for (from top to bottom) run 5 and run 6. The solid line is the zero contour.

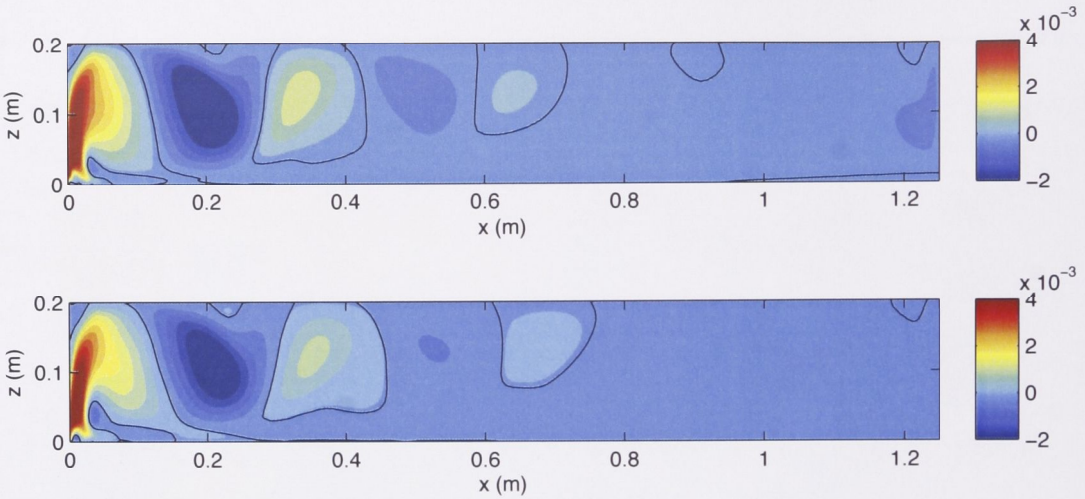

Figure 6.12: Time-averaged vertical velocity (m/s) over five hours of flow time for (from top to bottom) run 5 and run 6. The solid line is the zero contour.

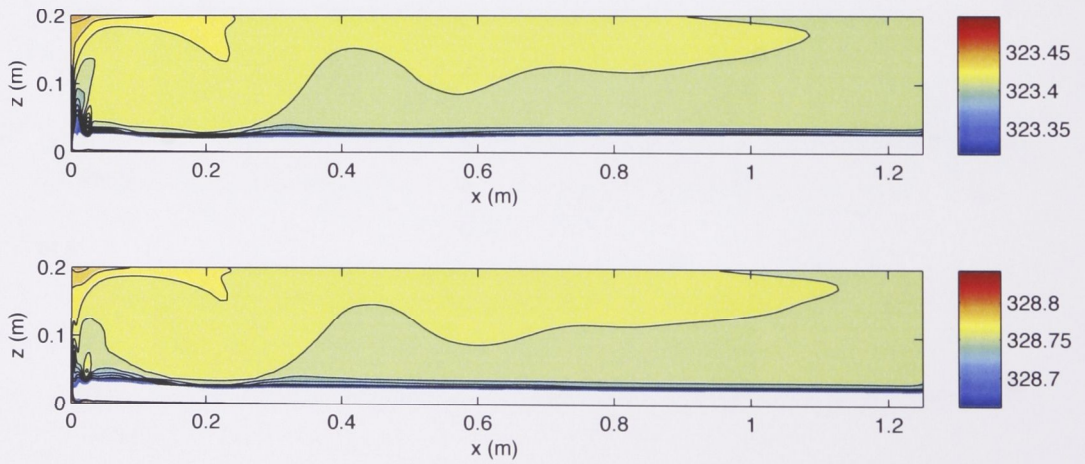

Figure 6.13: Time-averaged temperature (K) over five hours of flow time for (from top to bottom) run 5 and run 6. The black contour lines are 0.01° apart.

thermal boundary layer. In run 5 there is no flux coming through the right quarter of the base so the dense water from above the cold plate spreads towards $x = L$ without being cooled from below, i.e. it is only being affected by diffusion of heat from above. In contrast the boundary condition across the right half of the base in run 6 is the constant applied temperature, and so fluid is continually cooled for $0.5 < x/L < 1$ and advected towards the heated region of the base. This difference produces a very small region near the bottom right boundary of the box where the stream function and horizontal and vertical velocity are positive, and the vertical temperature gradient through the boundary layer is weakened. Therefore, there are small differences in the details of the flow fields, but the bottom boundary conditions in runs 5 and 6 give rise to similar large scale circulations.

A comparison between these results and those from Mullarney *et al.* (2004) reveals an overall consistency of the flow fields. Mullarney *et al.* (2004) reported a small and shallow intrusion from the base of the rising plume which was not observed at the steady state in either run 5 or 6. However, we had a finer grid resolution along all the boundaries and also set a more stringent criterion for thermal equilibrium, i.e. the mismatch between input and output flux was less than 0.5% (of the total heat flux) for our runs, whereas it was less than 3% for Mullarney *et al.* (2004).

Figure 6.14 shows the vertical profile of the horizontal velocity, u, at three locations along the box, $x = 0.1,\ 0.625$ and $1.125\,\mathrm{m}$ for runs 1, 4 and 5 ($R_Q = 0, 0.179$ and 1, respectively). The profiles for run 1 at $x = 0.1$ and $1.125\,\mathrm{m}$ are antisymmetric to each other. Each profile shows the plume outflow towards the centre of the domain and the much stronger and thinner bottom boundary layer flow towards the closest endwall. In contrast, the profiles for run 4 and 5 at $x = 0.1$ and $1.125\,\mathrm{m}$ are asymmetric. At $x = 0.1\,\mathrm{m}$ the plume outflow ($z \gtrsim 0.09\,\mathrm{m}$) is faster compared to run 1. The boundary layer flow in run 4 is similar in magnitude to run 1, and somewhat faster for run 5, and the entrainment into the lower half of the stronger plume is greater for increasing $|R_Q|$. At $x = 1.125\,\mathrm{m}$ in run 4, the weaker plume forms an intrusion towards the middle of the box at depths $0.02 < z < 0.04\,\mathrm{m}$. The effect of the zero flux boundary condition along the right quarter of the box for run 5 results in a weak positive maximum at $z \sim 0.005\,m$ and a weak negative maximum at $z \sim 0.01$, due to conservation of mass. The run 1 profile in the centre of the box shows almost stationary fluid, due to the centrally located confluence of the two full depth plumes. The corresponding profile for run 4 and 5 shows the dominance of the single full depth plume. The flow near the top of the box is positive, towards the opposite endwall, and the bottom boundary layer flow is negative, because it is drawn towards the stronger plume.

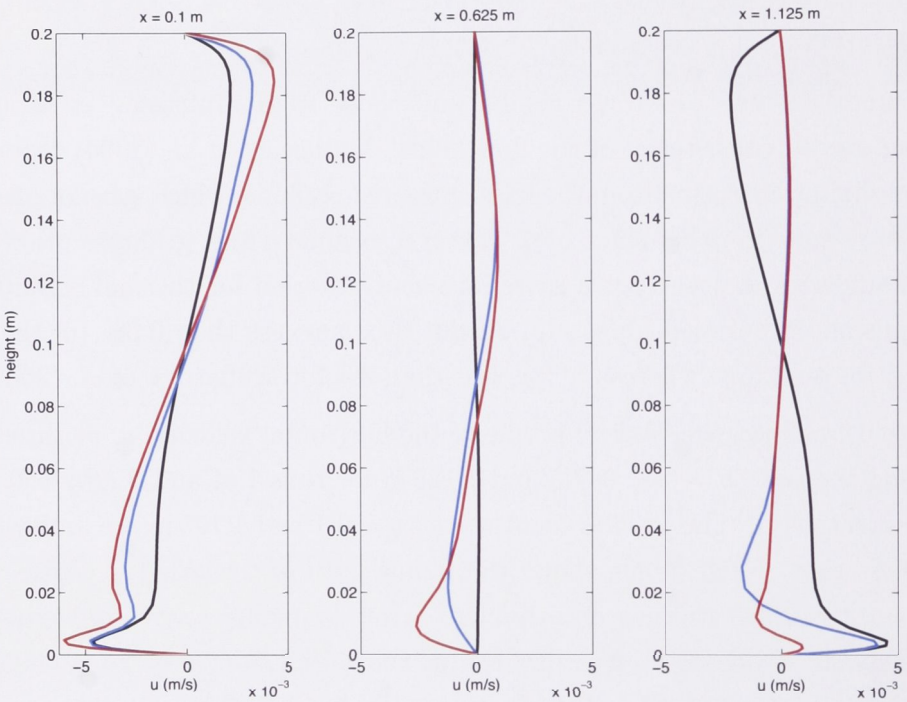

Figure 6.14: Horizontal velocity profiles from three locations along the tank for Runs 1, 4 and 5. Black, $|R_Q| = 0$, blue, $|R_Q| = 0.179$ and red, $|R_Q| = 1$.

The horizontal location of the confluence of the two plumes was measured using the averaged horizontal velocity data set. Figure 6.15 compares the confluence point data from the laboratory experiments with that from the numerical experiments. The agreement is excellent, the numerical data lies within the scatter of the experimental data. Our small set of numerical runs means we had limited capacity to add to figure 5.7, which showed the change of normalized weaker plume penetration depth with R_Q. Using figure 6.5 we can measure the penetration depth of the weaker plume and find, not surprisingly, that for runs 1 through 3 $z_{weak}/D = 1$ and for runs 5 and 6 $z_{weak}/D = 0$. Run 4 is the only experiment that has an intruding weaker plume, with $z_{weak}/D = 0.5$. This value is slightly larger than that found in the laboratory for the same R_Q, though it is in the range of laboratory values measured for $0.1 < |R_Q| < 0.2$. It should be remembered that the measurement of the confluence point and z_{weak} is from the time averaged plots. Animation of the horizontal velocity flow field reveals variability in the location of the confluence point as each unsteady plume ejects eddies and intermittently extends in the horizontal direction. Similarly, animation of the vertical velocity flow field reveals variation of the weaker plume's penetration height as it intermittently tries to punch its way through the stable interior stratification. The numerical results for x_c and z_{weak} confirm the laboratory results and serve to re-enforce the fact that a small change ($\sim 10\%$) from equally forced plumes ($R_Q = 0$) leaves the stronger plume in control of the circulation.

Figure 6.16 shows the normalised vertical temperature profiles at five locations along the domain, for runs 1, 4 and 5. The data were normalised by subtracting the temperature of the cold plate from the measured temperature and dividing by $\overline{T_{1/2} - T_c}$, which is the time averaged temperature difference between $z/D = 0.5$ and 0, for run 1 (use of $T_{1/2}$ here was to avoid use of the temperature at the top boundary in the laboratory experiments, where it can be contaminated by localised heat loss through holes in the lid). The data for runs 1 and 4 approximately overlay at all positions along the box and we can distinguish only one curve from these runs. Data from run 5 also overlays that from runs 1 and 4 for $x = 0.10, 0.30$ and 0.625 m, but the significant dependence on R_Q is apparent for $x = 0.95$ and 1.15 m. Runs 1 and 4 have an approximately mirror symmetric temperature field about the centre, contrasting with run 5 which is asymmetric. At $x = 0.625$ m the boundary layer is, in general, at its most stably stratified. In runs 1 and 4 the heating of the boundary layer fluid as it moves away from the centre, towards $x = 0.1$ and 1.15 m, respectively, results in convective mixing and significant erosion of the previously stable stratification. This is also true in the left half of the box in run 5, however, since no heating occurs

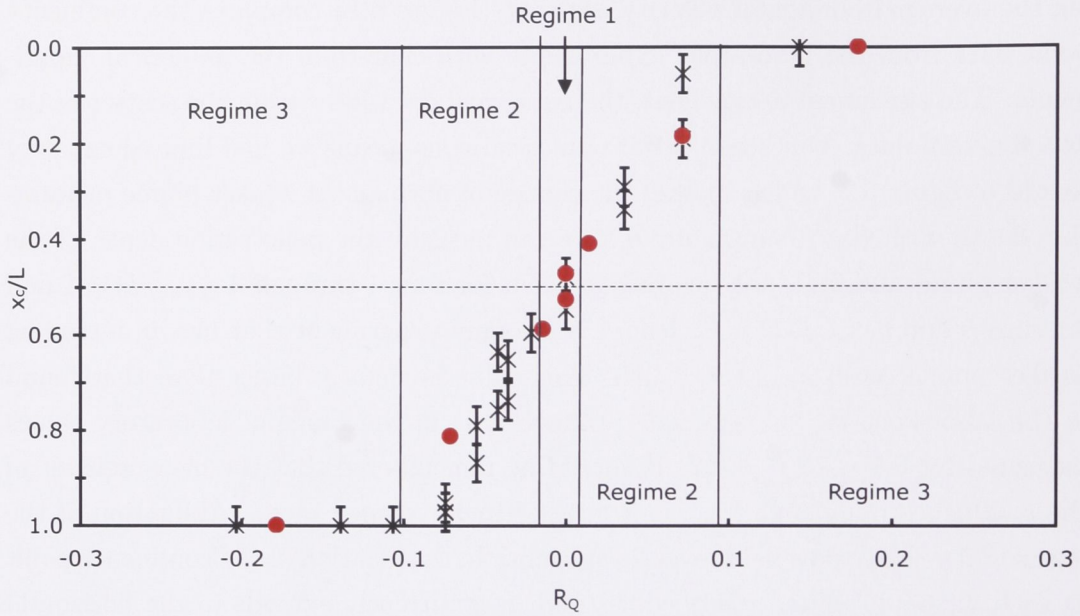

Figure 6.15: Normalised confluence point, x_c/L of the two full depth plumes. ($\times$) is the experimental data from chapter 5, ($\bullet$) is the numerical data.

over the right quarter of the base the dense fluid spreads towards $x = 1.15\,\mathrm{m}$ without being heated from below. There is, however, diffusive heating from above, which reduces the vertical temperature gradient through the bottom boundary layer in the right half of the box leaving the largest vertical gradients in the thermal boundary layer occurring at $x = 0.625\,\mathrm{m}$. It is not clear at what value of R_Q the transition between approximately mirror symmetric vertical temperature profiles (runs 1 - 4) and asymmetric profiles (run 5) occurs. It is evident that it does not correspond to $|R_Q| \sim 0.1$, where we have found the position of the confluence point and the stratification to be determined by the dominant plume The assumption that the temperature structure is approximately independent of $|R_Q|$ is valid for small $|R_Q|$, which includes the range of the laboratory experiments and numerical runs 1 - 4.

Due to the strictly two dimensional nature of the numerical calculation there is less entrainment into the endwall plumes in comparison to the laboratory experiments. This results in the interior stratification being less than the laboratory equivalent, by a factor of approximately 20 (figure 6.17). Nevertheless, we find that the stratification increases by a factor of approximately two as $|R_Q|$ is increased from 0 to 0.179, which compares well with the corresponding laboratory experiments. To allow more detail to be visible in figure 6.17 we scale separately the laboratory and numerical results, such that the data from Mullarney *et al.* (2004) for $R_Q = 1$ (as

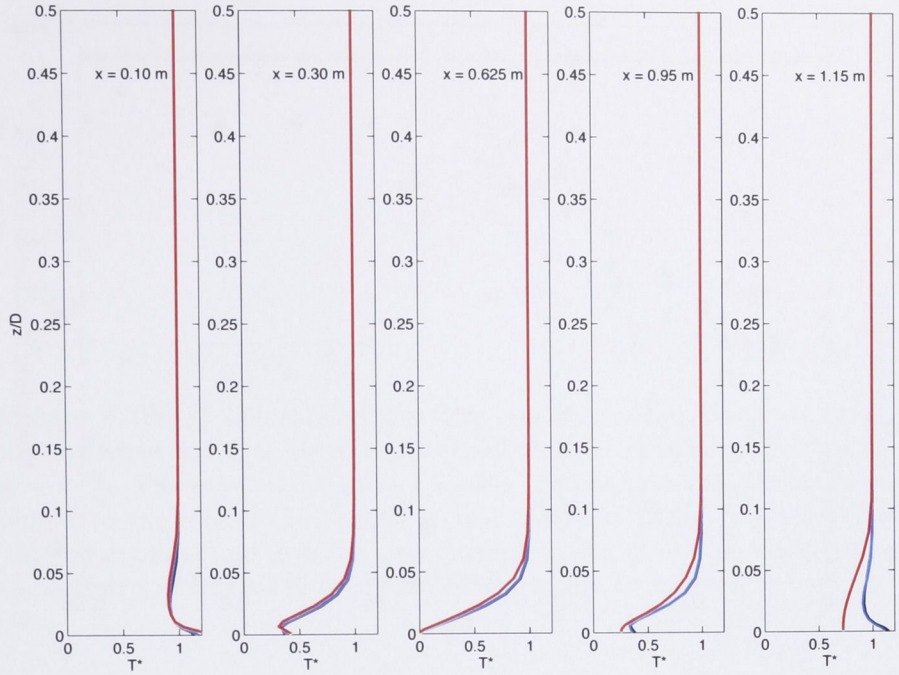

Figure 6.16: Normalised temperature profiles from runs 1, 4 and 5, at five locations along the tank, black, Run 1 $|R_Q| = 0$, blue, Run 4 $|R_Q| = 0.179$, and red, Run 5 $|R_Q| = 1$.

discussed in section 5.3) and the data from run 5 $|R_Q| = 1$ are coincident (shown by the horizontal solid lines). This suggests that above $|R_Q| \sim 0.2$ the stratification does not change with further increases of $|R_Q|$. Both the numerics and the laboratory experiments are consistent in this regard despite the large difference in stratification.

The stream function (per unit spanwise width) in the box ($\mathrm{kgs^{-1}m^{-1}}$) divided by the density gives the vertical volume transport (per unit spanwise width) in the box ($\mathrm{m^2s^{-1}}$). When two plumes are present ($n = 2$), the sum of the absolute value of the stream function maxima from each half of the box divided by the density gives the total vertical volume transport in the box, ψ_{total}.

Figure 6.18 shows the ratio of the vertical volume transport from the stronger plume, ψ_{sp}, to the total rate of vertical volume transport in the box, ψ_{total}, for each run. Not surprisingly, we see the data increasing from a ratio of about 0.5 when the plumes have equal strength, to 1 when all the flux is contained in one plume. For $|R_Q| > 0.2$, the total overturning continues to increase (albeit more gradually) by up to 20%. This is comparative to the increase in the stratification (figure 6.17)

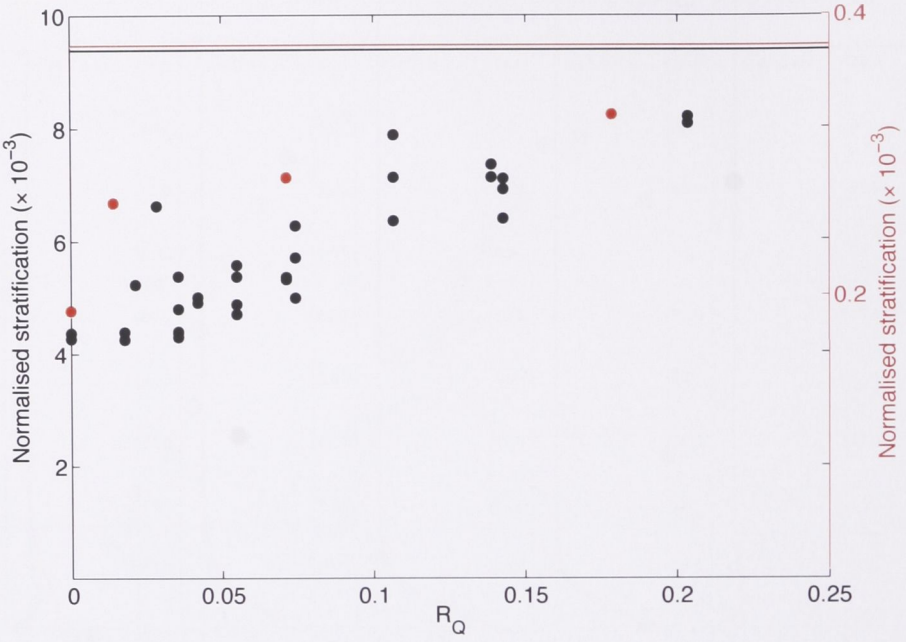

Figure 6.17: Comparison of the normalised stratification in the laboratory (black) and numerical (red) experiments. The scaled laboratory data from Mullarney *et al.* (2004) for $R_Q = 1$ and the data from Run 6 $|R_Q| = 1$ are represented by the black and red solid lines, respectively. To normalise the dimensional stratification we multiply by the tank depth, D, and divide by $(\Delta T_{1/2} - \Delta T_c)_{R_Q=0}$, the temperature difference between half depth and the cold plate for the $|R_Q| = 0$ experiments. Note the order of magnitude difference in the two vertical axis scales.

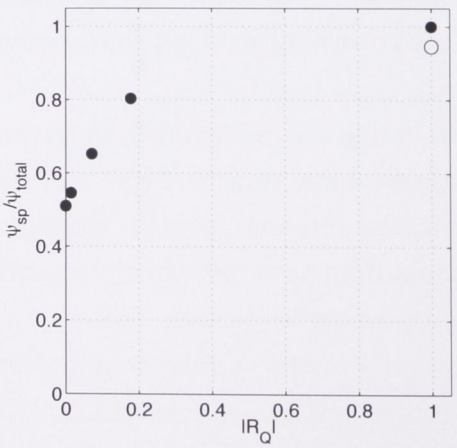

Figure 6.18: The ratio of the vertical volume transport from the stronger plume, ψ_{sp}/ρ_o, to the total rate of vertical volume transport in the box, ψ_{total}/ρ_o.

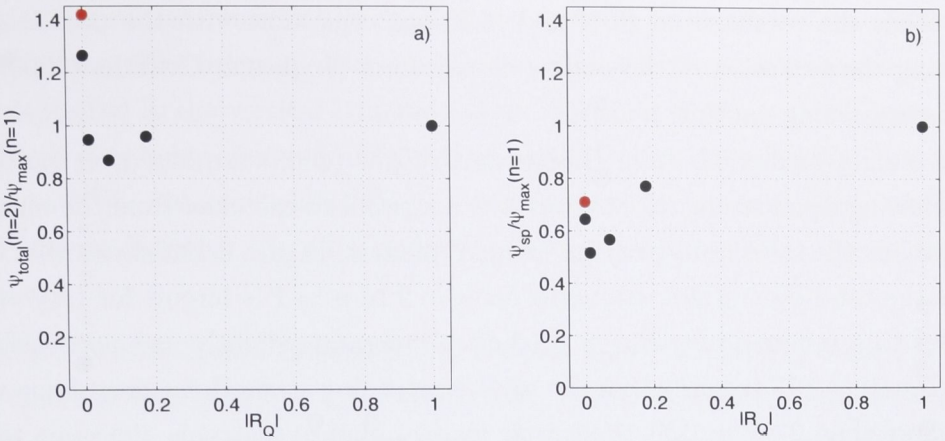

Figure 6.19: a) The ratio of the total rate of vertical volume transport in the box when $n = 2$, to the rate of vertical volume transport in the box when $n = 1$. b) The ratio of the rate of vertical volume transport in the stronger plume, to the rate of the vertical volume transport in the box when $n = 1$. The red dot in a) and b) is the upper bound prediction and scaling prediction, respectively, of Hughes & Griffiths (2008) for $|R_Q| = 0$.

between $|R_Q| = 0.2$ and 1. The open circle in figure 6.18 is the ratio of the vertical volume transport in run 6 compared to run 5.

Using the results from runs 1 and 5 we are able to test the scaling prediction of Hughes & Griffiths (2008) relating the stream functions of horizontal convection with one and multiple plumes. We note that even though the stratification in the numerical calculations is smaller than that measured in the laboratory (which may also imply a reduced stream function in the numerics) a comparison between two experiments in which entrainment is resolved in the same manner remains a valid way of testing the scaling prediction. The ratio of the average vertical volume transport from the two overturning cells in run 1, to the vertical volume transport of the single overturning cell from run 5, is

$$\frac{\overline{\psi_{max}}(n=2)}{\psi_{max}(n=1)} = \frac{0.5\,\psi_{total}}{\psi_{max}(n=1)} = \frac{0.1754}{0.2774} = 0.63, \tag{6.1}$$

where n is the number of plumes in the box. This is consistent with the prediction (equation 2.14) for this ratio of $\sim 2^{-1/2} = 0.71$. Similarly, the ratio of the total rate of vertical volume transport in run 1 to run 5 will be,

$$\frac{\psi_{max}(n=2)}{\psi_{max}(n=1)} = \frac{0.1720 + 0.1787}{0.2774} = 1.26, \tag{6.2}$$

which is $\leq 2^{1/2} = 1.41$ and consistent with the upper bound prediction (equation

2.15). Thus the results from (6.1) and (6.2) are consistent with the predictions, confirming the extension of the scaling theory from Hughes & Griffiths (2008) to domains containing multiple plumes.

The scaling predictions from Hughes & Griffiths (2008) are based on multiple plumes having equal strengths, however it is insightful to calculate from the numerical solutions the ratio from (6.2) for unequal plumes. Figure 6.19*a* shows that the ratio of the total overturning strengths for $n = 2$ to $n = 1$ is largest for $|R_Q| = 0$, decreases to a minimum at $|R_Q| \approx 0.1$ before increasing slightly and approaching unity. Equation 2.15 suggests that the total overturning strength for one plume will be no more than $2^{-1/2} = 0.71$ times that for two plumes (carrying the same total buoyancy input). In figure 6.19*b* we plot the ratio of ψ_{sp}/ρ_o to $\psi_{max}(n = 1)/\rho_o$ (the result from (6.1) is plotted for $|R_Q| = 0$). The corresponding scaling prediction is marked by the red dot. The ratio then drops for slightly unequal plumes and then asymptotes to one as $|R_Q| \to 1$.

For the same total buoyancy input, two (or more) equal strength plumes will be able to entrain more interior fluid than any other combination of two (or more) plumes, including the case when all the buoyancy input is through one end. This is because the surface area over which entrainment can occur is greatest for two equal plumes but decreases in boxes with two unequal plumes (because the weaker plume has a smaller height and/or weaker turbulence) or only one plume. If more fluid is able to be entrained into the plumes then the overturning strength in the box will also be larger. These results are indicative only, as the two-dimensional numerics do not accurately model entrainment.

In conclusion the numerical runs are in good agreement with the laboratory results from chapter 5. Measurements of the confluence point and interior stratification confirms the importance of the stronger plume in governing the interior stratification once the mismatch in buoyancy forcing is greater than $\sim 10\%$. In addition the scaling prediction from Hughes & Griffiths (2008) was confirmed.

6.3 Internal waves in horizontal convection

Internal waves have been observed in numerical simulations of convection driven by differential heating of vertical endwalls. Patterson & Imberger (1980) discussed the approach to steady state of a differentially heated cavity. The convective circulation was laminar at the range of Rayleigh number and aspect ratio explored. Internal waves were generated when the tilted isotherms (which were formed during the

early stages of the simulation) were restored to being horizontal in the approach to steady state. The internal wave motion was damped by viscosity and momentum was deposited in the vertical boundary layer. Reaching a steady state depended on wave motions being damped and the time scale for the damping was found to be equal to H^2/ν, the cavity height squared divided by the viscosity. More oscillations were observed during the adjustment for simulations that had a higher Rayleigh number.

Later studies of flow in rectangular cavities with differentially heated endwalls (Le Quere & Behnia, 1998; Trias *et al.*, 2007; Xin & Le Quere, 1995) have investigated turbulent convection. Under these conditions eddies form in the statistically steady state and are subsequently ejected from the vertical endwall boundary layers. The eddies perturb the background stratification and therefore drive internal wave motions.

Our laboratory and numerical results show a small, but dynamically important interior stratification (its existence means at least one of the plumes must ascend through the full tank depth). We also see eddies forming in the endwall plumes and travelling into the interior of the domain. As this must disturb the stable stratification, it is reasonable to expect internal waves to be present in horizontal convection experiments. The observation of internal waves in the laboratory requires a method of measuring the complete velocity field, which was not practical for this thesis. Thus we look for their signature in the time series velocity data (both horizontal and vertical) from the numerical simulations. In fact we find that internal waves account for much of the time variability in the flow. Figure 6.20 shows a Hovmöller plot of the vertical velocity anomalies along $z/D = 0.5$ over a five hour period. The coherent propagating lines of constant phase are a signature of internal waves. An eddy that is advected by the surrounding mean flow will also give coherent propagating phase lines, but only at the height at which they travel ($0.6 < z/D < 1$) and only at very low frequencies ($\omega < 5 \times 10^{-4}$ Hz). Below we outline some useful findings from linear internal wave theory that will help us to characterise the internal waves present in these experiments.

6.3.1 Linear inviscid internal wave theory

Wave-like solutions (periodic in space and time) to the two dimensional equations of motion can be found in a quiescent stratified fluid with uniform density gradient

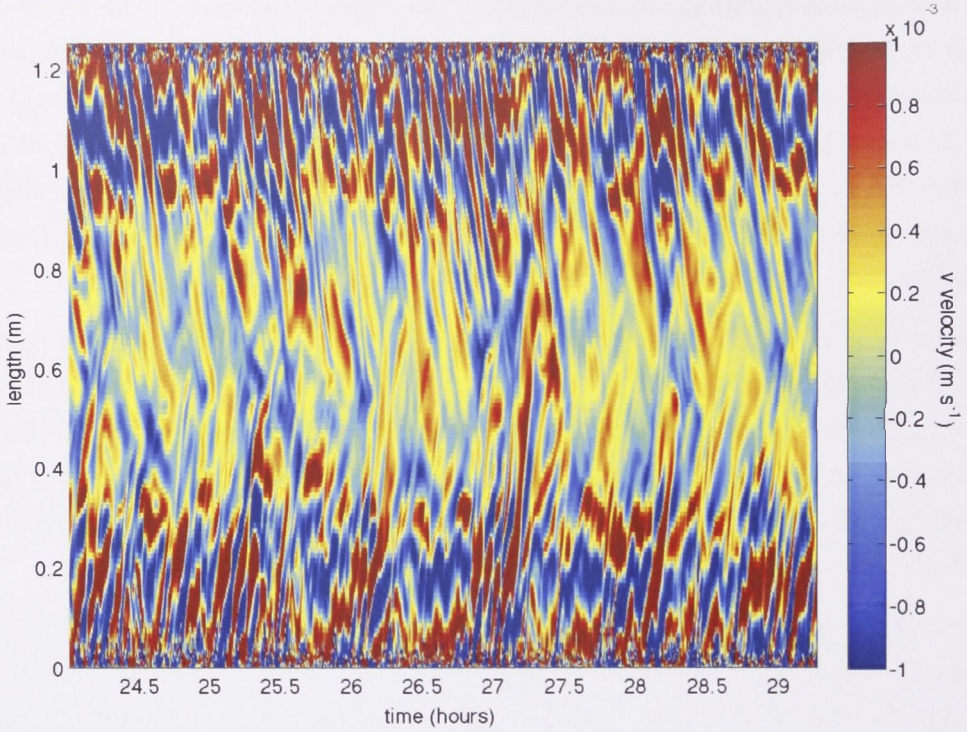

Figure 6.20: Hovmöller plot of the vertical velocity anomalies at mid-depth ($z/D = 0.5$) over a five hour period, for run 1. The typical phase speed from the most prominent lines of constant phase in this figure (dark red lines travelling along half of the tank length) is about 0.8 mm/s.

(Tritton, 1988; Turner, 1979) such that,

$$\omega = \frac{Nk}{(k^2 + m^2)^{1/2}}, \tag{6.3}$$

where ω, m and k are the angular frequency, vertical wave number and horizontal wave number, respectively, of the wave motion, and N is the Brunt-Väisälä frequency of the fluid. Equation 6.3 simplifies to

$$\omega = N \sin\theta \tag{6.4}$$

where θ is the angle the vectorial wave number, $\mathbf{k}$, makes with the vertical. The horizontal and vertical components of the wave number, $\mathbf{k}$, are,

$$k = \frac{2\pi}{\lambda_x} \tag{6.5}$$

and

$$m = \frac{2\pi}{\lambda_z} \tag{6.6}$$

where λ_x and λ_z are the distances between successive crests in the horizontal and vertical directions, respectively. The vectorial wave number is written as, $\mathbf{k} = \hat{\mathbf{x}}k + \hat{\mathbf{z}}m$, where $\hat{\mathbf{x}}$ and $\hat{\mathbf{z}}$ are the unit vectors parallel to the x and z axis respectively. We can write the relationship between k and m for any one internal wave mode in the form,

$$k = m \tan\theta. \tag{6.7}$$

Lines of constant phase move with speed, C_P, in the direction of $\mathbf{k}$, such that

$$C_P = \frac{\omega}{|\mathbf{k}|}, \tag{6.8}$$

with horizontal and vertical components,

$$C_{Px} = \frac{\omega}{k} \text{ and } C_{Pz} = \frac{\omega}{m}. \tag{6.9}$$

We can visualise the phase propagation associated with the internal wave modes using a Hovmöller plot such as that in figure 6.20.

The group velocity, C_g, indicates the speed and direction of the energy that is transmitted through the flow:

$$C_g = \left(\frac{\partial\omega}{\partial k}, \frac{\partial\omega}{\partial m}\right), \tag{6.10}$$

where the horizontal and vertical components are,

$$U_g = N\frac{m^2}{(k^2+m^2)^{3/2}} \text{ and } W_g = -N\frac{mk}{(k^2+m^2)^{3/2}}, \tag{6.11}$$

respectively. Fluid motion is perpendicular to the wave number, $\mathbf{k}$, and is therefore in the same direction as the group velocity. These relations are expected to hold so long as N varies only slowly with z.

6.3.2 Measuring the internal waves

We measure the characteristics of the internal waves present in each of the numerical runs. Equations 6.3, 6.4, 6.8 and 6.11 contain 3 unknowns: θ, m and k. The buoyancy frequency may be approximately determined by measuring the average value of the thermal gradient between $0.30 < x < 0.96$ and $0.037 < z < 0.163$, i.e.

away from the influence of the horizontal and vertical boundaries and outside the thermal boundary layer. The buoyancy frequency,

$$N = \left(g\alpha \frac{dT}{dz} \right)^{1/2}, \tag{6.12}$$

for each run is given in table 6.2, where in all cases $\alpha = 3.282 \times 10^{-4}$ °C and $g = 9.8\,\mathrm{m/s^2}$. The buoyancy frequency increases as $|R_Q|$ is increased. For simplicity we have assumed that the interior is uniformly stratified. The boundary layer stratification is much stronger than in the interior and any internal wave modes excited in this region will not be able to propagate into the interior of the box if they exceed the buoyancy frequency of the interior. More generally, if the buoyancy frequency in a stratified box is not constant, then the internal waves will be trapped in the region where $\omega \leq N$ and will die away exponentially in a region where $\omega > N$.

Table 6.2: The interior buoyancy frequency for each numerical run.

Run	N (rad/s)	N (1/s)
1	0.0134	0.00214
2	0.0156	0.00248
3	0.0161	0.00256
4	0.0176	0.00280
5	0.0191	0.00304
6	0.0182	0.00289

We subtract the mean horizontal and vertical velocity fields from the instantaneous horizontal and vertical velocity fields, respectively. Using the time series of velocity anomalies, it is possible to measure the angular frequencies, ω, and corresponding phase velocities, C_P, of the internal wave modes.

We found that several internal wave modes were simultaneously present in the box. This was evident upon taking a fast fourier transform of the time series velocity anomalies at each of 21 points distributed throughout the domain (figure 6.21*c*) to find the coherent angular frequencies in each run. The peak power was much larger in the spectra near the plume outflow, therefore spectra were normalised by the maximum value from each spectra. Figure 6.21*a* and *b* show the normalised power spectra for the vertical and horizontal velocity anomalies, respectively, for run 1. The colours and dashed lines denote the position of the measurement, as described in the caption of figure 6.21. The degree to which individual spectra are correlated varies between points in the box and also between the vertical and horizontal fields. In each run we found four or five peaks in the frequency spectrum that were below

the buoyancy frequency, N. The same peaks in the frequency spectrum are evident in both the horizontal and vertical velocity anomaly plots, as we would expect for each wave mode. Table 6.3 is a compilation of all the peaks detected in the power spectra for each run. The solid and dotted lines in the power spectra denote results from $z/D = 0.8$ and $z/D = 0.2$, respectively. These points coincide with the upper and lower limits of the region over which N was calculated. Beyond this region, N is likely to vary greatly (especially in the boundary layer region). Thus, in figure 6.21 and in all the power spectra plots (not shown here) for the other runs, we see some significant correlation of spectral peaks at frequencies $> N$, typically from locations close to the boundaries. These wave modes, which are probably evanescent throughout most of the box, have not been analysed.

Using (6.4) we can calculate θ, the angle the wave number vector makes with the vertical, and which is also the angle the group velocity vector makes with the horizontal. Presented in table 6.3 is θ, for each mode in each run. Four peaks were detected for runs $1 - 4$ and 6 and five peaks were detected in run 5. For run 2 the peak with the second lowest frequency has been split into two close sub-peaks that were detected separately in different regions of the tank, but were not completely coincident.

In addition to identifying the dominant frequencies of each run we also determined the band-width of each peak and used a band-pass fourier filter to isolate each of the propagating phase lines (see table 6.3 for the width of each filter). Using the filtered data, Hovmöller plots were constructed for the three vertical and three horizontal sections illustrated in figure 6.21*c*. We show a selection of filtered Hovmöller plots from run 1 in figures 6.22 and 6.23. Figure 6.22 shows the horizontal section along $z/D = 0.5$ of the horizontal velocity anomaly time series, and figure 6.23 shows the corresponding vertical section from $x/L = 0.9$ of the vertical velocity anomaly time series. In these figures the propagation of lines of constant phase is apparent for each wave mode. Figure 6.22 clearly shows the interaction in the centre of the box between the wave modes generated at each end. In particular, the variation of the confluence point position is associated with superposition of a number of internal wave modes, given the oscillatory behaviour of horizontal velocity anomalies along the central axis ($x \sim 0.625\,\mathrm{m}$).

In a Hovmöller plot the gradient of any line of constant phase will yield C_{Px} or C_{Pz} (depending on the orientation of the slice). Figure 6.22 (and all the other Hovmöller plots along a horizontal section from run 1) shows that in general the sign of C_{Px} is positive in the left half of the box and negative in the right half of the box. Figure 6.23 (and all Hovmöller plots from a vertical section) shows the sign of

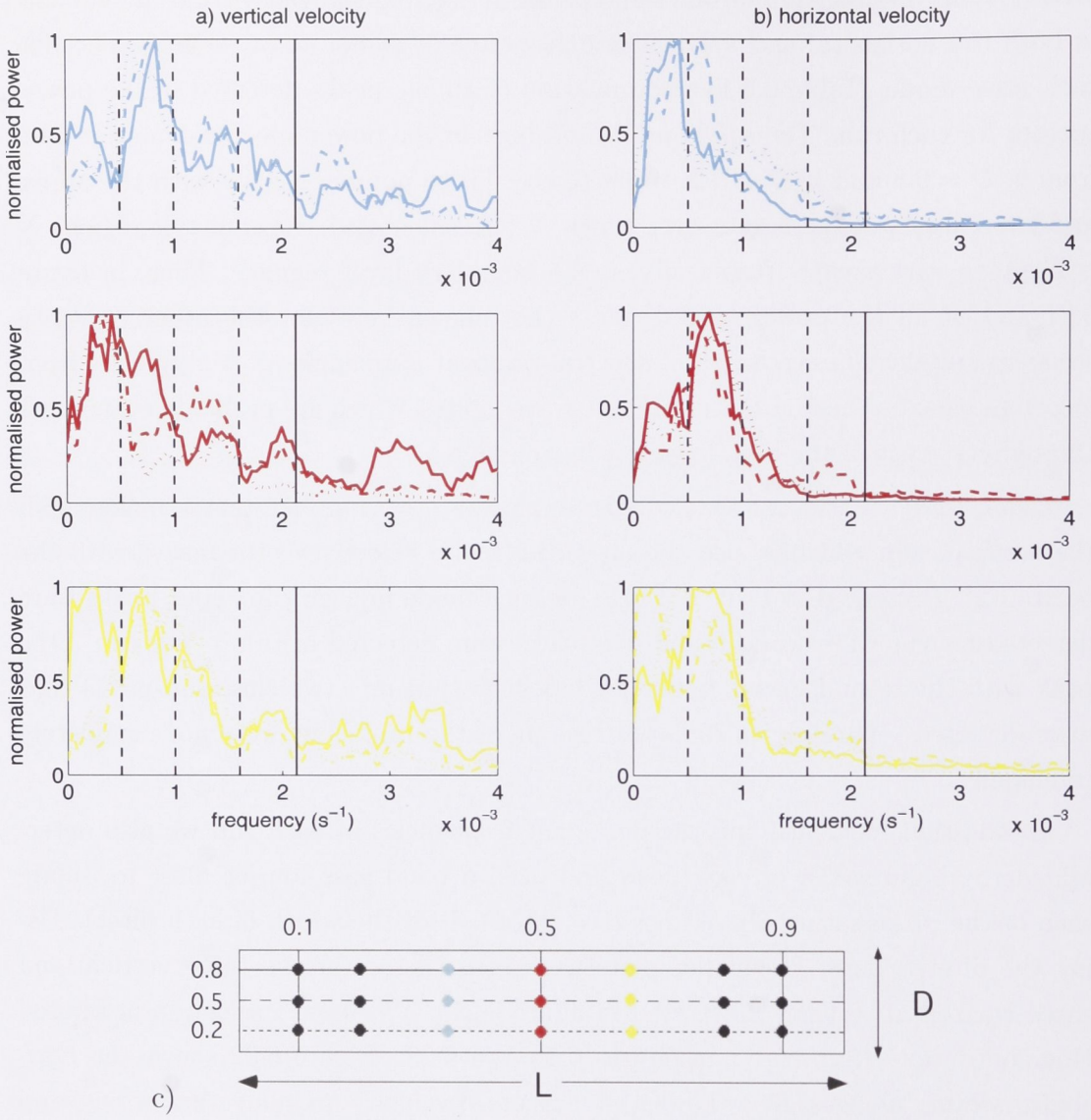

Figure 6.21: The power series from 9 points distributed throughout the box (run 1), calculated using a fast fourier transform of the a) local vertical velocity anomaly time series and b) local horizontal velocity anomaly time series. The spectra from each point has been normalised by the maximum peak value and the buoyancy frequency, N, is indicated by the solid vertical line. The band-width of each dominant frequency is indicated by the dashed and solid vertical lines. The schematic in c) is a side view of the box and serves as a legend for the coloured lines and line styles of a) and b). The power series spectra for the black dots is not shown here for brevity. The colour of a line represents the x position of the point and the style of the line represents the vertical location of the point. The numbers in c) indicate the value of z/D or x/L for the numbers aligned in the vertical or horizontal, respectively. The black lines also indicate the slices along which Hovmöller plots are made.

Table 6.3: The internal wave modes measured in the numerical experiments with the corresponding value of θ (angle of wave number vector from the vertical) and the frequency range over which the horizontal and vertical velocity time series were filtered.

Run	mode	ω (1/s)	θ (degrees)	band-pass filter (Hz)
1	1	0.25×10^{-3}	6.7°	0–0.0005
	2	0.75×10^{-3}	20.5°	0.0005–0.001
	3	1.30×10^{-3}	37.4°	0.001–0.0016
	4	1.87×10^{-3}	60.7°	0.0016–0.00213
2	1	0.20×10^{-3}	4.6°	0–0.0004
	2a	1.10×10^{-3}	26.3°	0.0004–0.0015
	2b	1.40×10^{-3}	34.3°	0.0012–0.001655
	3	1.95×10^{-3}	51.7°	0.001655–0.00215
	4	2.48×10^{-3}	90°	0.00215–0.0027
3	1	0.25×10^{-3}	5.6°	0–0.0005
	2	0.83×10^{-3}	18.8°	0.0005–0.00115
	3	1.53×10^{-3}	36.5°	0.00115–0.0019
	4	2.23×10^{-3}	60.5°	0.0019–0.00256
4	1	0.65×10^{-3}	13.4°	0–0.0012
	2	1.85×10^{-3}	41.3°	0.0012–0.00205
	3	2.25×10^{-3}	53.4°	0.00205–0.0026
	4	2.80×10^{-3}	90°	0.0026–0.0033
5	1	0.45×10^{-3}	8.5°	0–0.001
	2	1.2×10^{-3}	23.3°	0.0075–0.0013
	3	1.8×10^{-3}	36.3°	0.0013–0.00235
	4	2.55×10^{-3}	57.1°	0.00235–0.0028
	5	3.04×10^{-3}	90°	0.0028–0.0034
6	1	0.4×10^{-3}	8.0°	0–0.0009
	2	1.45×10^{-3}	30.1°	0.0009–0.0018
	3	2.05×10^{-3}	45.2°	0.0018–0.0023
	4	2.80×10^{-3}	75.7°	0.0023–0.00345

C_{Pz} is positive (upwards) throughout the box depth. Thus for run 1 the internal wave field is generated in the top corner of each end of the box, and corresponds to where we would expect the fluctuating plume outflow and eddy generation to strongly perturb the background stratification. The numerical runs reveal the same location for the internal wave generation points in runs 2 and 3. For runs 4, 5 and 6 one plume is dominant, we do not see eddy-shedding from the weak plume, and we only detect waves generated from one end of the box. We measured C_P for all the peaks in the frequency spectra for run 1 and the results are plotted in figure 6.24. Each data point represents the average over all the lines of constant phase for one Hovmöller plot, with one standard deviation error bars to indicate the spread of the data. The closed circles are measurements of C_{Px} and C_{Pz} from the vertical velocity anomalies and the open circles are the corresponding measurements from the horizontal velocity anomalies. The cross is the average value of the C_{Px} and C_{Pz} measurements from both horizontal and vertical velocity anomalies.

Equation (6.7) and (6.8) can be combined to find the theoretical relationship between C_{Pz} and C_{Px},

$$C_{Pz} = tan\theta \, C_{Px}. \tag{6.13}$$

We plot this relationship in figure 6.24 using the measured θ, and expect the value of C_{Px} and C_{Pz} to lie on the dashed line. The data and theory closely agree for mode 4, there is some agreement for modes 2 and 3, but none for mode 1. For small angles, θ, the accuracy of the vertical phase velocity measurement is greater than the corresponding horizontal phase velocity measurement. This is evidenced by the smaller error bars (modes 1 and 2) for C_{Pz} compared with C_{Px} in figure 6.24, and we therefore use the average value of the C_{Pz} data and equation (6.13) to find a more accurate value for C_{Px} for modes 1 and 2, given in table 6.4. The accuracy of the measurement of the two phase speeds is equivalent for modes 3 and 4, and for these we take the average values as they appear in figure 6.24.

The horizontal phase speed from modes 3 and 4 appears to be approximately independent of mode and equal to $6.7 \pm 0.2 \times 10^{-4}$m/s. This observation leads to the development of a simple model for internal wave generation and propagation in horizontal convection, which will be outlined in the next section.

Using equation (6.8) and the our best values of C_{Px}, C_{Pz} and ω we were able to calculate the horizontal and vertical wave numbers, k and m, respectively, for each mode in run 1 (table 6.4). Having determined k and m for each internal wave mode we also use equation (6.11) to calculate the group velocity and its components U_g and W_g. Figure 6.25 shows the magnitude and direction of the group velocity for

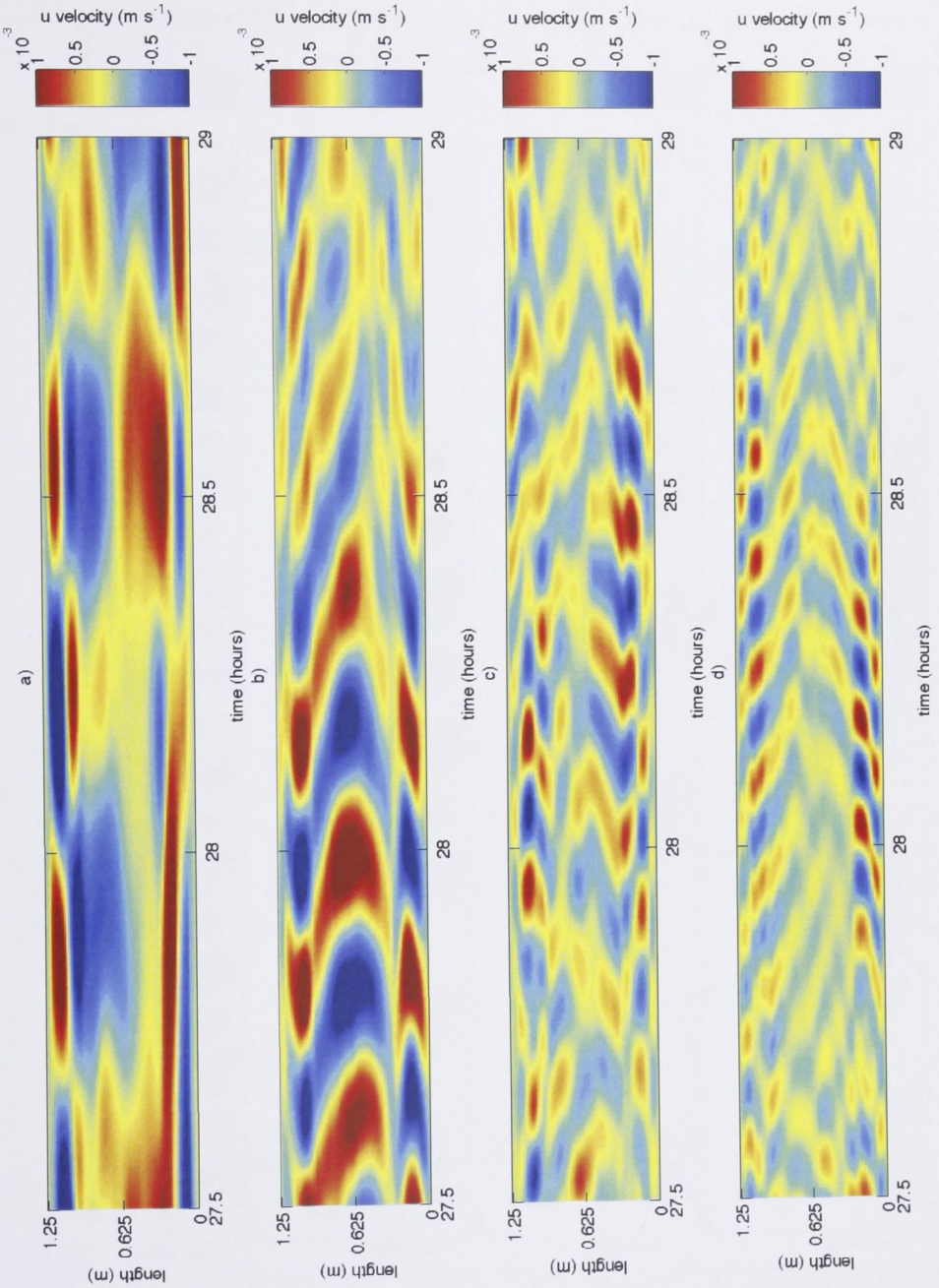

Figure 6.22: Filtered Hovmöller plots of horizontal velocity anomaly (ms^{-1}) versus distance along the box, over 1.5 hours for run 1 ($R_Q = 0$). The band-pass filters are, a) $0 - 0.0005\,Hz$, b) $0.0005 - 0.001\,Hz$, c) $0.001 - 0.0016\,Hz$ and d) $0.0016 - 0.00213\,Hz$.

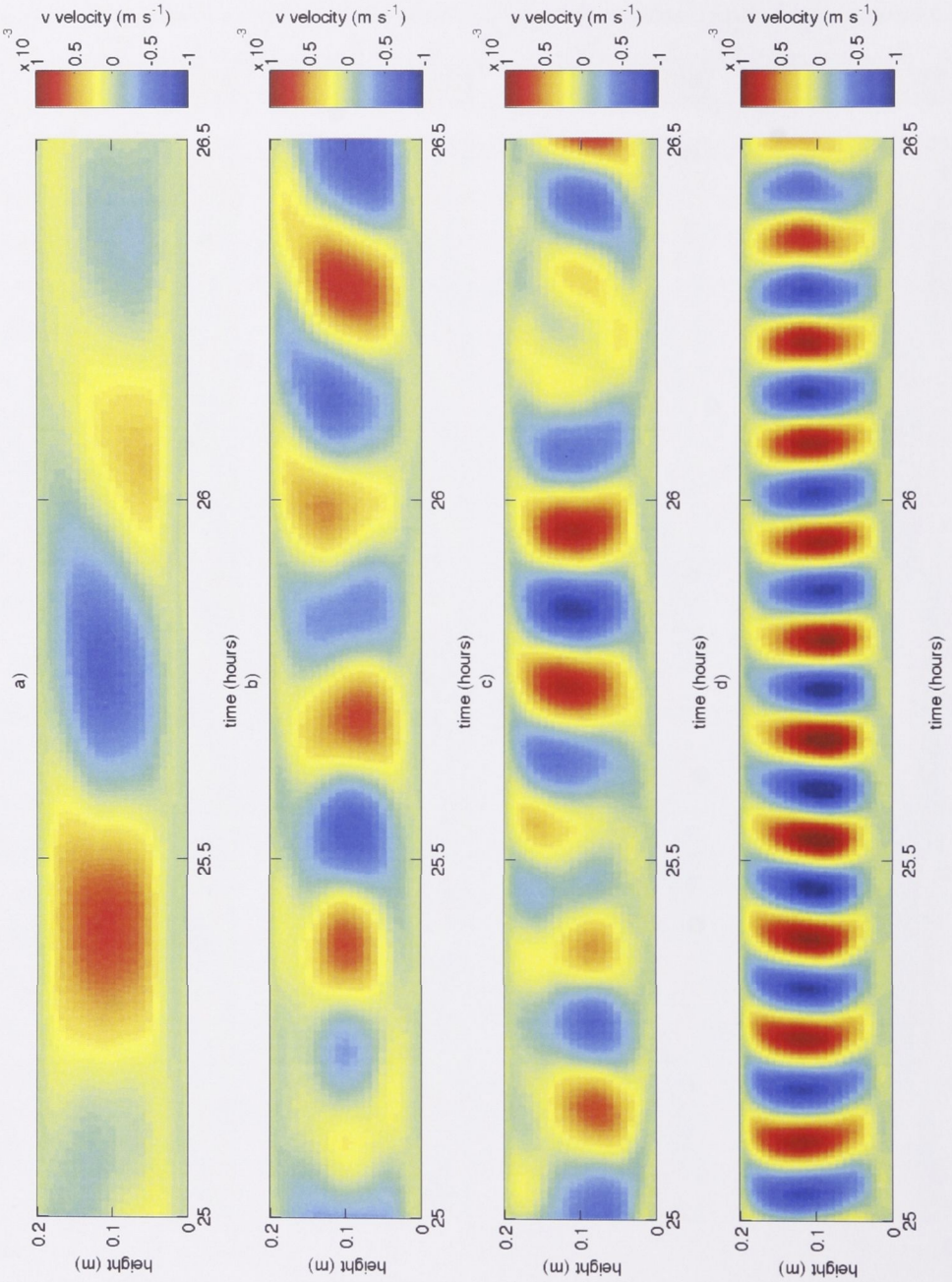

Figure 6.23: Filtered Hovmöller plots of vertical velocity anomaly (ms^{-1}) versus height, over 1.5 hours for run 1 ($R_Q = 0$). The band-pass filters are, a) $0 - 0.0005\,Hz$, b) $0.0005 - 0.001\,Hz$, c) $0.001 - 0.0016\,Hz$ and d) $0.0016 - 0.00213\,Hz$.

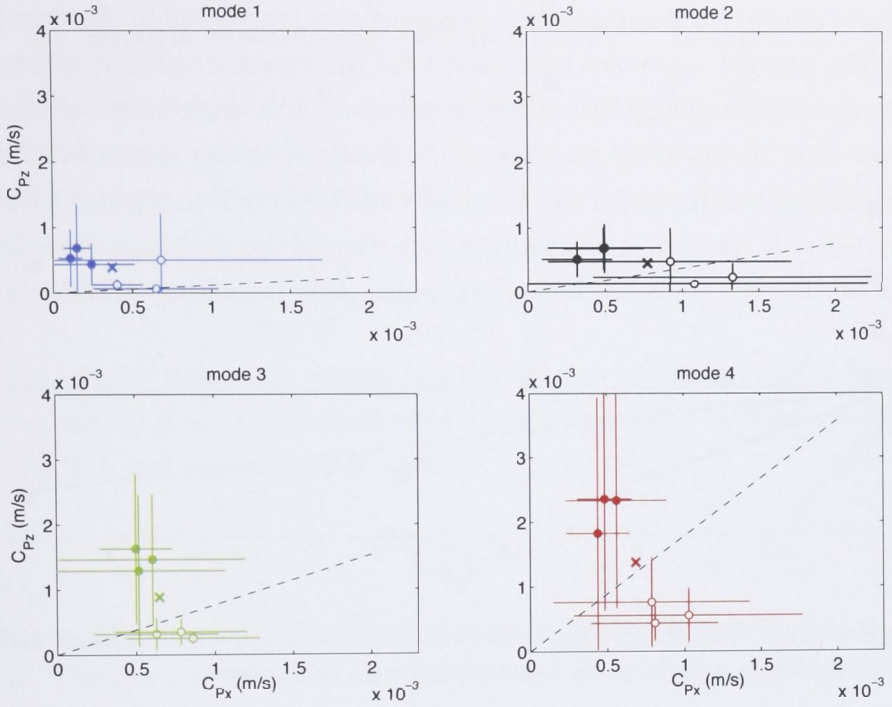

Figure 6.24: The measured phase velocity components for run 1. The closed circles are measurements of C_{Px} and C_{Pz} from the vertical velocity anomalies and the open circles are the corresponding measurements from the horizontal velocity anomalies. The error bars represent one standard deviation. The cross is the average of all data points. The dashed line is the theoretical relationship between C_{Pz} and C_{Px}.

Table 6.4: Internal wave mode characteristics for run 1.

Run 1							
mode	k	m	θ	C_{Px} (mm/s)	C_{Pz} (mm/s)	U_g (mm/s)	W_g (mm/s)
1	0.5	4.0	6.7°	3.303	0.388	3.252	−0.383
2	3.92	10.5	20.5°	1.204	0.450	1.053	−0.394
3	12.6	9.3	37.4°	0.647	0.881	0.300	−0.409
4	17.1	8.6	60.7°	0.685	1.364	0.141	−0.281

each internal wave mode. U_g is plotted with an aspect ratio equivalent to the box aspect ratio and with the internal waves being generated from the outflow of only the left hand plume, although the same internal waves are excited in the right plume outflow. The internal waves are numbered 1 for the lowest frequency, which is the wave with the shallowest angle to the horizontal, to 4 for the highest frequency, which is the wave that has the smallest horizontal component of the group velocity. The lower frequencies will travel further into the tank before encountering the bottom boundary layer. It is not clear whether any reflection of the wave rays occur because the boundary layer is not solid, but a region of rapidly increasing stratification.

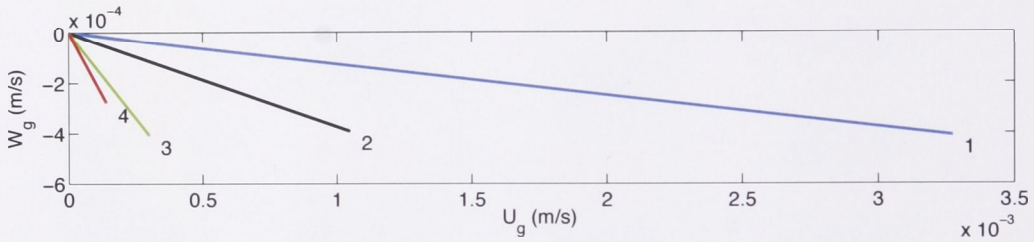

Figure 6.25: The group velocity in run 1. The scales of the horizontal and vertical velocity axes have the same aspect ratio as the box.

Our use of linear internal wave mode theory has thus far not considered the presence of the four boundaries. However the tank is finite, and as such we expect wave modes with a discrete number of wavelengths to be dominant in the box, as resonant or normal modes. We allow integer multiples of quarter wavelengths so that k and m can also be written as,

$$k = \frac{4\pi}{\lambda_x} = \frac{\pi i}{L} \tag{6.14}$$

and

$$m = \frac{4\pi}{\lambda_z} = \frac{\pi n}{D}, \tag{6.15}$$

where i is the number of horizontal quarter wavelengths of the corresponding horizontal component of the wave number and n is the number of vertical quarter wavelengths of the vertical wave number. Here i and n are by definition integers ≥ 1. We have assumed that the endwalls and horizontal boundaries must be nodes or anti-nodes for each mode. This would not be acceptable if the stratification throughout the whole box were linear, however the large horizontal velocities near the lid admit the possibility of an anti-node in the vertical modes in the vicinity of the upper boundary. Similarly, large vertical velocities near the endwall plumes

admit the possibility of antinodes in this region.

6.3.3 A simple model for the generation of internal waves

In what follows we consider the internal wave field generated in the box by one plume. The outflow from the plume must adjust its speed and depth so as to accommodate the volume flux per unit width of the plume, Q, which we can estimate using the maximum stream function as,

$$Q \approx \frac{\overline{\psi_{max}}}{\rho_0}, \tag{6.16}$$

where $\overline{\psi_{max}}$ is the maximum stream function of the overturning cell and ρ_0 is the reference density. If the plume outflow can be approximated by a steady plug flow, having depth h and mean speed U, then,

$$Q = Uh. \tag{6.17}$$

The plume outflow generates the internal waves by perturbing the background stratification. Therefore, we propose that the internal wave modes that will be excited will have a horizontal phase speed that matches the average horizontal velocity in the plume outflow,

$$C_{Px} = U. \tag{6.18}$$

This assumption is supported by the measured values of C_{Px} for run 1, which show the internal wave modes 3 and 4 to have $C_{Px} = 6.7 \pm 0.2 \times 10^{-4}$m/s, and the outflow velocity $U \approx 8 \times 10^{-4}$m/s. Equation 6.18 is not supported by the adjusted C_{Px} values for modes 1 and 2, and in this simple model we neglect this discrepancy. Therefore for two different internal wave modes A and B,

$$C_{Px} = \frac{\omega_A}{k_A} = \frac{\omega_B}{k_B}. \tag{6.19}$$

Combining (6.8) and (6.18) we find,

$$U = \frac{\omega_j}{k_j}, \tag{6.20}$$

where ω_j and k_j are the angular frequency and horizontal wave number of the permissible internal wave modes which are more generally numbered as j. Although the outflow takes the form of propagating eddies, or solitary wave-like pulses or boluses, to accommodate the flux, Q, we do not consider this in a zeroth-order description.

Combining (6.20) and (6.3) we find the range of wave modes likely to exist for a given stratification and horizontal plume outflow velocity in (k, m) space to be,

$$k^2 + m^2 = \left(\frac{N}{U}\right)^2. \tag{6.21}$$

Therefore, the possible modes will exist along one circle of radius N/U in (k, m) space. A further restriction of the possible values of k and m for a given run can be obtained with the assumption that only vertical normal modes are excited by the plume outflow. We require that the wavelength of a vertical mode be four times the box height divided by an integer, n, and conjecture that the energy will predominantly go into those modes having a vertical scale comparable to the outflow depth, h. In particular we anticipate that the vertical wavelength, λ_z, of the modes having largest amplitude will be of $O(c_j h)$, where c_j is a constant for the jth mode. The vertical wave number is $m_j = 4\pi/\lambda_z$, and the vertical wave length of the vertical mode becomes,

$$\lambda_z = 4D/n \sim c_j h, \tag{6.22}$$

where n is a real positive integer. Thus

$$c_j m_j \sim \frac{4\pi}{h}. \tag{6.23}$$

Using (6.3), (6.23) and (6.17) we expect,

$$Q \approx \frac{N}{(k_j^2 + m_j^2)^{1/2}} \frac{4\pi}{c_j m_j}. \tag{6.24}$$

Therefore the model suggests that the dominant normal mode will satisfy:

$$m_j({k_j}^2 + {m_j}^2)^{1/2} \approx \frac{4\pi N}{Q c_j}. \tag{6.25}$$

Only the size of c_j remains to be determined. We restrict the range of possible values of c_j by considering the physical limitations of the flow. Firstly, using the laboratory and numerical experiments as a guide, we expect the outflow depth, h, to be in the range $D/5 < h < D/2$. From equation (6.22),

$$c_j \sim \frac{4D}{nh}, \tag{6.26}$$

and using the range of expected values for h we find, $8/n < c_j < 20/n$.

Finally we consider the possible values of n, the number of quarter wavelengths

in a distance D for the vertical mode, m_j. When $n = 1$, $\lambda_z = 4D$ and the wave has maximum amplitude at the upper boundary and a node at the lower boundary. The range of c_j for this case is $8 < c_j < 20$. The largest value of n we expect to correspond to a strongly excited wave mode is $n = 4$, because larger n would not match the observed depth profile of the horizontal velocities. When $n = 4$, $\lambda_z = D$ and the vertical mode contains either nodes or antinodes at the top, centre and bottom of the box, with the upper region having positive amplitude and the lower to central negative amplitude. The range of c_j for this case reduces to $2 < c_j < 5$. Thus the observed velocity structure is likely to have c_j in the range $2 < c_j < 20$. The range of $4\pi N/Qc_j$ in equation (6.25) can now be found for each run and will act as a limit to the contours described by equation (6.21).

We can now determine the value of the contour lines for each run in wave number space using equation (6.25). The maximum stream function of the stronger plume for each run is given in table 6.5, along with the calculated value of Q, and the range of $4\pi N/Qc_j$ from equation (6.25). The calculated wave numbers for run 1 are plotted in figure 6.26, along with four other theoretical and model constraints. These are, the theoretical predictions for the relationship between k and m (equation (6.7), thick black radial lines), the contours that all permissible combinations of k and m for a given run should lie on (equation (6.21), lighter black lines), the predicted range that k and m should lie in (equation (6.25), red contours), and the range of values N/U would take using the maximum and minimum values of C_{Px} measured in the Hovmöller plots (blue lines). The use of the theoretical relation to constrain C_{Px} for modes 1 and 2 means that the data points fall directly onto the radial lines of ω_1 and ω_2. Wave mode 4 falls close to the theoretical radial line for ω_4 while wave mode 3 is somewhat removed from ω_3 (and, because the errors on the phase velocity data for this mode were of similar magnitude, no adjustment was made). Wave modes 2 - 4 fall into the bounds predicted by the model, while it is clear by the placement of mode 1 that the measurement techniques for very low frequency modes are not yet adequate. We have also used the model to predict the range of k and m for the remaining numerical runs, see figure 6.27. This simple model, considering the assumptions made in it's development, gives a reasonable guide to the range of k and m values that will arise in a horizontal convection experiment. The modal will break down if the horizontal phase speed, C_{Px}, is not comparable to the average plume outflow (as was the case once the adjustment to C_{Px} was made for modes 1 and 2 from run 1).

The sign of the vertical and horizontal phase velocities imply the source of the

Table 6.5: Maximum stream function, ψ_{max}, the estimated plume volume flux per unit width, Q, and the range of values for the right hand side of equation 6.25, for each numerical run. The value of N for each run can be found in table 6.2.

Run	ψ (kg/s)	Q (m^2/s)	$4\pi N/Qc_j$ (m^{-2})
1	0.1754	1.763×10^{-4}	478 – 48
2	0.1431	1.439×10^{-4}	682 – 68
3	0.1571	1.580×10^{-4}	640 – 64
4	0.2135	2.146×10^{-4}	516 – 52
5	0.2774	2.789×10^{-4}	430 – 44
6	0.2624	2.638×10^{-4}	432 – 44

internal wave modes to be near the top corners of the box. Thus we conclude that the internal waves are generated by the horizontal outflow from each of the endwall plumes. When the plumes have unequal strength so that only one plume penetrates through the full depth of the box, the source of detectable internal waves is near the outflow from only the stronger plume. The group velocities of each of the modes in run 1 show the difference in the horizontal distance (for the same time) that a wave mode can travel before encountering a boundary. We would anticipate the lower modes to be important in setting the time scale on which the plumes interact.

In Section 6.2 we outlined the large amount of variability that was observed in all numerical runs. The eddies are a cause of some of the variability we see in the flow, however, the frequency of eddy ejection is smaller than many of the variation frequencies we see in the animations (also evident in the time sequence of horizontal velocities, figure 6.7). Upon measuring the internal wave field, we have found a number of dominant frequencies spanning a range of periods from hours to minutes, which covers the frequency of variations observed in the flow. Thus it seems likely that the presence and interactions of internal waves induces much of the high frequency variability we observe in the flow.

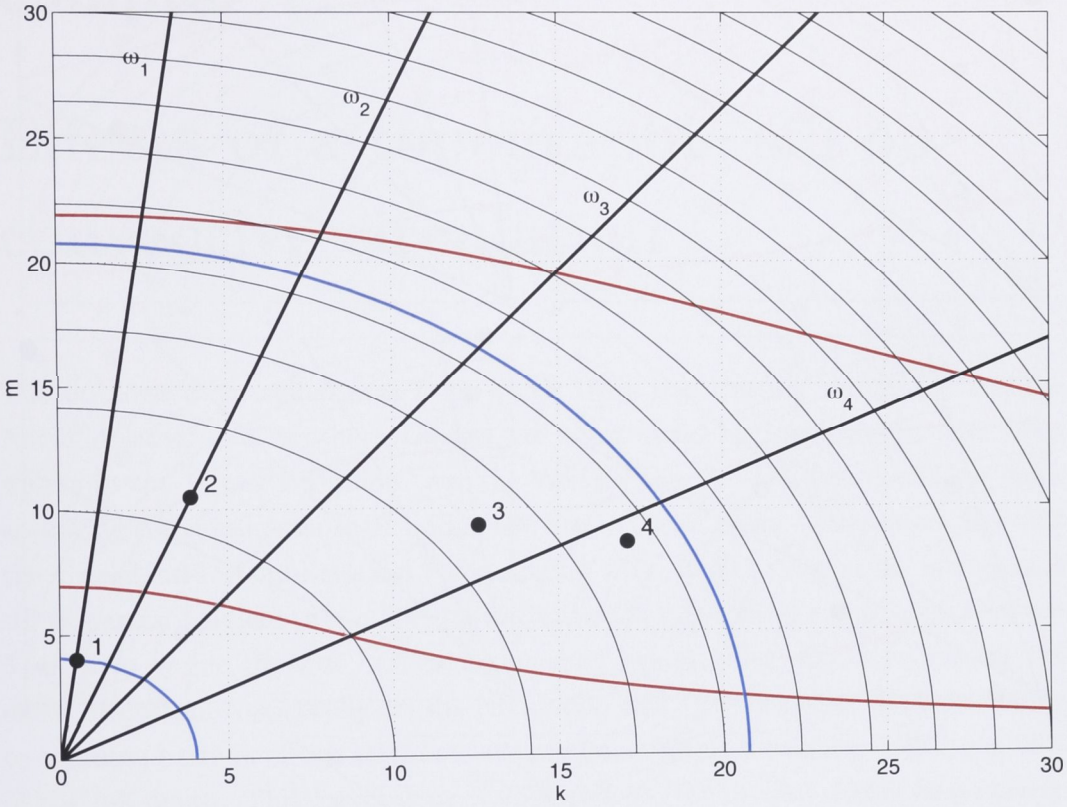

Figure 6.26: Black dots indicate the measured horizontal and vertical wave numbers for each of the internal wave modes in run 1. The blue contour lines are limits using the measured values of C_{Px} and equation 6.21. The black radial lines mark the theoretical relationship: $k = m\,tan\theta$, for each internal wave mode detected in the run. The lighter black lines show the form of the contour given by equation 6.21 (i.e. $(N/U)^2$), the red contour lines give the range of $4\pi N/Qc_j$, for $c_j = 2$ to 20. According to the model all possible wave modes will lie on one black contour satisfying equation 6.21 between the red contours specified by 6.25. The separation between the example black contour lines is 200.

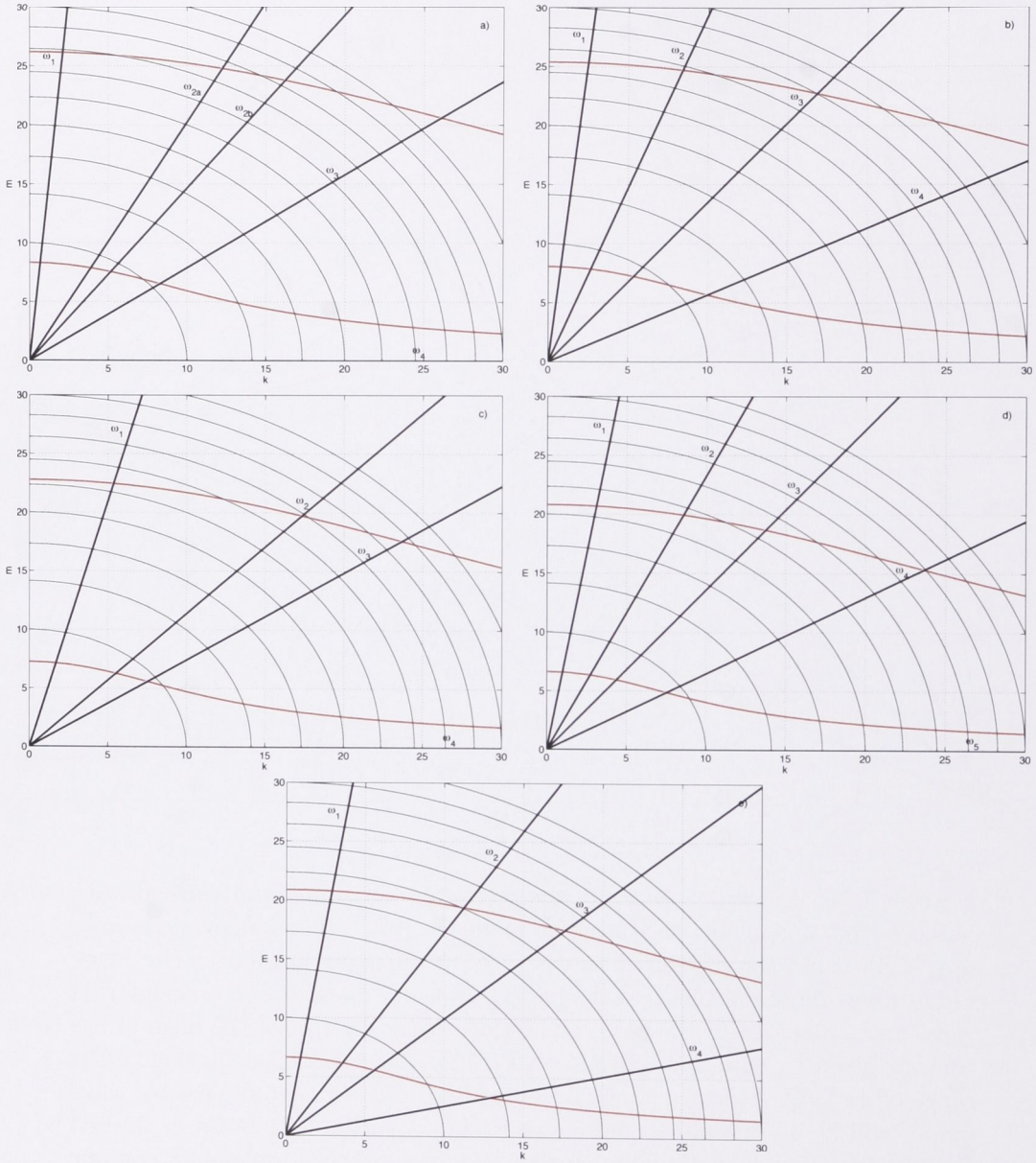

Figure 6.27: Predictions for the location of viable wave numbers based on the model presented in section 6.3.3 for a) run 2, b) run 3, c) run 4, d) run 5 and e) run 6. See the caption is figure 6.26 for details.

Chapter 7

Effects of a topographic sill on convective circulation

The outflows of marginal seas from which Deep and Bottom waters form in the North Atlantic and Southern Oceans are constrained by topography. The Deep waters in the Weddell Sea flow over the Weddell Sea ice shelf before sinking down and along the continental shelf, and in the Arctic Ocean Basin dense waters flow over the Greenland-Iceland-Scotland Ridge (figure 1.3). In this chapter we introduce a sill (a partial barrier) to the horizontal convection experiment reported in Chapter 5 so as to divide the box into two connected basins. Our aim is to explore the effect of bottom topography on the circulation and stratification. We have chosen to examine barriers of two different heights, mimicking sill heights of 75% and 90% of the full depth. This leaves gaps of 25% and 10% of the full depth, respectively, through which water can be exchanged between basins. These barriers were chosen to lie in the range of heights for which the overall circulation is likely to be strongly influenced. Dense waters can be trapped behind the sill in a marginal sea, leaving only a small range of depths above the sill for exchange of surface and overflow water. For instance, the North Atlantic Ocean, into which the Greenland-Iceland-Scotland overflow enters, is approximately 4000 m deep and the crest of the sill is less than 600 m deep in the Denmark Straits and 850 m deep for the Faroe Bank Channel.

7.1 Apparatus and Procedure

7.1.1 The tank

We have used the same experimental apparatus as described in Chapter 5 (where the boundary condition along the base of the tank captures the essential aspects of

thermal forcing at the ocean surface), with the insertion of a partial-height vertical barrier in contact with the tank lid. This created one small basin and one larger basin which were connected through the gap below the barrier (figure 7.1). The same procedure and measurement techniques used in Chapter 5 were employed for these experiments. In the remainder of this chapter we use the term 'sill' to describe the partial-height vertical barrier (in the inverted laboratory experiments) and bottom topography (in the ocean orientation).

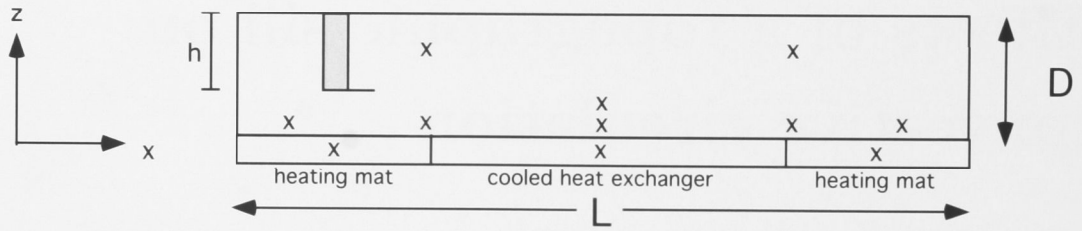

Figure 7.1: Side view of the experimental apparatus used for the horizontal convection experiments including the effect of a sill. × are the locations of the stationary thermistors.

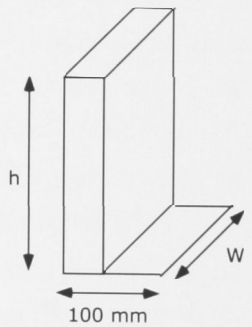

Figure 7.2: Side view of the schematic sill design used in this series of experiments. The rectangular block of high density foam is 50 mm wide and the acrylic overhang is also 50 mm wide.

For the horizontal convection experiments with two destabilising regions the endwall plumes are driven by horizontal gradients of density (and pressure). The exchange across the sill between the small basin and the large basin will be driven by the horizontal pressure difference across the sill due to the baroclinic density structure. We designed a sill that promotes unsteadiness and entrainment in the overflow. This is important because we want to compare the present results with the results from Chapter 5, which had unsteady, entraining plumes. A variety of nominally vertical sill designs were tested, using visualisation of the flow with

neutrally buoyant food dye to determine whether the overflow was turbulent. The final design, figure 7.2, was a two dimensional rectangular block of high density foam with an acrylic overhang, as long again as the sill width, attached to the top of the sill. This ensured the overflow was unsteady and entraining fluid but otherwise two-dimensional. Apart from promoting turbulent mixing in the overflow plume, this artificial device is expected to have no other effect on the flow. Rubber sealing on the three sides of the high density foam that were in contact with the tank walls and lid ensured all of the fluid exchange occurred through the gap below the sill.

7.1.2 Method

We filled the tank with de-aired water and added salt to create a 2% solution. We placed the sill in contact with the lid at $x/L = 1/8$ and then screwed the lid in place and lowered the thermistor rack into the tank. The approach to thermal equilibrium was monitored by plotting a time series of the temperatures measured by the stationary thermistors positioned as indicated in figure 7.1. Thermal equilibrium was judged to have been reached after the interior temperature was constant for at least one day (which typically occurred after five days). Once the flow was in thermal equilibrium the traverser was used to obtain vertical temperature profiles at five x locations along the tank. A measurement was taken every 0.01 mm and the results averaged over 10 readings to give a vertical resolution of 0.1 mm (details in Chapter 5). Observations of the flow were made using potassium permanganate crystals and neutrally buoyant food dye. The aspect ratio (5.2), Prandtl number (5.3) and flux Rayleigh number (5.4) were all held constant. We varied the heat flux ratio (5.5) between the two heating regions along with a new parameter, the normalised gap height

$$\varphi = \frac{D - h}{D}, \tag{7.1}$$

where h is the height of the sill and D is again the depth of the box. Five experiments were conducted in this series of experiments. Table 7.1 shows the parameter range explored. $\varphi = 1$ corresponds to the case with no sill studied in Chapter 5. However, these three $\varphi = 1$ experiments were completed after the series of experiments in Chapter 5. This is because the heating mat from the left end of the tank needed to be replaced after the series of thirty experiments in Chapter 5 and the new heating mat, of the same specifications, resulted in a slightly different temperature gradient along the left half of the copper base plate.

Table 7.1: Parameter range explored for the sill experiments.

Experiment	φ	R_Q	Ra_F	Pr
1	0.25	-0.0422	4.3×10^{14}	4.86
2	0.25	0.1164	4.3×10^{14}	4.86
3	0.10	-0.0422	4.3×10^{14}	4.86
4	0.10	0.0517	4.3×10^{14}	4.86
5	0.10	0.1164	4.3×10^{14}	4.86
33	1	-0.1389	4.3×10^{14}	4.86
34	1	-0.0131	4.3×10^{14}	4.86
35	1	-0.0422	4.3×10^{14}	4.86

7.2 Results and discussion

7.2.1 Qualitative observations: Effect of the sill

The addition of a sill creates a small basin that is filled by the outflow from the plume at the left hand end (see figure 7.3*b* and 7.3*c*). The water from the left plume pools behind the sill, creating a reservoir of hot water. In the equilibrium state the smaller hot reservoir constantly empties through the gap past the sill with a mass and volume flux identical to that entering in the bottom boundary layer. Provided that the buoyancy is large enough the water leaving the small basin will form an overflow that entrains interior fluid as it rises into the larger basin and subsequently flows along the upper boundary (or the ocean bottom). If the buoyancy is not great enough the water leaving the small basin forms an intrusion into the larger basin, just above the boundary layer. Even when an overflow occurs, some portion of the bottom boundary layer feeding the left plume may not be buoyant enough to rise into the small basin and so a weak intrusion forms above the boundary layer in the large basin. The larger basin is influenced by two plumes, the right plume, which is far from the sill; and the plume (that either overflows or intrudes) from the small chamber. The right hand plume does not always rise to the top of the box and the depth of the horizontal outflow from this plume depends upon the heat flux ratio, R_Q and the dimensionless sill gap, φ. The dividing streamline in the bottom boundary layer is the streamline either side of which the water in the cold boundary layer near the centre of the box moves in opposite directions. Its location is effectively an indication of the magnitude of the relative mass flux entering the small basin.

We note that in our experiments the small chamber was always filled by the left plume, however for certain combinations of the parameters R_Q and φ this will not always be the case (Wong & Griffiths, 2001).

Using the results from Chapter 5 and the series of experiments reported here we can study the effect on the circulation of varying the dimensionless sill gap φ with R_Q held constant. Figures 7.3 and 7.4 show for $R_Q = -0.04$ and $R_Q = 0.12$, respectively, a series of circulation visualisations for the three values of φ covered in this thesis. Included in these figures, above each subfigure, is the regime of the circulation in the large basin and which plume is stronger: Left or Right (note that this classification depends on the relative strengths of the two plumes as they enter the large chamber, and not necessarily on the relative strengths of the heat flux applied to each end). Most importantly we see that the regime is unchanged between $\varphi = 1$ and 0.25 (cf. figures 7.3*a*, *b* and 7.4*a*, *b*) but does change once φ decreases to 0.10 (cf. figures 7.3*a*, *c* and 7.4*a*, *c*). Specifically, when $R_Q = -0.04$, regime II L persists for $\varphi = 1$ and 0.25, but the circulation is regime III L for $\varphi = 0.10$. Similarly, when $R_Q \sim 0.12$, regime III R defines the circulation for $\varphi = 1$ and 0.25, but regime II L circulation exists once $\varphi = 0.10$.

As φ is decreased in these experiments the circulation in the tank is most affected for $\varphi = 0.10$, but is relatively unchanged for $\varphi = 0.25$. One further observation is that the location of the dividing streamline in the bottom boundary layer depended on sill depth. For the small range of $|R_Q|$ explored in Chapter 5 ($\varphi = 1$) the dividing streamline was always observed to be in the centre of the tank. When $\varphi = 0.25$ we observe the dividing streamline to again be located near $x/L = 0.5$. However, for $\varphi = 0.10$ the location was near $x/L = 0.3$. This is a significant deviation compared to the experiments with $\varphi = 0.25$ and $\varphi = 1$. The horizontal displacement of the dividing streamline away from the mid-point of the base means that the mass flux into the small basin is reduced, and the mass flux into the right end plume becomes greater than that into the overflow plume, when $\varphi = 0.10$.

7.2.2 Qualitative observations: Effect of R_Q

We now examine the results for constant sill depth but varying the heating difference R_Q. To do this we compare figures 7.3*a* with 7.4*a*, 7.3*b* with 7.4*b*, and the cases shown in figure 7.5. In Chapter 5 ($\varphi = 1$) we found that as R_Q is increased (from negative to positive) the stronger plume changes from being the plume on the left to the plume on the right. When $R_Q = 0$ (figure 5.3) the plumes have equal strength and the confluence point is in the centre of the tank. Thus the circulation and stronger plume is in exact accord with whichever plume is receiving the greater portion of the total heat flux. When $\varphi = 0.25$ (figures 7.3*b* and 7.4*b*) we find the same progression as that for $\varphi = 1$. Specifically, the left hand (overflow) plume dominates

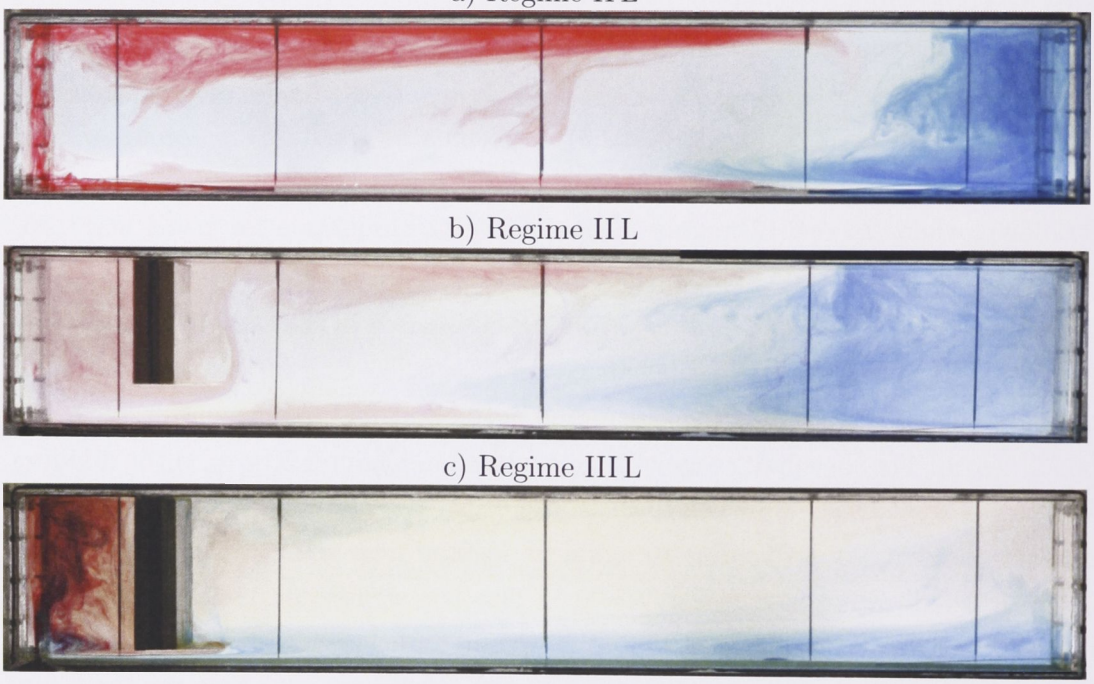

Figure 7.3: Neutrally buoyant food dye visualisation for $R_Q = -0.04$ and a) $\varphi = 1$, b) $\varphi = 0.25$ and c) $\varphi = 0.10$. The dye was added once the flow was in thermal equilibrium. The blue dye was injected into the bottom boundary layer one quarter of the way into the tank from the right end. The red dye was injected into the bottom boundary layer one quarter of the way into the tank from the left end in a) and injected into the tank through the left endwall, 20 mm above the base in b) and c). The initial release of the two colours in one experiment was at approximately the same time. The regime numbers shown are defined in Chapter 5, figure 5.6.

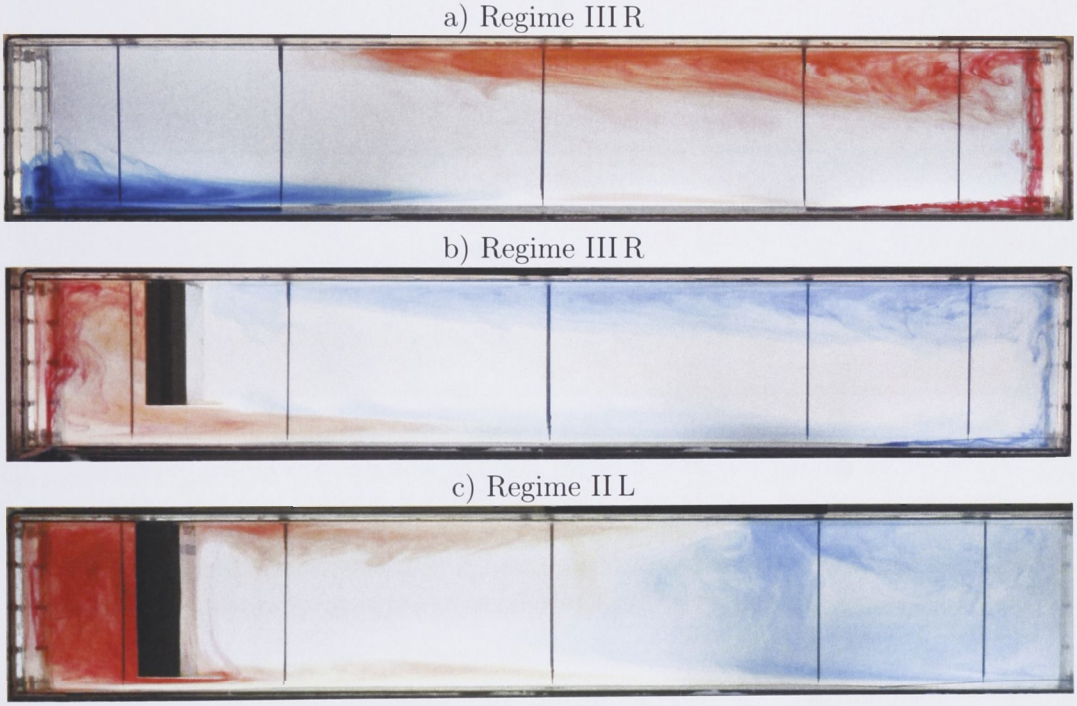

Figure 7.4: Neutrally buoyant food dye visualisation for $R_Q \sim 0.12$ and a) $\varphi = 1$, b) $\varphi = 0.25$ and c) $\varphi = 0.10$. The dye was added once the flow was in thermal equilibrium. The regime numbers shown are defined in Chapter 5, figure 5.6. The image in a) is actually from an experiment with $R_Q \sim -0.12$ and has therefore been flipped about the vertical axis, hence the colour shift.

the circulation when $R_Q < 0$ and the right plume dominates when $R_Q > 0$. For

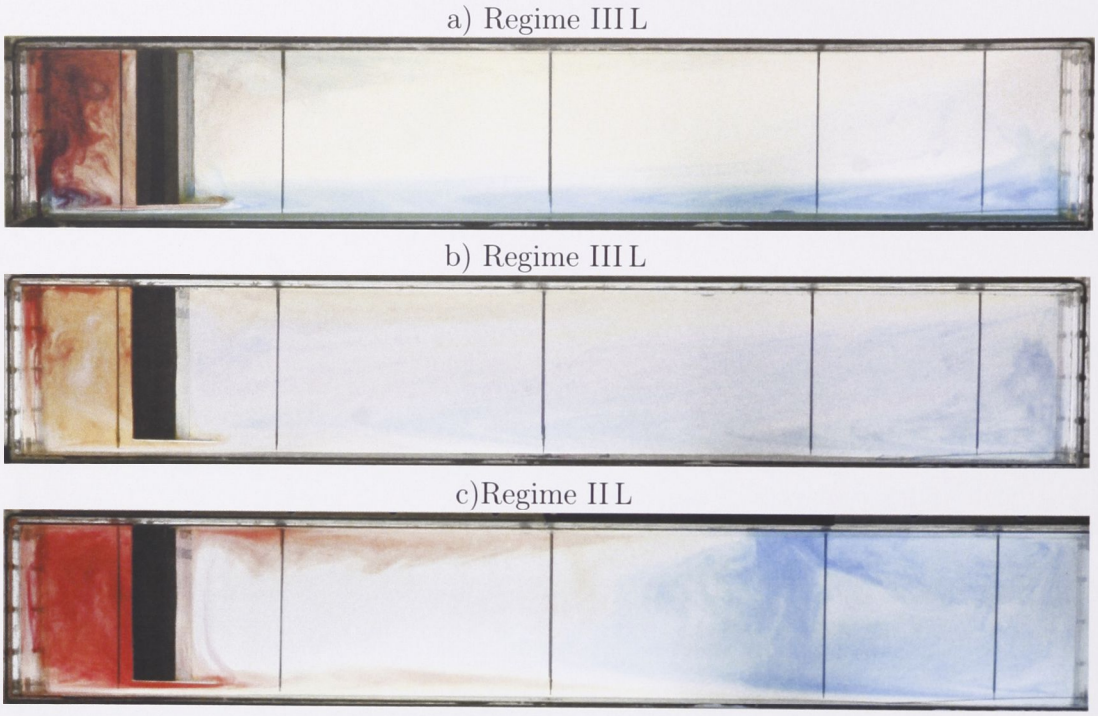

Figure 7.5: Neutrally buoyant food dye visualisation for $\varphi = 0.10$ and a) $R_Q = -0.04$, b) $R_Q = 0.05$ and c) $R_Q = 0.12$. The dye was added once the flow was in thermal equilibrium. The blue dye was injected into the bottom boundary layer one quarter of the way into the tank from the right hand end. The red dye was injected into the tank through the left endwall, 20 mm above the base. The initial release of the two colours was at approximately the same time.

$\varphi = 0.10$, the sequence of photos in figure 7.5 also progresses from negative to positive R_Q but reveals very different flow behaviour. In figure 7.5*a* the left overflow plume rises through the full depth and flows at the top along the entire length of the tank – this is regime 3 circulation in the large basin. In figure 7.5*b* $R_Q > 0$, enabling the right plume to reach almost full depth. In figure 7.5*c* a further increase of R_Q brings the circulation in the larger basin into regime 2. Hence for $R_Q = 0$ and $\varphi = 0.10$ the overflow plume and the right plume will not form a confluence near the centre of the large basin, a significant contrast from the $\varphi = 1$ results. Furthermore, the sequence in figure 7.5 shows a transition from regime III L to regime II L at $0.05 < R_Q < 0.12$, whereas this same transition occurs at $R_Q = -0.1$ for $\varphi = 1$ (see figure 7.8). The reasons behind this large shift of the transition in R_Q parameter space will be explored further in section 7.3. However it is clear that the fundamental effect of this sill is to support a circulation in which the left hand overflow plume is

dominant.

7.2.3 Temperature and stratification measurements

The temperature profiles from this series of experiments are shown in terms of the normalised temperature T^*, where,

$$T^* = \frac{T - T_c}{\overline{T_{1/2} - T_c}}, \tag{7.2}$$

where T_c is the temperature of the cold plate, and $\overline{T_{1/2} - T_c}$ is the average from all the experiments in this series of the temperature difference between the cold plate and $z/D = 0.5$. In calculating $\overline{T_{1/2} - T_c}$ the average over experiments 1 - 5 was used because vertical profile data was not measured for the extra $\varphi = 1$ experiments.

Figure 7.6 shows temperature profiles for $\varphi = 0.25$ (left column) and $\varphi = 0.10$ (right column) each as a function of location along the tank ($x/L = 0.1$, 0.5, 0.9) and R_Q. Comparison between the first and second columns of figure 7.6 shows that for the more restrictive $\varphi = 0.10$ sill the bulk temperature throughout the tank is warmer. A comparison of figures 7.6*a* and *d* supports the visual evidence of reduced mass flux into the small basin for $\varphi = 0.10$. The profiles show a much thinner boundary layer at the left hand end for the $\varphi = 0.10$ case compared with the $\varphi = 0.25$ case. Within each set of experiments with a given φ a smaller value of R_Q results in a warmer small basin temperature. This is directly attributed to the relatively larger flux applied through the left heating mat for smaller R_Q.

The profile for run 3 in figure 7.6*f* (green line) shows the signature of the intruding right plume between $0.05 < z/D < 0.2$. The intrusion was due to the very buoyant sill overflow which led to this (regime 3) circulation in the large basin.

We define a Nusselt number based on the heat transfer through the gap,

$$Nu_1 = \frac{F_1 L}{\rho_0 C_P \kappa \delta T}, \tag{7.3}$$

where F_1 is the input heat flux to the left heating mat ($H_1/(0.15 \times 0.30)\,\mathrm{W/m^2}$) and δT is the temperature difference between the centre of the cold plate and the centre of the left hand hot plate, as measured by the embedded thermistors.

Figure 7.7 plots the Nusselt number Nu_1, against the heat flux ratio R_Q, for the different values of φ. Most importantly, for the same R_Q the cases with $\varphi = 1$ and 0.25 have very close Nu_1 values, whereas Nu_1 is much reduced for $\varphi = 0.10$. This implies that the more restricted flow ($\varphi = 0.10$) has a larger horizontal temperature

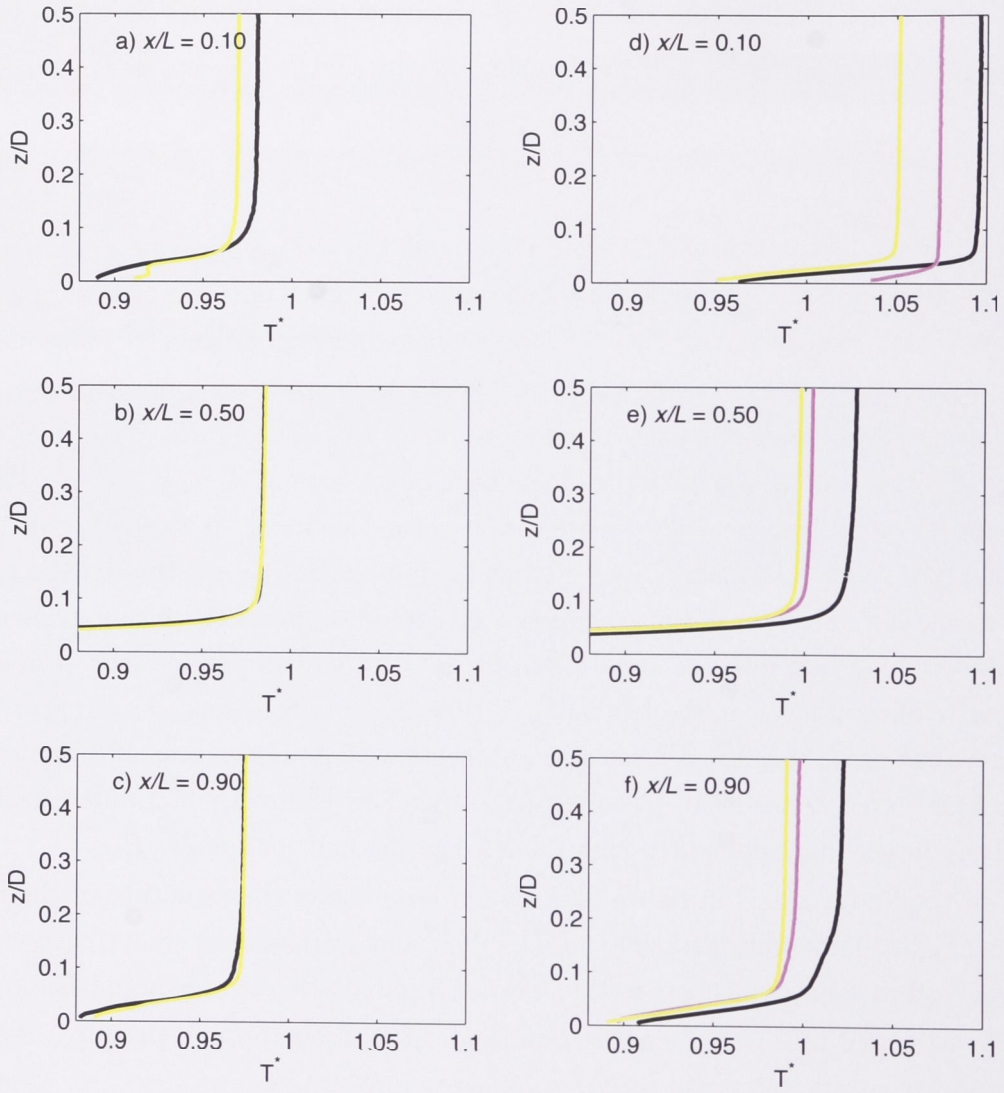

Figure 7.6: Comparison of normalised temperature profiles for the sill experiments with a), b) and c) $\varphi = 0.25$, and d), e) and f) $\varphi = 0.10$ at three different locations along the tank; a) and d) $x/L = 0.10$, b) and e) $x/L = 0.50$ and c) and f) $x/L = 0.90$. Black line, $R_Q = -0.04$, pink line, $R_Q = 0.05$, and yellow line, $R_Q = 0.12$.

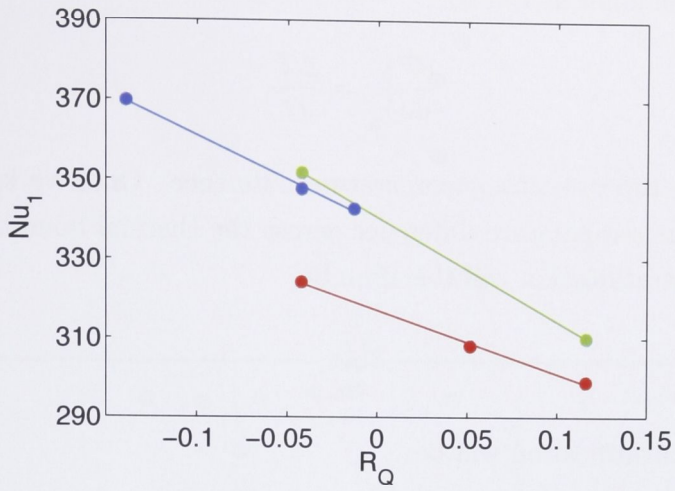

Figure 7.7: Nusselt number versus heat flux ratio for $\varphi = 1$ (blue), $\varphi = 0.25$ (green) $\varphi = 0.10$ (red), the linear fit to the data is also included.

difference δT for a given R_Q, which also implies a larger temperature difference between the small and large basins. More generally, the Nusselt number decreases with increasing R_Q for all φ. This is because the reduction in F_1 is much larger than the increase in δT as R_Q increases, thus overall Nu_1 decreases. A linear trend was computed from the Nu_1 data and we see slightly different slopes for each φ. The difference is due to the manner in which δT varies with R_Q for each φ. The slopes for $\varphi = 1$ and 0.25 are comparatively more similar than the slope for $\varphi = 0.10$.

Using the result from Mullarney *et al.* (2004) for a single plume forced by 271 W we find an upper bound on the value of the Nusselt number at $R_Q = -1$. We use their scaling result, $Nu \sim 0.81587 Ra_F^{1/6}$, adjust for the difference in total heat input and the different destabilising forcing lengths, and find the Nusselt number to be 463. This is an upper bound because Mullarney *et al.* (2004) based their δT on the maximum temperature difference measured in the interior of the box, whereas we have used the temperature difference between the left hot plate and the cold plate.

For each of the experiments presented in this chapter, the temperature profile from the mid-point ($x/L = 0.5$) of the tank is used to determine the stratification in the larger basin. In contrast to the profiles from chapter 5, the present temperature profiles outside the boundary layer were not well approximated by a linear fit. Instead we find the boundary layer thickness and calculate the temperature difference between $z = D$ and $z = z_b$, where z_b is the height of the thermal boundary layer

and defined as the point at which,

$$\left.\frac{dT}{dz}\right|_{z_b} = \frac{\Delta T}{D}, \tag{7.4}$$

where ΔT is the top-to-bottom temperature difference. Once we know z_b we can also find ΔT_b, the temperature difference across the thermal boundary layer. The boundary layer stratification will therefore be,

$$\frac{\Delta T_b}{z_b}, \tag{7.5}$$

and the interior stratification will be,

$$\frac{\Delta T - \Delta T_b}{D - z_b}. \tag{7.6}$$

We normalise the interior stratification by $D/\Delta T_{ref}$, where $\Delta T_{ref} = \overline{T_{1/2} - T_c}|_{sill}$ is the average over all the sill experiments of the temperature difference between $z/D = 0.5$ and the cold plate. In figure 7.8 we plot the interior stratification for the sill experiments, as well as the measurements for the $\varphi = 1$ case (re-calculated using the method outlined above, including normalisation with the same ΔT_{ref}).

The stratification results for the experiments with $\varphi = 0.25$ are consistent with the $\varphi = 1$ results and the notion that a 75% barrier does not significantly modify the bulk characteristics of the convective circulation. However, the stratification results for $\varphi = 0.10$ show a marked departure from the regime boundaries defined for $\varphi = 1$. This is consistent with the qualitative observations and the normalised temperature profiles, which showed significant differences in the circulation pattern, Nusselt number and temperature trends compared with $\varphi = 1$ and $\varphi = 0.25$.

7.3 Discussion

When $\varphi = 1$ (no sill) the thermal boundary layer thickness is close to $0.1D$. Therefore when $\varphi = 0.10$ the sill extends into the region where the thermal boundary layer plus the return flow would otherwise be. However, the gap must accommodate a mass exchange in the thermal boundary layer and the return flow over the sill. Therefore, for $\varphi = 0.10$ the exchange flow through the gap is modified in comparison to the $\varphi = 1$ case. The velocities in the exchange region are difficult to determine accurately. However, we observe the dividing streamline between leftward and rightward flow in the bottom boundary layer to be located near $x/L = 0.3$ for

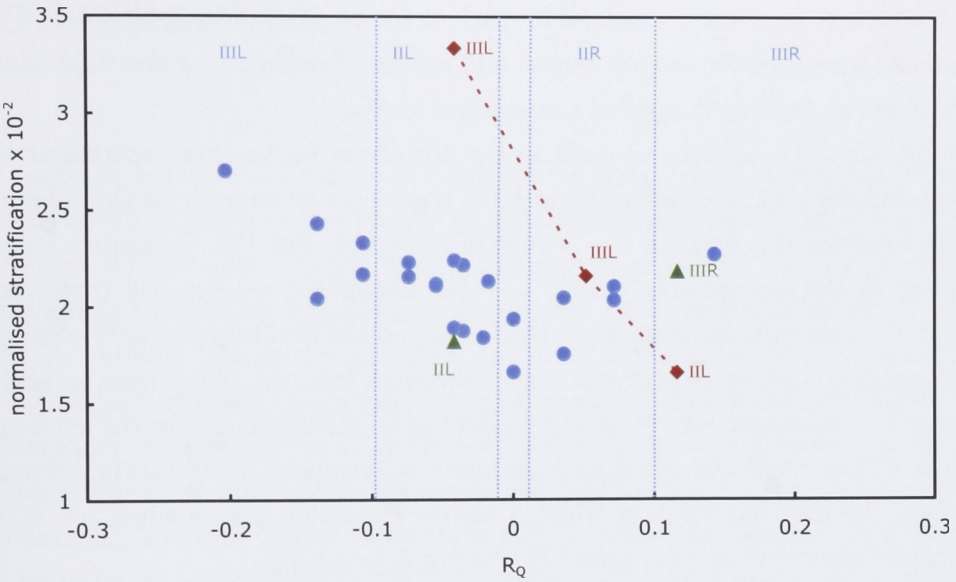

Figure 7.8: Comparison of the normalised interior stratification for the experiments with and without a sill. •: $\varphi = 1$, ▲: $\varphi = 0.25$, ♦: $\varphi = 0.10$. Sill data points are labeled with the flow regime, I, II or III, and L or R, representing whether the left or right plume is dominant, as observed during visualisation. The regime boundaries for the $\varphi = 1$ data are shown by the blue dashed lines, and are also labeled according to the description above. The interior stratification measurements were less sensitive than the Nu_1 measurements to the replacement of the left heating mat and so we present all the data from Chapter 5 for comparison with the sill experiments in this figure.

$\varphi = 0.10$. This is a significant deviation compared to the experiments with $\varphi = 0.25$ and $\varphi = 1$, for which the dividing streamline was close to $x/L = 0.5$. Thus, for $\varphi = 0.10$, the mass flux into the small basin is reduced, and the mass flux into the right end plume is increased in comparison with either the $\varphi = 0.25$ or $\varphi = 1$ case. This is consistent with the normalised temperature plots, which show a thinning of the thermal boundary layer at $x/L = 0.1$ when φ is decreased from 0.25 to 0.10. In addition to achieving an asymmetry in the mass flux through each plume the leftward displacement of the dividing streamline also alters the length of the cold plate available to cool water destined for each of the plumes. The result for $\varphi = 0.10$ is enhanced buoyancy for the left plume and reduced buoyancy for the right plume, even if the heat flux input applied to each end is equal.

In summary the addition of a sill to the horizontal convection experiment with two destabilising regions creates a circulation that depends strongly on the sill depth. The sill impedes the flow for the values of φ tested, but the disruption is most significant in the experiments with $\varphi = 0.10$. Compared with no sill cases, when $\varphi = 0.25$ the thermal boundary layer thickness and the dividing streamline location are unchanged, and we expect the mass transport into the left plume to also be unchanged. In contrast, for $\varphi = 0.10$ the thermal boundary layer over the left heated region is thinner and the dividing streamline is displaced significantly leftwards. Therefore, the heat flux ratio at which a regime transition occurs when $\varphi = 0.10$ is significantly altered from that found in chapter 5 for no sill.

The results presented in this chapter are consistent with the experiments conducted in Chapter 3, in which a box with differentially heated endwalls is partially divided by a barrier into two connected basins. The magnitude of the mass transport in one direction through the gap was found to be fairly constant for barrier heights $< 80\%$ of the tank depth and the transport was then significantly reduced for barriers $> 80\%$ of the tank depth.

The results from this chapter suggest that topographical features, such as the Denmark Straits and Faroe Bank Channel, are regions that may control the global circulation structure. This is because these regions are some of the few topographic features in the present ocean with a φ between 0.2 and 0.1.

Chapter 8

Conclusions

The introduction of a barrier to the bottom of a box with differentially heated endwalls severely disrupts the transport of heat and mass in the boundary layers adjacent to the box endwalls and base. Temperature profiles in the box are dramatically modified, with the formation of a very cold basin and a moderately warmer basin. A complex flow structure arises, featuring a fast overflow of the barrier, a varying number of shear layers in the density stratified flow above the barrier, partial boundary layer detrainment on the cold endwall, and slow upwelling in the cold chamber. The heat (and mass) transport is little changed for small and medium-sized barriers, and only begins to decrease rapidly when the barrier height becomes very large (in excess of 80% of the box height). The heat transport is also only weakly dependent on the lateral position of the barrier and the volume transport increases slightly as the barrier is moved closer to the cooled endwall.

In the remainder of this thesis the convective circulation due to thermal forcing at one horizontal level or boundary was explored. Sandström's original experiments (Sandström, 1908) were reproduced and extended in order to clarify the contradiction between his conclusion and Rossby's (1965) experiments. We observed a persistent circulation under steady state conditions for the three arrangements of the sources of heating and cooling; heating below cooling, heating and cooling at the same level and heating above cooling. Therefore, despite a close reconstruction of Sandström's apparatus and methods we were unable to obtain results consistent with his report of no sustained circulation for heating and cooling sources at the same level or for the heat source above the cooling source. We can only conjecture as to the differences between our observations and the report by Sandström, however the reduction in the steady state velocities compared with the initial transient flow velocities may have played a role. Regardless, Sandström did not consider the role diffusion would play in transporting heat away from the source, which leaves the

magnitude of the circulation insensitive to small changes in the relative height of the heating and cooling sources. This point was realised early on by Jeffreys (1925), however Sandström's 'theorem' gained a foothold in the oceanographic community (Defant, 1961), and has continued to cloud the discussion as to whether buoyancy forcing of the ocean surface has a role in the meridional overturning circulation. We concluded that Sandström's report was incorrect and there is no basis for Sandström's 'theorem.'

High Rayleigh number, non-rotating horizontal convection experiments in a long box with two destabilising regions of forcing shows that a steady state circulation exists which depends on the ratio (R_Q) of the heat input to each destabilising region. The heating near the ends of the box and cooling in the centre of the box established a temperature and pressure gradient along the base. Cold water from the centre of the box is drawn towards the heated ends of the base where it gains buoyancy and rises up the endwalls as unsteady, entraining plumes. The stable thermal boundary layer established above the cold plate is eroded by convective instabilities as the water flows over the heated regions, forming a convective mixed layer (CML). Three regimes of circulation are defined which depend on R_Q. Regime 1 occurs when the heat input to each plume is equal, which results in strong symmetry of the flow about the centre of the box. For instance, the confluence of the horizontal outflow from each of the full depth plumes is at the top of the box and very close to the centre. Regime 2 occurs for slightly unequal heat inputs. Both plumes penetrate through the full box depth but the horizontal outflow from each plume is of different strength and the confluence of the outflows is moderately or highly off centre. Regime 3 occurs when the mismatch of heat input to the two plumes is greater than about 10%. In these cases one plume does not have enough buoyancy to penetrate to the top of the box and therefore intrudes into the interior of the box underneath the horizontal outflow from the stronger plume. For large R_Q the weaker plume intrudes into the interior just above the thermal boundary layer. For all regimes the flow below the main horizontal outflow consists of a broad and comparatively slow downwelling into an entraining endwall plume or the bottom thermal boundary layer. Vertical temperature profiles reveal strong thermal gradients in the boundary layer and much weaker gradients in the interior. Although small, the interior gradient is dynamically significant in a steady state because it requires at least one of the plumes to extend through the full box depth. Measurements of the stratification in the interior revealed that a doubling of the interior stratification occurs when $|R_Q|$ increases from 0 to 0.2. Use of previous data from Mullarney *et al.* (2004) helped to illustrate that the interior stratification for one plume in a box will be similar to

the interior stratification for two plumes in the same box, if each plume is supplied with the same buoyancy flux.

These experiments have shown that the structure of the large scale meridional overturning circulation with two sinking regions will depend on the strength of the buoyancy forcing towards each sinking region. Many factors act to enhance or alter the buoyancy of the deep sinking water (whether it be at the surface or through entrainment and mixing in turbulent slope currents). Regardless of the manner of buoyancy exchange, these experiments have shown that a significant change in circulation can occur when the buoyancy of the plumes is changed only slightly. Supposing the meridional overturning circulation is presently in regime 1 or 2 a 10% change is likely to significantly alter the present circulation.

The numerical solutions for the case of two sinking regions confirmed the experimental results. In addition we examined internal wave activity in the box and concluded that the variability of the confluence point, the horizontal and vertical velocities and of the stream function in the numerical and laboratory experiments, was largely due to the presence of internal waves. The outflow from a full depth plume contains eddies which disturb the background stratification and excite internal waves. The internal waves were fully characterised for the case of two equal plumes (regime 1) and a simple theory was developed to explain the existence and origins of the internal waves. This theory was successfully used to predict the dominant wave modes in the experiment.

Internal waves in the ocean are more generally discussed in the literature because of the contribution breaking internal waves can make to the turbulent mixing of the ocean. However, internal waves generated by abyssal gravity or slope currents have not been considered. In the experiments these motions were a large part of the flow, however it remains to be seen whether similarly generated internal waves will have a significant effect on the large-scale abyssal ocean flow.

The addition of a sill to the horizontal convection experiment with two destabilising regions created two basins; a small basin that was filled by the plume from the left hand end; and a larger basin which was controlled by the overflow from the small basin and the plume from the right hand end. The gap adjacent to the sill, through which the transport of heat and mass occurs, was equal to 10% and 25% of the box depth, i.e. $\varphi = 0.10$ or 0.25, respectively. These values were chosen to create comparable gap sizes to marginal sea sills such as the Denmark Straits and Faroe Bank Channel. The circulation depended strongly on the sill depth and input heat flux ratio, R_Q. The sill impeded the flow in both cases, but the disruption was most significant in the experiments with the $\varphi = 0.10$ sill. We defined the regime of the

circulation in the larger chamber using the same criteria as for the experiments with no sill. We found that the heat flux ratio at which a regime transition occurs when $\varphi = 0.10$ is significantly altered from that found in chapter 5 for no sill, however, no change was found for $\varphi = 0.25$. The location of the dividing streamline in the bottom boundary layer (that is, the streamline either side of which the water in the cold boundary layer near the centre of the box moves to the left or right) is indicative of the proportion of the mass flux entering the small basin. The displacement of the regime transitions for $\varphi = 0.10$ and not for $\varphi = 0.25$, compared to the case with no sill, is explained in terms of the mass flux past the sill. As the gap height approaches the thermal boundary layer thickness of the no sill case the exchange flow through the gap is modified because the gap must accommodate a mass exchange in the thermal boundary layer and the return flow over the sill. When $\varphi = 0.25$ the gap height is somewhat larger than the $\varphi = 1$ boundary layer thickness. However, when $\varphi = 0.10$ the sill extends into the region where the thermal boundary layer would otherwise be and therefore a significant deviation from $\varphi = 1$ flow occurs. This is supported by the measurements of the thermal boundary layer thickness and the dividing streamline location which are unchanged for $\varphi = 0.25$, and we expect the mass transport into the left plume to also be unchanged. In contrast, for $\varphi = 0.10$ the thermal boundary layer over the left heated region is thinner and the dividing streamline is displaced significantly leftwards, thus reducing the heat transport into the left plume and significantly altering the buoyancy of the sill overflow, which in turn influences the circulation in the large basin.

As other studies have concluded (Bryden & Nurser, 2003; Finnigan & Ivey, 2000; Whitehead, 1998) large topography has a non-negligible role to play in contributing to the dynamics of the meridional overturning circulation. Consideration must be given as to how much the presence of a sill will modify the slope current overflows, through mixing and entrainment, and to the restricted heat and mass fluxes across the sill. Such 'choke points' on the circulation lead to increased density differences and therefore to greater density of water destined to form the deep and bottom water of the oceans. The depth of the sill will influence any change in overturning circulation pattern following a change in surface buoyancy forcing.

Bibliography

Baines, W. D. & Turner, J. S. 1969 Turbulent buoyant convection from a source in a confined region. *Journal of Fluid Mechanics* **37**, 51–80.

Beardsley, R. C. & Festa, J. F. 1972 A numerical model of convection driven by a surface stress and non-uniform heating. *Journal of Physical Oceanography* **2**, 444–455.

Bejan, A. 1979 Note on Gill solution for free convection in a vertical enclosure. *Journal of Fluid Mechanics* **90**, 561–568.

Bejan, A. 1980 A synthesis of analytical results for natural convection heat transfer across rectangular enclosures. *International Journal of Heat and Mass Transfer* **23**, 723–726.

Bejan, A., Al-Homoud, A. A. & Imberger, J. 1981 Experimental study of high-rayleigh number convection in a horizontal cavity with different end temperatures. *Journal of Fluid Mechanics* **109**, 283–299.

Bejan, A. & Tien, C. L. 1978 Laminar natural convection heat transfer in a horizontal cavity with different end temperatures. *International Journal of Heat and Mass Transfer* **100**, 641–647.

Bjerknes, V. 1916 Über thermodynamische Maschinen die unter Mitwirkung der Schwerkraft arbeiten. *Abhandlungen der Mathematisch-Physischen Klasse der Königlich Sächsischen Gesellschaften*, vol. 35, p. 29. Leipzig.

Blythe, P. A. & Simpkins, P. G. 1977 *Physico-chemical Hydrodynamics* **2**, 511.

Bryden, HL & Nurser, AJG 2003 Effects of strait mixing on ocean stratification. *Journal of Physical Oceanography* **33** (8), 1870–1872.

Chiu-Webster, S., Hinch, E. J. & Lister, J. R. 2008 Very viscous horizontal convection. *Journal of Fluid Mechanics* **611**, 395–426.

Coman, M. A., Griffiths, R. W. & Hughes, G. O. 2006*a* Sandstrom's experiments revisited. *Journal of Marine Research* **64** (6), 783–796.

Coman, M. A., Hughes, G. O., Kerr, R. C. & Griffiths, R. W. 2006*b* The effect of a barrier on laminar convection in a box with differentially heated endwalls. *International Journal of Heat and Mass Transfer* **49** (17-18), 2903–2911.

Cormack, D.E., Leal, L. G & Imberger, J. 1974*a* Natural convection in a shallow cavity with differentially heated end walls. Part 1. Asymptotic theory. *Journal of Fluid Mechanics* **65**, 209–229.

Cormack, D.E., Leal, L. G & Seinfeld, J. H. 1974*b* Natural convection in a shallow cavity with differentially heated end walls. Part 2. Numerical solutions. *Journal of Fluid Mechanics* **65**, 231–246.

Cunningham, Stuart A., Kanzow, Torsten, Rayner, Darren, Baringer, Molly O., Johns, William E., Marotzke, Jochem, Longworth, Hannah R., Grant, Elizabeth M., Hirschi, Joel J. M., Beal, Lisa M., Meinen, Christopher S. & Bryden, Harry L. 2007 Temporal variability of the atlantic meridional overturning circulation at 26.5 degrees n. *Science* **317** (5840), 935–938.

Defant, A. 1961 *Physical Oceanography: Volume I*. New York, USA: MacMillan.

Dickson, RR & Brown, J 1994 The production of north-atlantic deep-water - sources, rates, and pathways. *Journal of Geophysical Research-Oceans* **99**, 12319–12341.

Eckert, E. R. G. & Carlson, W. O. 1961 Natural convection in an air layer enclosed between two vertical plates with different end temperatures. *International Journal of Heat and Mass Transfer* **2**, 106.

Finnigan, T. D. & Ivey, G. N. 2000 Convectively driven exchange flow in a stratified sill-enclosed basin. *Journal of Fluid Mechanics* **418** (-1), 313–338.

Fischer, HB 1972 Mass-transport mechanisms in partially stratified estuaries. *Journal of Fluid Mechanics* **53**, 671–687.

Ganachaud, A. & Wunsch, C. 2000 Improved estimates of global ocean circulation, heat transport and mixing from hydrographic data. *Nature* **408**, 453–457.

Gill, A. E. 1966 The boundary layer regime for convection in a rectangular cavity. *Journal of Fluid Mechanics* **26**, 515–536.

GNANADESIKAN, A 1999 A simple predictive model for the structure of the oceanic pycnocline. *Science* **283**, 2077–2079.

GNANADESIKAN, A, DE BOER, A. M. & MIGNONE, B. M. 2007 *A simple theory of the pycnocline and overturning revisited*, *Geophysical monograph series*, vol. 173. Washington, DC: American Geophysical Union.

GREGG, M. C. 1989 Scaling turbulent dissipation in the thermocline. *Journal of Geophysical Research* **94**, 9686–9698.

HOUGHTON, J. T., MEIRA FILHO, L. G., CALLANDER, B. A., HARRIS, N., KATTENBERG, A. & MASKELL, K. 1996 *Climate change 1995: The science of climate change*. Cambridge, England: Cambridge University Press.

HUANG, R. X. 1999 Mixing and energetics of the oceanic thermohaline circulation. *Journal of Physical Oceanography* **29**, 727–746.

HUGHES, G. O. & GRIFFITHS, R. W. 2006 A simple convective model of the global overturning circulation, including effects of entrainment into sinking regions. *Ocean Modelling* **12**, 46–79.

HUGHES, GRAHAM O. & GRIFFITHS, ROSS W. 2008 Horizontal convection. *Annual Review of Fluid Mechanics* **40** (1), 185–208.

HUGHES, G. O., GRIFFITHS, R. W., MULLARNEY, J. C. & PETERSON, W. H. 2007 A theoretical model for horizontal convection at high Rayleigh number. *Journal of Fluid Mechanics* **581**, 251–276.

IMBERGER, J. 1974 Natural convection in a shallow cavity with differentially heated end walls. part 3. experimental results. *Journal of Fluid Mechanics* **65**, 247–260.

JEFFREYS, H. T. 1925 On fluid motions produced by differences of temperature and humidity. *Quarterly Journal of the Royal Meteorological Society* **51**, 347–356.

JONES, H & MARSHALL, J 1993 Convection with rotation in a neutral ocean - a study of open-ocean deep convection. *Journal of Physical Oceanography* **23**, 1009–1039.

KILLWORTH, PETER D. 1976 The mixing and spreading phases of MEDOC. I. *Progress In Oceanography* **7** (2), 59–90.

KILLWORTH, P. D. & MANINS, P. C. 1980 A model of confined thermal convection driven by non-uniform heating from below. *Journal of Fluid Mechanics* **98**, 587–607.

KILLWORTH, P. D. & TURNER, J. S. 1982 Plumes with time-varying buoyancy in a confined region. *Geophysical and Astrophysical Fluid Dynamics* **20**, 265–291.

KUHLBRODT, T., GRIESEL, A., MONTOYA, M., LEVERMANN, A., HOFMANN, M. & RAHMSTORF, S. 2007 On the driving processes of the atlantic meridional overturning circulation. *Reviews of Geophysics* **45** (1), RG2001.

LE QUERE, P & BEHNIA, M 1998 From onset of unsteadiness to chaos in a differentially heated square cavity. *Journal of Fluid Mechanics* **359**, 81–107.

LEDWELL, J. R., WATSON, A. J. & LAW, C. S. 1993 Evidence for slow mixing across the pycnocline from an open-ocean tracer release experiment. *Nature* **364**, 701–703.

LEGG, S. & MARSHALL, J 1993 A heton model of the spreading phase of open-ocean deep convection. *Journal of Physical Oceanography* **23** (6), 1040–1056.

LINDEN, P. F. 1999 The fluid mechanics of natural ventilation. *Annual Reviews in Fluid Mechanics* **31**, 201–238.

MACDONALD, A. M. & WUNSCH, C. 1996 An estimate of global ocean circulation and heat fluxes. *Nature* **382**, 436–439.

MANINS, P. C. 1973 A filling box model of the deep circulation of the Red Sea. *Mémoires Société Royale des Sciences de Liége* **6**, 153–166.

MARCHAL, OLIVIER 2007 Particle transport in horizontal convection: Implications for the "Sandstrom theorem". *Tellus Series A-Dynamic Meteorology and Oceanography* **59** (1), 141–154.

MILLER, R. C. 1968 A thermally convecting fluid heated non-uniformly from below. PhD thesis, MIT.

MULLARNEY, J. C., GRIFFITHS, R. W. & HUGHES, G. O. 2004 Convection driven by differential heating at a horizontal boundary. *Journal of Fluid Mechanics* **516**, 181–209.

MULLARNEY, J. C., GRIFFITHS, R. W. & HUGHES, G. O. 2006 The effects of geothermal heating on the ocean overturning circulation. *Geophysical Research Letters* **33** (L02607).

MUNK, W. H. 1966 Abyssal recipes. *Deep-Sea Research* **13**, 707–730.

MUNK, W. H. & WUNSCH, C. 1998 Abyssal recipes II: energetics of tidal and wind mixing. *Deep-Sea Research I* **45**, 1977–2010.

NYCANDER, J., NILSSON, J., DOOS, K. & BROSTROM, G. 2007 Thermodynamic analysis of ocean circulation. *Journal of Physical Oceanography* **37**, 2038–2052.

ORSI, A. H., SMETHIE JR., W. M. & BULLISTER, J. L. 2002 On the total input of Antarctic waters to the deep ocean: a preliminary estimate from chlorofluorocarbon measurements. *Journal of Geophysical Research* **107** (C83122).

PAPARELLA, F. & YOUNG, W. R. 2002 Horizontal convection is non-turbulent. *Journal of Fluid Mechanics* **466**, 205–214.

PATTERSON, J. & IMBERGER, J. 1980 Unsteady natural convection in a rectangular cavity. *Journal of Fluid Mechanics* **100**, 65–86.

PIERCE, DW & RHINES, PB 1997 Convective building of a pycnocline: A two-dimensional nonhydrostatic numerical model. *Journal of Physical Oceanography* **27** (6), 909–925.

PIERCE, D. W. & RHINES, P. B. 1996 Convective building of a pycnocline: laboratory experiments. *Journal of Physical Oceanography* **26**, 176–190.

POLZIN, K. L., TOOLE, J. M., LEDWELL, J. R. & SCHMITT, R. W. 1997 Spatial variability of turbulent mixing in the abyssal ocean. *Science* **276**, 93–96.

PRICE, J. F. & BARINGER, M. O. 1994 Outflows and deep water production by marginal seas. *Progress in Oceanography* **33**, 161–200.

QUON, C 1972 High Rayleigh number convection in an enclosure - numercial study. *Physics of Fluids* **15** (1), 12.

RAHMSTORF, STEFAN 2002 Ocean circulation and climate during the past 120,000 years. *Nature* **419** (6903), 207–214.

ROSSBY, H. T. 1965 On thermal convection driven by non-uniform heating from below: an experimental study. *Deep-Sea Research* **12**, 9–16.

ROSSBY, H. T. 1998 Numerical experiments with a fluid non-uniformly heated from below. *Tellus* **50**, 242–257.

RUDNICK, D. L., BOYD, T. J., BRAINARD, R. E., CARTER, G. S., EGBERT, G. D., GREGG, M. C., HOLLOWAY, P. E., KLYMAK, J. M., KUNZE, E., LEE, C. M., LEVINE, M. D., LUTHER, D. S., MARTIN, J. P., MERRIFIELD, M. A., MOUM, J. N., NASH, J. D., PINKEL, R., RAINVILLE, L. & SANFORD, T. B. 2003 From tides to mixing along the Hawaiian ridge. *Science* **301**, 355–357.

SAMELSON, RM 2004 Simple mechanistic models of middepth meridional overturning. *Journal of Physical Oceanography* **34** (9), 2096–2103.

SANDSTRÖM, J. W. 1908 Dynamische Versuche mit Meerwasser. *Annalen der Hydrographie und Maritimen Meteorologie* **36**, 6–23.

SANDSTRÖM, J. W. 1916 Meteorologische Studien im Schwedischen Hochgebirge. *Göteborgs Kungl. Vetenskaps- och Vitterhetssamhälles Handlingar* **17**, 1–48.

SANDSTRÖM, J. W. 1922 Deux théoremes fondamentaux de la dynamique de la mer. *Svenska Hydrografisk-Biologiska Kommissionens Skrifter* **7**.

SCHMITT, RW 1995 The salt-finger experiments of Jevons (1857) and Rayleigh (1880). *Journal of Physical Oceanography* **25**, 8–17.

SEND, U. & MARSHALL, J. 1995 Integral effects of deep convection. *Journal of Physical Oceanography* **25**, 855–872.

SIGGERS, JH, KERSWELL, RR & BALMFORTH, NJ 2004 Bounds on horizontal convection. *Journal of Fluid Mechanics* **517**, 55–70.

SIMPKINS, P. G. & CHEN, K. S. 1986 Convection in horizontal cavities. *Journal of Fluid Mechanics* **166**, 21–39.

SIMPKINS, P. G. & DUDDERAR, T. D. 1981 Convection in rectangular cavities with differentially heated end walls. *Journal of Fluid Mechanics* **110**, 433–456.

SMITH, WALTER H.F. & SANDWELL, DAVID T. 1997 Global sea floor topography from satellite altimetry and ship depth soundings. *Science* **277** (5334), 1956–1962.

SPALL, MA & PICKART, RS 2001 Where does dense water sink? a subpolar gyre example. *Journal of Physical Oceanography* **31** (3), 810–826.

ST LAURENT, L. & SIMMONS, H. 2006 Estimates of power consumed by mixing in the ocean interior. *Journal of climate* **19** (19), 4877–4890.

STEWART, M.J. & WEINBERG, F 1972 Fluid-flow in liquid-metals .1. Theoretical analysis. *Journal of Crystal Growth* **12** (3), 217–227.

STOMMEL, H 1958 The abyssal circulation. Deep-Sea Research.

STOMMEL, H. 1962 On the smallness of sinking regions in the ocean. *Proceedings of the National Academy of Sciences, Washington* **48**, 766–772.

STOMMEL, H, ARONS, AB & BLANCHARD, D 1956 An oceanographical curiosity - the perpetual salt fountain. *Deep-Sea Research* **3** (2), 152–153.

TALLEY, L. D. 1999 *Some aspects of ocean heat transport by the shallow, intermediate and deep overturning circulations. Geophysical monograph series* 112. Washington, D.C.: American Geophysical Union.

TOGGWEILER, J. R. & SAMUELS, B 1995 Effect of Drake Passage on the global thermohaline circulation. *Deep-Sea Research Part I-Oceanographic Research Papers* **42** (4), 477–500.

TOGGWEILER, J. R. & SAMUELS, B. 1998 On the ocean's large-scale circulation near the limit of no vertical mixing. *Journal of Physical Oceanography* **28**, 1832–1852.

TRIAS, F. X., SORIA, M., OLIVA, A. & PEREZ-SEGARRA, C. D. 2007 Direct numerical simulations of two- and three-dimensional turbulent natural convection flows in a differentially heated cavity of aspect ratio 4. *Journal of Fluid Mechanics* **586**, 259–293.

TRITTON, D. J. 1988 *Physical Fluid Dynamics*, 2nd edn. Oxford University Press.

TURNER, JS & VERONIS, G 2000 Laboratory studies of double-diffusive sources in closed regions. *Journal of Fluid Mechanics* **405**, 269–304.

TURNER, J. S. 1973 *Buoyancy effects in fluids*. Cambridge, England: Cambridge University Press.

TURNER, J. S. 1979 *Buoyancy Effects in Fluids*. Cambridge, England: Cambridge University Press.

WANG, W. & HUANG, R. X. 2005 An experimental study on thermal convection driven by horizontal differential heating. *Journal of Fluid Mechanics* **540**, 49–73.

WEBB, D.J. & SUGINOHARA, N. 2001 Oceanography — Vertical mixing in the ocean. *Nature* **409**, 37–37.

WHITEHEAD, JA 1998 Topographic control of oceanic flows in deep passages and straits. *Reviews of Geophysics* **36** (3), 423–440.

WHITEHEAD, J. A. & WANG, WEI 2008 A laboratory model of vertical ocean circulation driven by mixing. *Journal of Physical Oceanography* **38**, 1091–1106.

WONG, A. B. D. & GRIFFITHS, R.W. 1999 Stratification and convection produced by multiple plumes. *Dynamics of Atmospheres and Oceans* **30**, 101–123.

WONG, A. B. D. & GRIFFITHS, R. W. 2001 Two-basin filling boxes. *Journal of Geophysical Research* **106**, 26929–26941.

WOODS, AW & BUSH, JWM 1999 Dimensions and dynamics of megaplumes. *Journal of Geophysical Research-Oceans* **104** (C9), 20495–20507.

WORSTER, M. G. & LEITCH, A. M. 1985 Laminar free convection in confined regions. *Journal of Fluid Mechanics* **156**, 301–319.

WUNSCH, C. 2000 Moon, tides & climate. *Nature* **405**, 743–744.

WUNSCH, C 2002 What is the thermohaline circulation? *Science* **298** (5596), 1179–1181.

WUNSCH, C. & FERRARI, R. 2004 Vertical mixing, energy, and the general circulation of the oceans. *Annual Reviews in Fluid Mechanics* **36**, 281–314.

XIN, SH & LE QUERE, P 1995 Direct numerical simulations of two-dimensional chaotic natural convection in a differentially heated cavity of aspect ratio 4. *Journal of Fluid Mechanics* **304**, 87–118.